Magnetic Trapping of Imidogen Molecules

A dissertation presented
by

Wesley C. Campbell

to
The Department of Physics
in partial fulfillment of the requirements
for the degree of
Doctor of Philosophy
in the subject of

Physics

Harvard University
Cambridge, Massachusetts
February 2008

Thesis advisor

John M. Doyle

Author

Wesley C. Campbell

Magnetic Trapping of Imidogen Molecules

Abstract

This thesis consists of the description of a series of experiments with cold imidogen (nitrogen monohydride) molecules in helium buffer gas. Much of this volume will be focused on the technological development of the apparatus and technique for making and trapping cold molecules, which was the focus of my graduate work. The results will focus on measurements made on the physics of cold molecule collisions with helium and one measurement of a vibrational spontaneous emission lifetime.

Contents

Citations to Previously Published Work

Portions of this thesis have appeared in the following papers:

"Time-Domain Measurement of Spontaneous Vibrational Decay of Magnetically Trapped NH", Wesley C. Campbell, Gerrit C. Groenenboom, Hsin-I Lu, Edem Tsikata, and John M. Doyle, Phys. Rev. Lett. **100**, 083003 (2008)

"Collision-Induced Spin Depolarization of $^3\Sigma$ Molecules", Wesley C. Campbell, Timur V. Tscherbul, Hsin-I Lu, Edem Tsikata, Roman V. Krems, and John M. Doyle, Manuscript in Preparation

"Magnetic Trapping and Zeeman Relaxation of NH ($X^3\Sigma^-$)", Wesley C. Campbell, Edem Tsikata, Hsin-I Lu, Laurens D. van Buuren, and John M. Doyle, Phys. Rev. Lett. **98**, 213001 (2007)

"Buffer-gas cooling of NH via the beam loaded buffer-gas method", D. Egorov, W. C. Campbell, B. Friedrich, S. E. Maxwell, E. Tsikata, L. D. van Buuren, and J. M. Doyle Eur. Phys. J. D **31**, 307 (2004)

Acknowledgments

Shout-out to Marb, atomz, and Big Papi.

Dedicated to J. D.,
J. B.,
and J. W..

Chapter 1

Introduction and Summary

Structure of this thesis

This thesis describes the magnetic trapping and study of cold collisions of the imidogen (NH) radical. The measurements reported here were undertaken to assess the feasibility of cooling and trapping imidogen, with emphasis on understanding the underlying physics governing the relevant processes. Trapping is demonstrated, and the critical inelastic spin-relaxation NH-He cross section is measured.

The experimental work is described as taking place in two phases. First, Phase I work's primary result demonstrates the principle of beam-loading molecules into buffer-gas cell in a magnetic trapping field. Between Phase I and Phase II, the apparatus was partially rebuilt to allow lower-temperature operation and reduce liquid helium consumption. Phase II experiments utilized this newly refitted apparatus to perform cold collision measurements the imidogen radical with helium and a measurement of the vibrational spontaneous emission lifetime of NH($v = 1$).

Chapter 1 serves to present the motivation for pursuing this research and review

the state of the art up to the point where the work described in this thesis begins. Motivations for creating cold trapped samples of molecules are discussed, along with some of the techniques that are being pursued by various groups to cool and trap molecules.

Chapter 2 gives an overview of buffer-gas loading, which is the technique used for this work. The primary technical issues involved are presented to emphasize both the flexibility and the limitations of this method. The theory of collision-induced Zeeman transitions in molecules is presented in a simplified form so as to highlight salient features.

Chapter 3 provides a description of Phase I, which was partially presented in Dima Egorov's thesis [60]. The Phase I apparatus is introduced, much of which is also part of the Phase II apparatus. The results of this investigation are presented showing buffer-gas cooling of molecules in a magnetic trap and an enhancement of the lifetime of trappable molecules by the trapping field. These results demonstrated the feasibility of the beam-loading method and suggested that the addition of a refrigerator to further lower the buffer-gas temperature would lead directly to molecule trapping.

Chapter 4 describes the construction of the Phase II apparatus, which incorporates a ^{3}He refrigerator to produce lower temperatures. Much of the material here involves things that did *not* work, with the goal being to help the reader to avoid repeating the mistakes of the author.

Chapter 5 presents the results of experiments done with the Phase II apparatus. Imidogen trapping is demonstrated, and the results of cold collision measurements are covered along with analysis and a guide to how those results fit into the larger

physics context. A measurement of the vibrational spontaneous emission lifetime of $\mathrm{NH}(X^3\Sigma^-, N = 0, v = 1)$ is introduced and presented in this chapter.

Chapter 6 is the conclusion of this thesis. I have attempted to insert here ideas for useful directions for this work to take in the future, along with relevant calculations to demonstrate or refute the feasibility of each.

The appendices include calculations of the Zeeman and hyperfine effects in NH.

! Boxed text such as this includes technical information that I found to be particularly surprising or important. Boxes include content that more often than not was discovered the hard way, and may therefore be useful to future experimentalists.

1.1 Background

1.1.1 History

The field of cold molecules as an observational science begins with the liquefaction of nitrogen, oxygen, and carbon monoxide by Cailletet and Pictet in 1877 [23]. By the 1920s, Vegard had demonstrated the technique of cryogenic matrix isolation to observe the $a_u^{3+} \rightarrow X_g^{1+}$ Vegard-Kaplan intercombination line in molecular nitrogen. Detection of cold molecules in space followed in the 1930s [116]. Molecular clouds with temperatures between 10 and 20 K and densities of 10^3 cm^{-3} have been observed since the 1960s [40].

In the 1950s, the supersonic jet expansion provided the first method for creating gaseous samples of cold molecules in the laboratory [113], which largely replaced cryogenic matrix isolation as the premier method for preforming spectroscopy on

radicals. Cold molecules were also produced in superfluid liquid helium droplets [69]. Molecules in droplets can sometimes exhibit properties that closely resemble those of gas phase cold molecules.

1.1.2 Laser Cooling of Atoms

In the 1980s, the technique of laser cooling of atomic gasses was demonstrated [140], opening the door to the ultracold regime. In the two decades since then, cold atomic samples have been used in the realization of multiple quantum phases of matter [145, 70, 49], increased sensitivity of precision spectroscopy and atomic clocks [106], and quantum optics [82]. Using evaporative cooling [86], atomic ensembles are now routinely able to reach the nanokelvin temperature regime.

Laser cooling relies on the ability to rapidly repeat a cycle of absorption and spontaneous emission. Since the excitation light field is narrow-band, if the atom spontaneously decays to a different state than the original ground state, it must be "repumped" with another laser to return it to the cycling state. For many atoms, this can be done with only a few lasers, or even with one laser and a few acousto-optic or electro-optic modulators (AOMs, EOMs).

Because molecules have additional vibrational and rotational degrees of freedom, the number of decay paths to states other than the original ground state is large and has precluded the application of laser cooling to molecules, although work in this field persists [161]. The prospects for laser cooling molecules will be discussed in chapter 6.

1.1.3 Cool, Cold, and Ultracold

In atomic physics there is a precise definition of the word *ultracold*. The definition refers to the regime in which only s-wave collisions are possible. This is sometimes understood in terms of the fictitious *centrifugal barrier*.

The one-dimensional representation of an interspecies potential is commonly used for atom-atom collisions. This projection onto one dimension naturally loses information about the rotational motion of the collision complex. The relative angular momentum of the collision partners can be accounted for as giving rise to a barrier in the interatomic potentials. An example situation of an atom passing by a scattering center with a nonzero impact parameter can then be viewed in one dimension as an atom coming in, rolling part way up the centrifugal barrier, and rolling back down to the right. The ultracold regime is defined as temperatures where the height of the $l = 1$ barrier exceeds the kinetic energy of the colliding species.

For the van der Waals potential ($1/r^6$), the ultracold regime typically sets in around 1 mK. Likewise, nonpolar molecule-molecule and molecule-atom collisions generally have a similar threshold. Polar molecules, however, are different because they can possess permanent body-fixed electric dipole moments–two aligned polar molecules will interact on a dipole-dipole potential, which goes as $1/r^3$. This potential is sufficiently strong to move the ultracold regime to a few picoKelvins [140].

Despite the fact that current experiments are nowhere near the ultracold regime for polar molecule with polar molecule collisions, the term ultracold molecules is used to denote molecules colder than the typical s-wave regime for atom-atom collisions. The same terminology is also applied to ultracold Fermions, which cannot interact

with s-wave symmetry.

1.2 The Interest in Cold Molecules

1.2.1 Precision Spectroscopy

Much of the interest in the production of samples of cold molecules is similar to that for atoms. For the purposes of precision spectroscopy, it is useful to have long interaction times with the species of interest that are free from perturbing interactions and Doppler broadening. For some studies, these criteria can be met at room temperature. Vapor cells can be made with special wall coatings that preserve the coherence of the internal states of atoms upon collisions. Furthermore, by adding a buffer-gas one can increase the interaction time with the molecules of interest if such a gas does not cause the states to be perturbed too much by enforcing diffusive motion through the cell. Likewise, "Doppler-free" saturation spectroscopy can be used to circumvent the first-order Doppler effect due to the thermal motion of the molecules.

These techniques do not, however, meet the needs of most precision spectroscopy experiments. Vapor cell experiments often require that the vapor pressure of the molecule be in a narrow range, and the complicated internal vibrational structure of molecules increases their probability of sticking to the cell walls. Furthermore, there are fundamental issues with the energy scale of room temperature that are not present for atoms. First, since rotational splittings are typically on the order of 1 Kelvin, the rotational state distribution of a room-temperature sample of molecules is extremely broad, which will generally reduce the fraction of molecules in the state

of interest [59]. Second, the blackbody radiation spectrum from room temperature overlaps rotational and vibrational transitions in polar molecules, causing coupling between states and stimulating emission [88]. Finally, more subtle effects can limit precision, such as the *second*-order Doppler effect [78].

Specific proposals for utilizing cold molecules for precision spectroscopy include measurements of the time variation of fundamental constants and violation of time-reversal symmetry. Possible time-variation of the proton to electron mass ratio could be detected using homonuclear molecules [51, 209]. Since the *shape* and *depth* of the interaction potential between two atoms are sensitive to electronic properties, while the *energy spacing* between the vibrational states in that potential is sensitive to the nuclear masses, comparing two vibrational levels (with different sensitivities to m_e/m_p) provides a method for determining time variations in m_e/m_p. Similarly, time-variation of α should also be measurable in cold molecules. Stark-decelerated OH has been studied for this purpose [95].

Cold molecules can also be used to search for permanent electric dipole moments (EDMs) of fundamental particles. The strong electric fields inside polar molecules enable the production of GV/cm electric fields that can be oriented by modest laboratory electric fields (kV/cm). The relativistic electrons in heavy atoms can then experience energy shifts that are proportional to any electron EDM times the effective internal field. Furthermore, the opposite parity levels of molecules are far more closely spaced than atoms, which can dramatically increase their sensitivity to a nonzero electron EDM [97]. Stark-deceleration of YbF is currently being pursued to enhance an electron EDM measurement [96].

1.2.2 Ultracold Quantum Mechanics with Molecules

Another reason to pursue cold molecules can be described by analogy with cold atom physics. The observation of Bose-Einstein condensation [111, 43, 25], Fermi degeneracy [49], and the Mott-insulator transition [70] with atoms has yielded a tremendous amount of interesting physics. A natural extension of those systems is to replace the atoms with electric dipoles (*i.e.* heteronuclear molecules). The electric dipole-dipole interaction between molecules adds an anisotropic interaction between particles with a strength that becomes important in the density regimes of these quantum gasses [10, 169, 141].

Another aspect of the strong electric dipole-dipole interaction is that it can potentially be used for quantum computation [50, 3]. Electric dipole qubits made from polar molecules can be addressed by optical lasers or microwave fields and can strongly interact with one another to perform conditional quantum logic. In this way, polar molecules can provide the strong inter-qubit interactions necessary for quantum computation while maintaining a relatively weak coupling to the environment.

1.3 The Production of Cold Molecules

Two distinct approaches to the production of cold molecules have been demonstrated. The first, which can be called the *direct* approach, works to cool molecules that are initially hot (room temperature). The direct approach includes buffer-gas cooling [139], Stark deceleration [17], laser deceleration [66], collisional cooling [61], and mechanical slowing [75]. Here I will focus buffer-gas cooling and Stark decelera-

tion since they are the two direct approach techniques that have been demonstrated with trapping [197, 16].

The *indirect* approach, on the other hand, works to create cold molecules by associating laser-cooled atoms. The indirect approach includes photoassociation [109] as well as Feshbach resonance association [144].

1.3.1 Buffer-Gas Cooling

Buffer-gas cooling is conceptually very simple. A molecular gas may be cooled by being brought into thermal contact with something else that is already cold. Because the vapor pressure for all molecules is essentially zero at low temperatures, one cannot use the surface of a refrigerator cold plate directly to cool molecules because they will stick to its surface. Instead, buffer-gas cooling uses a cold helium vapor as a heat link between the molecular gas and a refrigerator. Since this technique is central to this thesis, it will be explained in finer detail in the next chapter and the focus in this section will be on the history of the technique.

The first realization of buffer-gas cooling to temperatures below 77 K was demonstrated by Messer and De Lucia in 1984 [139]. They used a buffer-gas cell submerged in liquid helium that was capillary-filled with CO to measure pressure-broadening parameters. In 1988 they extended this technique to 1.7 K by pumping on the helium bath [199].

Buffer-gas *loading* was inspired by the attempts as MIT to trap atomic deuterium. Work there with atomic hydrogen used a superfluid helium film to aid in collisional cooling [86]. In 1998, CaH and VO were cooled using helium buffer gas [196] and

CaH was magnetically trapped [197]. Buffer-gas loading is currently being pursued in several groups [34, 188, 176].

1.3.2 Stark Deceleration

Another way to cool atoms that are initially hot is to use a supersonic expansion to cool them in the center of mass frame of a supersonic beam and then slow down the center of mass to a standstill. This can be done with time-varying electric fields [17] as long as the time sequence is controlled precisely. Because the electric fields required are often employed with a few kilovolts, this technology was demonstrated only once the technology for high speed, high voltage switching became available[1].

Stark deceleration slows a packet of dipolar molecules by forcing them to climb a series of potential hills. High voltage (HV) electrodes create an inhomogeneous electric field in the direction of packet propagation and molecules in low-field seeking (LFS) states lose energy as they move from zero-field to this region of high electric field. The electric field is then rapidly switched off, leaving the molecules ready to climb another hill at the next electric field stage and lose more energy. The first demonstration of Stark Deceleration of molecules was made by the Meijer group in 1999 with the deceleration of CO [17]. Stark deceleration (or the closely-related *alternating gradient deceleration* [19]) is being pursued in multiple groups [17, 20, 96] and an excellent introduction to Stark deceleration is given by Rick Bethlem and Gerard Meijer in Ref. [18].

[1]MOSFET switches made by Behlke Electronic GmbH.

1.3.3 Association of Laser-Cooled Atoms

The indirect approaches of Feshbach- and photo-association have also been used to make (ultra)cold molecules. A Feshbach resonance occurs when the total energy of two species (hereafter atoms) interacting on a particular interaction potential matches a bound state of a higher energy interaction potential. This other potential may be a different relative orientation of the nuclei of the atoms (hyperfine Feshbach resonance) or any other type of potential. In Feshbach association, the upper potential has a different magnetic moment than the ground-state interaction potential, so by changing the magnetic field, the height of the bound state can be moved with respect to the ground-state interaction potential. By adiabatically lowering the energy of the bound state as the atoms interact, they can become bound with an energy lower than the dissociation threshold. This bound state is typically the most weakly-bound vibrational level of the potential, so the molecules are extremely "hot" vibrationally. Feshbach resonances between chemically distinct atoms have been seen in ^{6}Li^{23}Na [178], ^{6}Li^{87}Rb [48], and ^{40}K^{87}Rb [100]. Polar Feshbach ^{40}K^{87}Rb molecules have recently been created in an optical lattice [144] and an optical dipole trap [210]. There are currently efforts being made toward creating vibrational ground-state molecules from these Feshbach molecules.

Ultracold molecule formation by photoassociation is similar to Feshbach association in that two atoms approach each other and then form a molecule. In photoassociation, the photon frequency is tuned to couple the atoms from an unbound continuum energy state on the ground-state potential to a bound upper state, from which they may be able to decay to a bound state of the lower potential by emitting a differ-

ent wavelength photon. Because the efficiency of this process will be related to the wavefunction overlap between any states being connected, the initial unbound state typically results in a vibrationally-excited molecule, much like Feshbach-associated molecules. Photoassociation between chemically distinct atoms has been demonstrated with NaCs [76], ^{39}K^{85}Rb [137, 193], LiCs [118], and RbCs [109]. Pumping the molecules into vibrational ground states (which results in polar molecules) is the aim of much current work in this field and has been demonstrated with RbCs [166].

1.4 Trapped molecules

In order to insulate the cold molecules being studied from perturbing interactions, they can be held in a trap made of electric and/or magnetic fields. Such traps can levitate the molecules far from the walls of the vacuum chamber for extended periods of time, permitting the experimentalist to interrogate and control them with electromagnetic fields.

Not all experiments that benefit from cold molecules require traps, but it is instructive to examine when this becomes a necessary technology. The cutoff is essentially one of interaction time. If the time required to complete an experiment is longer than the size of the vacuum chamber divided by the forward speed of the molecules, a trap can be called for. Alternatively, if the time required exceeds the time between the types of collisions that prohibit making the measurement, isolation of molecules in a trap can provide long times that are free of collisions. As will be described below, most room-temperature molecules that are then cooled reach motional temperatures somewhere between 10 - 500 mK. For the relatively light molecules that have been

cooled this far, this speed corresponds to more than 1000 cm/s. Already, any experiment needing more than 1 s of interaction time is 10 m long, and the quantum computation and quantum phase transition studies described above both fit into that category. For precision spectroscopy, 100 ms of interaction time already limits the frequency precision to 10 Hz via transit broadening.

1.4.1 Magnetic Traps

A well-known consequence of Maxwell's equations ("Earnshaw's/Wing's Theorem") is that a static electromagnetic field maximum cannot exist in free space in three dimensions. A consequence of this fact for static magnetic fields is that molecules must be in low-field seeking states to be magnetically trapped in free space. The trap field will produce a potential from the Zeeman shift given by

$$E = -\boldsymbol{\mu} \cdot \mathbf{B}. \tag{1.1}$$

where $\mathbf{B}$ is the magnetic field strength and $\boldsymbol{\mu}$ is the magnetic moment of the molecule.

The trap depths attainable for paramagnetic molecules can be estimated as follows. The magnetic moment of an electron spin is approximately one Bohr magneton (μ_{B}). Molecular radicals with one or two unpaired electrons are paramagnetic and well-studied spectroscopically, so we may take as a typical value 1 Bohr magneton magnetic moment for likely trapping candidates. Static magnetic fields greater than 1 Tesla or so can be difficult to produce, so this would amount to a Zeeman shift of order 700 mK. As will be described later in this thesis, our trap is 3.9 Tesla deep and imidogen has 2 μ_{B} magnetic moment, but one can keep in mind a trap depth whose order of magnitude is 1 K for magnetostatic traps.

The first demonstrated trapping of molecules was done in our group at Harvard in 1998 [197]. CaH molecules were loaded into a magnetic trap using buffer-gas loading and spectroscopy confirmed thermalization of their translational and rotational degrees of freedom. Since then, up to the start of the work presented in this thesis, no other molecules had been magnetically trapped.

1.4.2 Electrostatic Traps

Instead of the Zeeman effect, one can also use the Stark effect to trap molecules in static electric fields. The principle is similar to magnetostatic trapping in that the molecules must be in low-field seeking states to be trapped in this way. A typical electric dipole moment for a polar molecule is 1 Debye [2], and a good practical limit for laboratory electric fields is 3 kV/cm. Gerard Meijer's group in Berlin pushes this to ≈ 10 D, 10 kV/cm, but for the parameters above, this corresponds to a trap depth of 72 mK.

Electrostatic trapping of molecules was first demonstrated in the Meijer group in The Netherlands (now in Berlin) [16] using ND_3. They have since then also demonstrated electrostatic trapping of hydroxyl radicals [189].

1.4.3 AC Electric Traps

There are significant drawbacks to trapping low-field seeking molecules that will be described in this thesis, such as the lack of LFS states, Majorana losses, and collision-induced dipole reprojection. It is therefore also possible to consider making

[2] 1 D $= 0.394ea_o = 3.34 \times 10^{-30}$ Cm $= 24$ mK/(kV/cm)

an AC trap. Because magnetic fields of order 1 Tesla usually require large inductances or large currents (and often both), AC magnetic traps have not exceeded ≈ 10 μK in depth [44].

AC electric traps, however, do not suffer from the same inductance limitation and can be made with similar technology to Stark decelerators. AC traps work by creating a field maximum along one dimension and a field minimum along another and then rapidly switching directions, in analogy to a Paul trap for charged particles. In a particular direction, the molecules will feel a force that is repulsive from the trap center and they will move away from the center. At that point, the voltages are switched and the molecules feel a force that is attractive toward the trap center, moving them closer to the center. Since the magnitude of the force will increase with the distance from the trap center, the focusing force can overcome the defocusing force if the switching frequency is appropriate.

Gerard Meijer's group in Berlin became the first to demonstrate AC electric trapping of molecules using $^{15}ND_3$ [191]. The trap depth was estimated at 5 mK and the trap volume was 20 mm^3.

1.4.4 Optical Dipole Traps

Another type of AC electric trap that has been demonstrated for molecules is the so-called optical dipole trap which is made by focusing an intense laser beam in free space. When the laser frequency is lower than the longest-wavelength transition of the trapped particles, it is known as a far off-resonance trap, or FORT. The FORT creates a maximum in the time-average of the electric field magnitude, and the trap

depth can be estimated using the trapped particle's static polarizability [183]. The lasers used for making FORTs for molecules are typically cw CO_2 lasers at 10.6 μm [184] or Yb-doped fiber lasers at at 1.06 μm [117].

One advantage of using a FORT over other types of traps is the flexibility it affords in trap species and trap location. The main drawback is the trade-off between trap volume and trap depth. Typical trap volumes are of order 10^{-4} cm^3 with depths of order 1 mK [183]. Defocusing the beam to increase the trap volume will make the trap less deep. In order to load such a trap efficiently, the molecules need to be "mode-matched" in velocity and position to the trapped distribution. This 6D mode matching is currently unavailable from direct cooling methods, mostly due to the size mismatch. In addition, it is unclear if a FORT will work well for polar molecules, since vibrational transitions are dipole allowed and may lead to scattering [184].

Chapter 2

Buffer-Gas Loading and Inelastic Collisions

A detailed explanation of buffer-gas loading is presented in this chapter, along with a discussion of typical and limiting values of relevant experimental parameters. A qualitative explanation of the theory of collision-induced Zeeman transitions is given to bring the pertinent physics to the foreground. The explanation of this mechanism for $^3\Sigma$ molecules that is examined experimentally in Chapter 5 is covered last.

2.1 Buffer-Gas Loading

In Chapter 1, the maximum trap depth for neutral molecules that was estimated was the magnetostatic trap depth of about 1 K. From this it is clear that a significant amount of cooling must be performed to bring a room-temperature molecular gas to a temperature where it can be trapped. Buffer-gas loading accomplishes this task by

bringing the molecular gas into thermal contact with a cryogenic refrigerator using the buffer gas as a heat link.

In order to choose an appropriate buffer gas, the required buffer-gas density must first be estimated in order to exclude species with insufficient saturated vapor pressures. Thermalization of 1000 K molecules to within 10% of 250 mK will take of order 100 collisions [112] with a light mass buffer species. Since the motion of molecules through the buffer gas will be diffusive, the mean-free path of molecules through the buffer-gas must be no larger than 1/10th of the size of the cell. For a cell that is a few cm in size, this corresponds to a buffer-gas density of about 10^{14} cm^{-3}. The saturated vapor densities of gasses can then be consulted to determine which gasses have sufficient density at less than 1 K.

Figure 2.1 shows saturated vapor density vs. temperature for temperatures below 5 K. The only two gasses that have high enough saturated vapor density below 1 K for buffer-gas loading are the two stable isotopes of helium, ^{3}He and ^{4}He.

Figure 2.1 also shows that there is a lower limit on the loading temperature imposed by the buffer gas. If the temperature is lowered too far, the buffer-gas density will be insufficient for thermalizing the molecules. Fig. 2.1 shows that ^{4}He becomes unsuitable below 500 mK and the ^{3}He limit is 200 mK. It can now be seen that the vapor pressure of ^{3}He and available trap depths have constrained buffer-gas loading to the temperature range of 200-1000 mK.

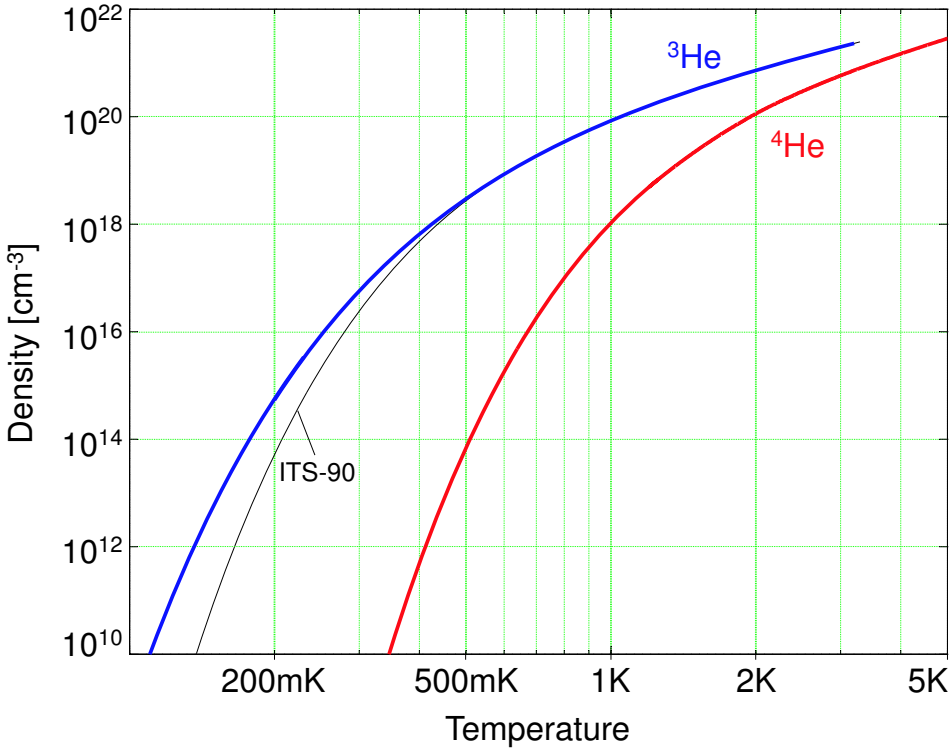

Figure 2.1: Saturated He vapor density at cryogenic temperatures. The ^{4}He curve is based on ITS-90 [147], and the ^{3}He curve is from [93] with the old ITS-90 curve shown for comparison.

2.1.1 Thermalization

Thermalization of the external kinetic energy of light molecules with ^{3}He buffer gas proceeds in about 50 collisions [112]. While this is sufficient to ensure some molecules are trapped, it does not imply thermalization of the rotational, vibrational, or electronic degrees of freedom of the molecule.

The rotational energy scale for a typical diatomic molecule is a little bit less than 1 K[1], and the bond length is of order $2a_o$. In the first rotational excited state, the

[1]Diatomic hydrides tend to have rotational constants of more than 7 K, and heavy diatomics can have rotational constants of less than 50 mK, but for this estimation we will take 1 K as a typical value.

rotational motion has $\hbar$ units of angular momentum and $B_e \approx 1$ K units of energy, which gives us an angular velocity of $\omega = 2\pi \times 40$ GHz. For a bond length of $2a_o$, this corresponds to a tangential velocity of 1300 cm/s, which is the same order as the thermal velocity of helium at 0.5 K ($\approx$ 5500 cm/s). In this sense, we cannot rigorously make the approximation that the molecular rotational motion is averaged out compared to the colliding helium atom. As such, we would expect the helium to be an efficient thermalizer of molecular rotational motion. Calculations show relaxation cross sections for this temperature range that are similar to the diffusion cross section [7, 121].

The vibrational energy scale of a light diatomic molecule is typically of order 1000 K. The vibrational motion, then, is much faster than both the rotation and the helium velocity. In this case, we would not expect the helium atom to be an efficient thermalizer of vibrational energy, and predicted and measured vibrational quenching cross sections in this temperature range are orders of magnitude smaller than the diffusion cross section [7, 198, 33].

Electronic states may be more than 10000 K, and it is important to determine if metastable electronic states will be quenched by the buffer gas. One mechanism by which this can happen is the transfer of electronic energy to the buffer gas electronic energy. Such a process will be greatly enhanced if the excited state energies are well-matched, such as in a helium-neon laser. In general, however, the He levels do not match the species of interest.

2.2 Introduction to Inelastic Collisions

A significant drawback to trapping the low-field seeking (LFS) Zeeman sublevel is that this opens an exothermic inelastic collision channel. During a collision, a stretched-state[2] LFS molecule can undergo a Zeeman transition to a less-trapped or even high-field seeking (HFS) state. The likelihood for this process must be small enough to allow thermalization of the external motion of the molecule and leave time for experiments in the trap. (A practical guideline is that γ, the ratio of the diffusive cross section to the inelastic collision cross section, needs to be at least 10^4 for buffer-gas loading.)

2.2.1 Inelastic Collisions in Atoms

All of the inelastic collision processes seen in atoms are also possible with molecules, and they are categorized here to draw attention to processes unique to molecules. Collision-induced Zeeman transitions in atoms can be induced or enhanced by spin-exchange, interaction anisotropy, Feshbach resonances, shape resonances, and three-body recombination. The last of those will not be treated here since the experiments described in this thesis are at densities far too low for three-body collisions.

In spin-exchange, an atom with a net spin can trade angular momentum with the spin of its collision partner. This is not a factor for collisions with ground-state ^{4}He since it has no spin, but the ^{3}He nuclear spin and any other atom with net angular momentum can potentially participate in spin-exchange collisions. The dominant mechanism for alkali atom spin-exchange with ^{3}He is the overlap of the alkali valence

[2] $m_J = +J$

electron with the ^{3}He nucleus, which results in a molecular-type hyperfine interaction. Spin-exchange cross sections for alkali atoms with ^{3}He at room temperature are typically 10^9 times smaller than the elastic cross section [192].

The electrostatic interaction between the atom of interest and a structureless helium atom does not couple directly to electron spin. The helium atom can, however, distort the spatial electron cloud, which is equivalent to mixing in various M_l states that weren't there before. This redistribution of M_l states would not occur for a spherically-symmetric interaction, and is therefore due to the anisotropy of the interaction with the helium atom. If the interaction causes a redistribution of M_l states, spin-orbit coupling will cause other M_S sublevels to be mixed in. It is through this mechanism that interaction anisotropy can lead to Zeeman transitions in atoms.

2.2.2 Shape Resonances

If the temperature of the colliding particles is high enough to permit non-s-wave collisions between particles, there may be quasi-bound states with nonzero angular momentum that are long-lived. The two particles stuck in such a quasi bound state can orbit each other, forming a long-lived complex that increases the likelihood of Zeeman transitions in the species of interest due to the perturbations of the other particle.

The process can be envisioned in 1D with the help of the centrifugal energy barrier, as shown in Fig. 2.2. The barrier corresponding to the relative angular momentum of the collision partners L may support a bound state below the height of the barrier but above the s-wave zero-energy threshold of the particles. In this case, an incoming

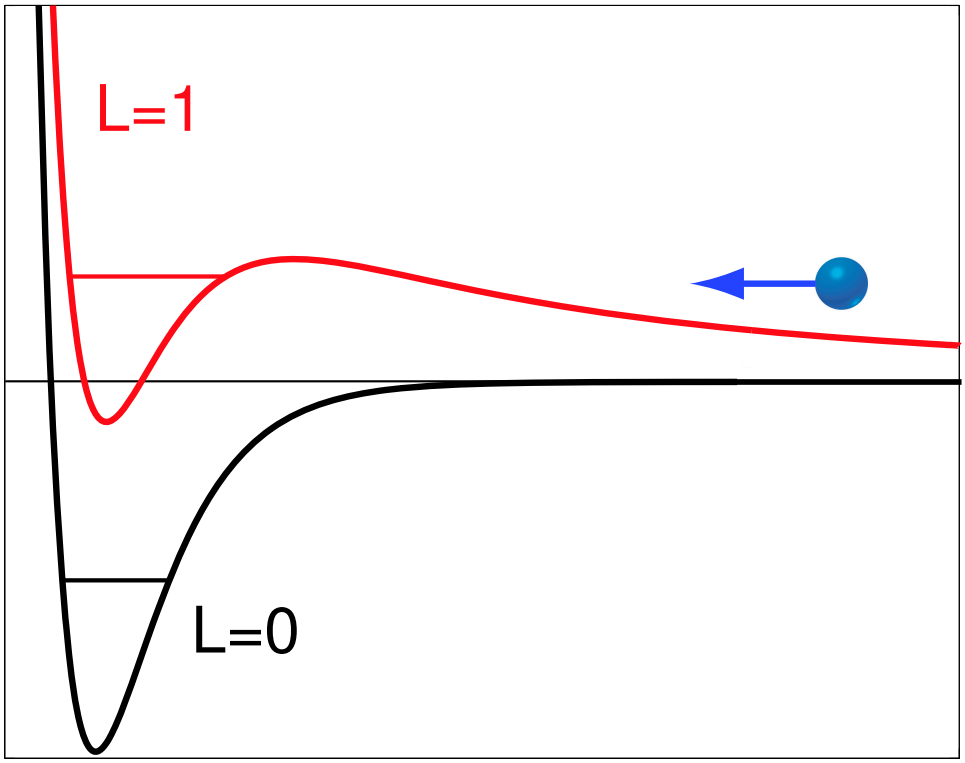

Figure 2.2: An $L = 1$ shape resonance can occur if the energy of the incoming particle matches the quasi-bound state of the $L = 1$ potential.

particle whose kinetic energy matches the energy of the quasi-bound state may tunnel through the barrier and reside in the stationary state supported by the centrifugal barrier. The lifetime of this state is limited by the tunneling rate back through the barrier, which will also determine the width of the resonance.

2.2.3 Feshbach Resonances

A so-called Feshbach (or Fano-Feshbach) resonance can occur through coupling to a true bound level of a higher-energy state of the collision complex. If the total energy of this bound state matches the energy of the colliding atoms, an enhancement of the inelastic rate can occur.

Feshbach resonances have come into prominence in the field of cold molecules due to their usefulness for making cooler molecules out of laser-cooled atoms, as discussed in Section 1.3.3.

2.3 Inelastic Collisions with Molecules

All of the mechanisms described above for atoms can also lead to spin-depolarization (inelastic collisions) of diatomic molecules. The rotational degree of freedom possessed by molecules, however, introduces new Zeeman relaxation mechanisms not present for atoms. This degree of freedom is described by the rotational wavefunction, which gives the probability amplitude for finding the internuclear axis pointing in a particular direction on the lab-frame. It is the distortion of this angular wavefunction by the electrostatic interaction with the helium atom that dominates inelastic collisions in molecules.

Spin-depolarization of Σ molecules was formally examined by Krems and Dalgarno [120] for both doublet and triplet states. From an external perspective, the dominant spin-depolarization mechanism for $^2\Sigma$ and $^3\Sigma$ molecules is similar. As depicted in Fig. 2.3, the molecule starts out in the fully stretched LFS state before colliding with a helium atom. The helium atom may approach closely enough to distort the rotational wavefunction, or, in the case of $^3\Sigma$ or rotating molecules, the rotational wavefunction may already be nonspherical. An internal molecular interaction between rotation and spin can then cause a Zeeman transition. It is the nature of this internal coupling between rotation and spin that is so different for $^2\Sigma$ vs. $^3\Sigma$ molecules, and the mechanism responsible sets the magnitude and scaling behavior of the inelastic

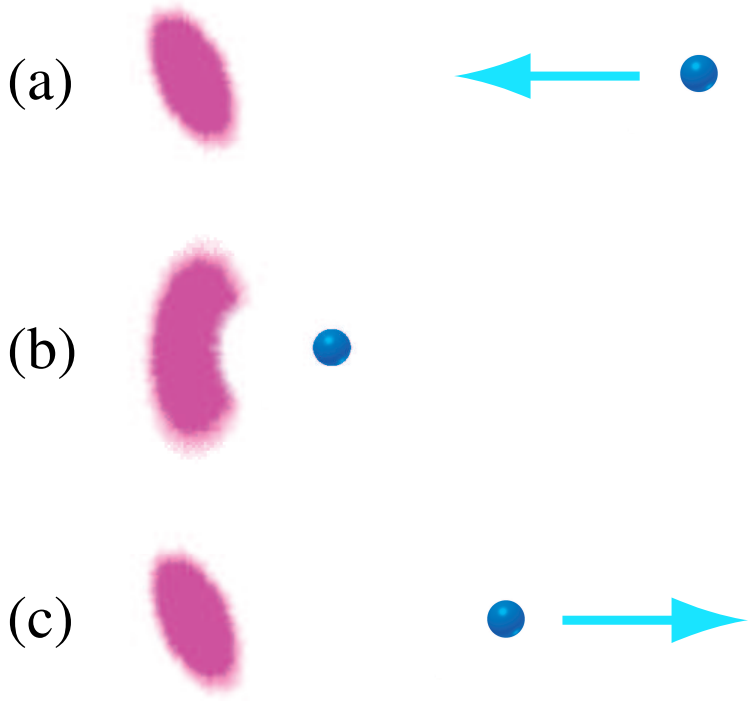

Figure 2.3: Distortion of a wavefunction by a colliding helium atom. In the case of atoms, this wavefunction could be an electron cloud. For molecules, the relevant spatial distribution is the rotational wavefunction for nuclear motion.

cross section.

2.3.1 Inelastic Collisions in $^2\Sigma$ Molecules

For molecules in non-Σ states, the rotational wavefunction is already highly non-spherical and collision-induced Zeeman relaxation is predicted to be rapid [74]. The Λ-type splitting is also typically less than 1/10th of a wavenumber, so collisions are likely to mix in the opposite parity Λ-doublet state. These types of collisions are

very accessible at temperatures appropriate for buffer-gas cooling. The mechanism at work is essentially the same as the spin-orbit driven relaxation described for atoms.

For Σ states, however, the nearest state to be mixed in by electrostatic perturbations will be the first rotationally excited state, which can be more than 10 K above the ground state. As with atoms, the electrostatic interaction between the helium atom and the molecule does not couple to the electron spin. In order to change the spin projection M_S, there must be a mechanism by which the spin can be coupled to something that can be altered by the electrostatic interaction.

The spin-rotation interaction $\gamma_{\rm SR}\mathbf{N}\cdot\mathbf{S}$ seems a natural choice for just such a mechanism. It can couple states with the same value of the sum $M_S + M_N$, which are the projections of the molecular spin and rotation on the lab-fixed Z-axis. This can be seen immediately with the use of the following identity:

$$\gamma_{\rm SR}\mathbf{N}\cdot\mathbf{S} = \gamma\left(N_z S_z + \frac{1}{2}\left(N_+ S_- + N_- S_+\right)\right). \tag{2.1}$$

The inner product $\mathbf{N}\cdot\mathbf{S}$ depends on the relative projection of $\mathbf{N}$ and $\mathbf{S}$, so all states with the same value of $M_J \equiv M_S + M_N$ will have the same energy under the $\gamma_{\rm SR}\mathbf{N}\cdot\mathbf{S}$ interaction and can be coupled by it. An important consequence of this is that for the rotational ground state, $N = 0$ implies that $M_N = 0$ so the spin-rotation interaction cannot change M_S without changing M_J, which is forbidden. Collisions between helium atoms and fully ground-state $^2\Sigma$ molecules cannot directly cause spin-depolarization, and first-order perturbation theory will predict a Zeeman transition probability of zero.

Despite these considerations, there is a three step process by which the electrostatic interaction of the colliding helium atom and the spin-rotation interaction in

the molecule can cause spin depolarization. Even though the electrostatic interaction cannot couple to the electron spin, electric fields can mix rotational states. That means that the helium atom can perturb the rotational state distribution from pure $N = 0$ into a mixture of N states during the collision. In the second step, the spin-rotation interaction can mix in different M_S states from the $N > 0$ portion of the rotational eigenstate that is perturbed by the proximity of the helium atom. Finally, the electrostatic interaction between the helium atom and these mixed states will have off-diagonal elements in M_J, which lead to spin-depolarization.

2.3.2 Inelastic Collisions in $^3\Sigma$ Molecules

The mechanism described above developed by Krems and Dalgarno [120] will still be present for $^3\Sigma$ molecules. As they have pointed out, however, the addition of the spin-spin interaction in $^3\Sigma$ molecules leads to another relaxation channel that tends to dominate the spin depolarization.

As mentioned in Sec. 2.3.1, the electrostatic interaction from the helium cannot cause Zeeman transitions for a pure $N = 0$ rotational ground state, which is why first order perturbation theory was insufficient for describing $^2\Sigma$ Zeeman relaxation. One way to see this is to note that the rotational wavefunction for $N = 0$ is spherically symmetric, so there cannot be any directly anisotropic interactions to re-orient the molecule.

The ground state of a $^3\Sigma$ molecule, on the other hand, is not a pure $N = 0$ state, even in zero field. The spin-spin interaction mixes in some $N = 2$ character. The ground state will be a mixture of $|N=0, M_S=+S\rangle$ and various $|N=2, M'_N, M'_S\rangle$

states. Here it can be seen mathematically that the spatial orientation of the internuclear axis on the lab frame is coupled to the projection of the electron spin through the spin-spin interaction. The amount of $N = 2$ present will depend on λ_{SS}/B. This theory indicates that it is therefore desirable for a $^3\Sigma$ molecule to have a large rotational constant to minimize collision-induced Zeeman relaxation. This theory is one of the factors that led us to the NH radical, described in Section 3.1

So for $^3\Sigma$ molecules, the helium atom can again approach the ground state atom and distort the spatial rotational wavefunction. In this case, however, first order perturbation theory will work since there will now be elements of the interaction Hamiltonian that are off-diagonal in M_J, leading directly to Zeeman relaxation. This mechanism is likely to dominate for molecules for which the spin-spin coefficient (λ_{SS}) is larger than the spin-rotation coefficient (γ_{SR}), which is true for the imidogen radical.

It is not clear from this qualitative model whether the additional 1 μ_B of magnetic moment gained in moving from $^2\Sigma$ molecules to $^3\Sigma$ states is worth the trouble. If the spin-spin driven Zeeman relaxation for $^3\Sigma$ molecules is too strong, the trap lifetime will be strongly limited by inelastic collisions and not the trap depth. In 2003, a quantitative calculation was performed by Krems *et al.* that predicted a favorable Zeeman relaxation rate coefficient for imidogen with helium [45, 121]. Furthermore, experiments performed in our group indicate that thermal isolation of $2\mu_B$ species is dramatically easier than $1\mu_B$ [79]. These considerations encouraged us to pursue a $^3\Sigma$ molecule with large rotational constant for buffer-gas loading.

Chapter 3

Phase I: Magnetic-Field Enhanced Diffusion Lifetime

The Phase I apparatus and imidogen radical are introduced, followed by results from Phase I. The molecular beam was coupled into the buffer-gas cell in the magnet bore with the trap field on. The Phase I buffer-gas cell was simply the semi-sealed magnet bore, and the minimum temperature reached was about 2 K. The detection systems used are also introduced, along with some unanticipated light production in the cell (magnetic-field stabilized discharge glow). Hyperfine spectroscopy was performed in the cell without buffer gas and Zeeman spectroscopy was accomplished with buffer gas. The magnetic trapping field is shown to enhance the lifetime in the cell by a factor of two, as expected. This result demonstrated the feasibility of the beam-loading process and provided sufficient evidence that trapping should be possible to begin construction of Phase II.

3.0.3 Molecular Beam Test Phase

The first cryogenic test of loading a buffer-gas cell from a molecular beam was described in Dima Egorov's thesis [60] and will not be described in detail here. Briefly, the production of an imidogen molecular beam by a DC glow discharge of ammonia was demonstrated. This was motivated by the unpredictability of laser ablation as a source of molecules for buffer-gas loading. Molecules were detected with a residual gas analyzer (RGA) and the beam was then loaded into a buffer gas cell. In the cell, laser-induced fluorescence (LIF) and laser absorption detection were performed to verify the number and temperature of the cold molecules. $10^{11} - 10^{12}$ imidogen radicals were cooled to a translational temperature of less than 5 K. There was no trap magnet present for this test phase. Phase I consists primarily of the integration of the molecular beam with the trap magnet.

3.1 Imidogen

Magnetic molecules are highly reactive chemically. The magnetic moment essentially arises from unpaired electrons, which give the molecule a net spin angular momentum, but which also make production of such molecules difficult. One notable exception to this production rule is the ground-state oxygen molecule, which is highly reactive, but not with itself. It is also so abundant that after reacting with everything in sight (thus passivating container walls and the like) there is still some left over for experiments.

As discussed in Section 2.3.2, we sought out molecules that had $^3\Sigma$ ground states

Table 3.1: Spectroscopic Constants for NH (in cm^{-1}). Constants for $X^3\Sigma^-$ from [153], for $A^3\Pi_i$ from [27]

cm^{-1}		$X^3\Sigma^-(v=0)$	$X(v=1)$	$A^3\Pi_i(v=0)$	$A(v=1)$
Vibration	ω_e	3282.72		3232	
	$\omega_e x_e$	79.04		98	
Rotation	B_v	16.34	15.70	16.32	15.58
Spin-Spin Interaction	λ_{SS}	0.9199	0.9200	-0.1997	-0.2007
Spin-Rotation Interaction	$\gamma_{\rm SR}$	-0.0549	-0.0518	0.0298	0.0285
Spin-Orbit Interaction	A_v			-34.620	-34.649
Internuclear Separation	r_e	$1.96000a_o$		$1.95917a_o$	

and large rotational constants. This essentially limited us to considering hydride molecules from the nitrogen column. After looking at factors such as health risks associated with each precursor, NH was an obvious choice. Gerard Meijer's group first pointed out the imidogen radical as a possibility for us, and closer investigation revealed that it had many of the properties we desired.

The radical is know by a few names (NH, imidogen, nitrogen monohydride, imine) and has been well-studied spectroscopically due to its importance in astrophysics [127, 71, 134], combustion flames [42], the earth's atmosphere [29] and chemistry [90].

3.1.1 Spectroscopy

The spectroscopic constants for the states of interest to this thesis are listed in Table 3.1 and a diagram of the $A \leftrightarrow X$ electronic transition is shown in Fig. 3.1.1. The potential curves of of the X and A states are remarkably similar, as can be seen by comparing their equilibrium internuclear separations and vibrational constants. This coincidence results in a highly diagonal Franck-Condon array due to the good overlap between the vibrational wavefunctions with the same value of v. Furthermore, the internuclear separation is quite small (compare to r_e =

3.80, 2.70, 2.90, 3.25, 3.41, and $2.28a_o$ for CaH [45], PH [180], AsH, SbH, BiH [94], and O_2 [85], respectively). This should reduce the anisotropy of the NH-He interaction potential surface and therefore further suppress collision induced Zeeman relaxation.

The $X^3\Sigma^-$ ground state is well-described by Hund's case (b) [186], which means that the spin is not strongly coupled to the internuclear axis. In the $A^3\Pi$ state, spin-orbit coupling tends to couple the spin to the internuclear axis. Table 3.1 shows that the ratio of the spin-orbit to rotational constant is $A/B = -2.12$, which puts the $A^3\Pi$ state into the intermediate regime between Hund's case (a) and (b).

3.1.2 Zeeman Effect

Since the imidogen radical is a $^3\Sigma$ ground state, it should have a magnetic moment of $2\mu_B$ from the two aligned electron spins. In the high-field limit where M_S and M_N are good quantum numbers, Herzberg [85] gives the magnetic moment for Hund's case (b) to be

$$|\boldsymbol{\mu}| = \frac{\Lambda^2 M_N}{N(N+1)}\mu_B + 2M_S\mu_B. \tag{3.1}$$

For X-state NH the first term is zero since $\Lambda = 0$ and we get a $2\mu_B$ magnetic moment.

If we apply this Hund's case (b) equation to the $A^3\Pi_2$-state, we obtain magnetic moments of $2.5\mu_B$. For $^3\Pi_1$ in the $R = 0$ ground state, $N = \Lambda$ and we have an equal superposition of $|1,0\rangle$ and $|0,1\rangle$ in the $|M_N, M_S\rangle$ basis, giving us a magnetic moment of $1.25\mu_B$. In the $^3\Pi_0$ rotational ground state we have an equal superposition of $|+1,-1\rangle$ and $|-1,+1\rangle$, giving us $0\mu_B$. The multiplet splitting between the $A^3\Pi_2$ and $A^3\Pi_1$ rotational ground states is approximately A, while rotational splitting for

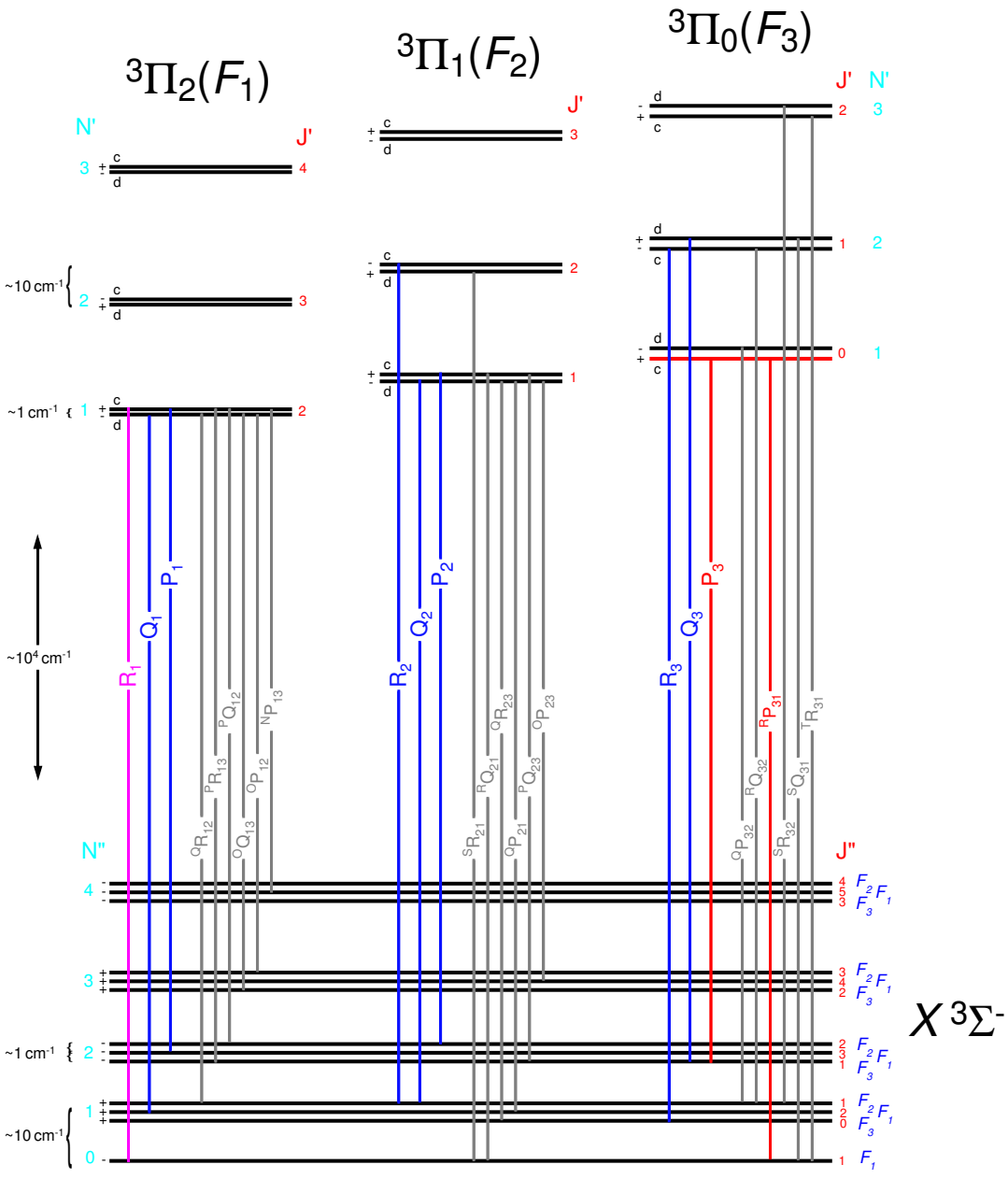

Figure 3.1: The $A^3\Pi \leftrightarrow X^3\Sigma^-$ electronic transition of NH following the notation of Dixon [54]. NH spectroscopy for this work is performed on the R_1 transition.

2 is approximately $4B_v$. We can therefore expect the case (b) formula (Eq. 3.1) to give a reasonably good description of the magnetic moment of the excited state. A more exact calculation of the Zeeman effect in NH is given in Appendix A.

3.2 2 Kelvin Apparatus

The decision to pursue loading NH into the magnetic trap field at temperatures higher than those required for trapping was made because the technical challenges associated with getting the molecules into the trap region are significant. The molecular beam source has to be be connected to the cryogenic dewar vacuum and operated without causing substantial cryogen boiloff. The magnet needs to be run in vacuum to make the magnet environment compatible with molecular beams. Furthermore, the buffer-gas cell aperture will potentially cause escaping helium to soften the dewar vacuum and scatter molecules out of the beam before they enter the trapping region. All of these complications were addressed satisfactorily, which enabled the observation of cold molecules in the magnetic trapping field.

3.2.1 Molecular Beam Source

The molecular beam source used for the Phase I apparatus was essentially the same as the beam-loading demonstration experiment and is discussed in detail in Dima Egorov's thesis [60]. Briefly, the beam source is centered around a pulsed valve[1] with a Kel-F or Vespel poppet and a stagnation gas containing ammonia. Just outside the nozzle is a high voltage gap that causes a DC glow discharge when the

[1] General Valve Series 9

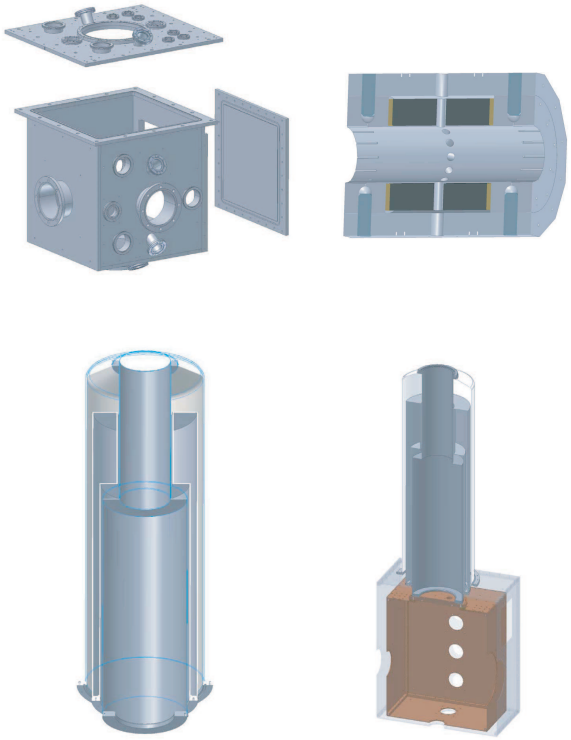

Figure 3.2: Upper left: The so-called "spider box" vacuum chamber that houses the trap. The molecular beam enters from the left. Upper right: cross-sectional view of the trap magnet. The NbTi coils are shown in black. Lower left: cross-sectional view of the dewar. The helium bath holds 30l of liquid when full to the neck. Lower right: The blackbody radiation shields connected to the dewar. The 77K shield is shown as transparent, the 4K shield as copper. Both are mechanically and thermally connected to the dewar.

gas density is high enough. The valve is magnetically actuated, so a compensation coil was required to reliably operate the valve near the magnet. The minimum open-to-close time for this valve is of order 2 ms for a sustainable and repeatable discharge.

3.2.2 Magnet

The trap magnet for this experiment is described in detail in [80, 60][2]. Briefly, the magnet is made from two symmetric coils of NbTi superconducting magnet wire wound around a form we call the bobbin. The magnet bobbin is machined from Grade 6 titanium alloy ("Ti 5-2$\frac{1}{2}$"), which begins superconducting around 3 K [80].

The field produced by the two coils is referred to as a "spherical quadrupole field," and is the favored configuration for the deepest magnetic traps. The field minimum is a field zero positioned directly between the coils and the field magnitude increases linearly in all directions. The contours of equal field magnitude are oblate spheroids with an aspect ratio of 2 such that the "pancake faces" point along the axis of the magnet and the edges of the pancake eventually intersect the I.D. of the magnet bore.

Buffer-gas Cell

The temperature of the buffer-gas in the Phase I apparatus was only capable to being lowered to the temperature of the helium bath. Since this is also the temperature of the magnet, it was decided to simply have the bore of the magnet serve as the buffer-gas cell. The magnet bore was sealed (except for the 3 mm diameter molecular beam entrance aperture) with indium and grease seals. LIF was still excited and collected at the magnet midplane, where the seals to the magnet midplane holes were made using titanium window (or lens) holders with silicone vacuum grease. These holders utilized fin-type strain relief for the epoxy seal between the fused silica and the titanium alloy.

[2]It is referred to as the "Mark 5" magnet in [80]

The molecular beam entrance aperture was made in the end of the charcoal tube (see Section 3.2.5), which was reentrant into the magnet bore. The axial position of this hole was chosen to be at the magnetic-field saddle point to ensure that thermalized molecules could be trapped while not lowering the trap depth.

3.2.3 Vacuum System

The main vacuum chamber for the experiment is called the "spider box" due to its resemblance to a spider and the fact that when we opened the crate a spider crawled out. The chamber is essentially a 1 m stainless steel cube with a separate top face. The dewar attaches to the to place through a large diameter flange and the cold parts of the dewar hang down into the spider box. In "normal" operating mode, the spider box hangs from the ceiling and the rest of the spider box can be lowered away for working on the inside. In this way we are able to gain access to the business end of the trap from five directions, which has provided tremendous flexibility in terms of unforeseen additions and changes to the experiment.

The spider box itself is connected to two pumping systems. For pumpdown and use while warm enough to pump ammonia gas we have a pump charged with PFPE pump oil.

! The gas ballast on the PFPE pump should remain open. This will cause a reduction in the base pressure of the pump and may cause it to make more noise, but condensation of water or ammonia in the pump due to closure of the ballast has caused the pump to fail and require factory repairs.

There is also a turbo pump connected to the spider box that is backed by a diaphragm pump. This pump is dry, so it is compatible with the higher vacuum applications, such as finishing a pumpout before cooling down the dewar.

3.2.4 Dewar and λ-fridge

The dewar itself is capable of holding 33 l liquid helium and 22 l of liquid nitrogen. The nitrogen bath is a "jacket" that surrounds the helium bath except for the lowest 1 inch.

! With the addition of the pulse tube cooler (described in Section 4.1), the experiment maintenance while cold is limited by the size of the nitrogen bath. The hold time of the helium bath is about 2 days, but the nitrogen bath boils off in 18-20 hours. Future experiments similar to this one should have nitrogen baths of 50 l or more.

The neck of the helium bath is a full 6 in I.D. to accommodate the retrofitting of a commercial helium-3 fridge, which was never implemented. Helium vapor that boils off from the bath is confined to rubber hoses through holes in the top plate that connect to the helium exhaust system in the lab. This eliminates stray helium gas in the room, which can corrupt PMTs and lower the sensitivity of helium leak checking. The top plate is held onto the dewar with springs to allow a high-conductance path for vapor to escape in the event of a catastrophic rapid boiloff of helium.

Inside the helium bath there is a device called the λ-fridge. This is essentially a coil of copper tubing that sits in the bottom of the helium bath and has a large-diameter pumping line that leads straight up and out the top of the dewar. At the other end of the coil there is a tunable impedance for sipping helium from the bath. The λ-fridge is used to cool down the helium bath below 4.2 K without having to pump on the whole bath, which would interfere with the proper operation of the vapor-cooled leads.

The tunable impedance permits a significant pressure drop between the atmospheric pressure bath space and the coil, which is pumped by a mechanical pump at

room temperature. This pressure drop results in a significant reduction in temperature (see Fig. 2.1) for the helium in the coil, and the OFE copper tubing can conduct heat from the bath to the enthalpy of the vapor inside the coil. The result is a cooling of the bottom layer of liquid in the bath. Since this colder helium is more dense than the 4.2 K portion, the cold helium stays at the bottom of the bath in contact with the dewar cold plate. Our λ-fridge is capable of cooling the cold plate to just above the λ-point.

! The extra resources associated with making the impedance at the bottom of the λ-fridge adjustable were worth the effort for two reasons. During cooldown and even while running in steady-state the optimal impedance changes dramatically, so having the ability of adjust it pays off in cooldown time. Furthermore, as we learned with our homemade ^{3}He fridge, there tends to be some solid stuff floating around in the liquid that gets pulled into pumped systems and will easily clog tight impedances.

There is a room-temperature baratron reading the pressure of the pumping line just outside the dewar and we find empirically that the fridge achieves the lowest base pressure when this gauge reads 21.8 mbar.

3.2.5 Charcoal Sorption Pumping

The vacuum system already described can provide hundreds of liters per second pumping speed on the manifolds exposed to room-temperature pumping ports, but has poor conductance to much of the business end of the apparatus. In particular, if the region just outside the cell orifice (which is recessed about 5 in into the magnet bore) has too high a helium density, the molecular beam will be attenuated before it gets to the cell. Furthermore, helium gas loads will tend to soften the dewar vacuum, by which it is meant that any helium gas between two surfaces of different

temperatures will tend to bring them into thermal contact with one another.

To combat this problem, we employ the use of charcoal sorption pumps, often called "sorbs." Charcoal is organic material (usually wood, but sometimes coconut shells or even bone) that has been heat-treated to remove its water. This produces a remarkably porous material with pores ranging from the visible to molecular size scale. This produces and tremendously large effective surface area for gas adsorption ($\approx$ 1000 m^2/g [171]). When the charcoal is cooled to below 40 K or so, helium gas will tend to stick to its surface. At 4 K, this sticking probability is so high that the effective pumping speed can be more than 6 l/s per cm^2 apparent area [171]. The total amount of gas that can be pumped by a fixed amount of cold charcoal is approximately equal to 10%-100% the apparent volume of charcoal in liquefied gas. So 1 cc of charcoal can pump of order 100 cc of helium gas.

! Charcoal pumps large quantities of gas by having a gas molecule stick to its apparent surface area and then move into the bulk through 2-D surface diffusion. It has been noted [133] that 2-D diffusion will stop working below a certain critical temperature, so the charcoal actually stops pumping well if it gets too cold. Our experience is that this happens between 2-3 K for helium.

When the charcoal begins to reach its maximum capacity of adsorbed gas, the pumping speed will decrease and it becomes necessary to "regenerate" the sorb. This is accomplished by heating the sorb to $\approx$ 40 K while pumping with some other pump to get rid of the desorbing gas. It is also possible for the sorb to regenerate itself automatically if the desorbing gas can bounce off a surface significantly hotter than the sorb. A hot helium atom can hit the full sorb and cause a few other (cold) helium atoms to desorb, which can then heat up by hitting the hot surface and then hit the sorb again, causing even more atoms to desorb. This type of "spontaneous

regeneration" can happen an inopportune times if one is not careful to keep the sorbs from filling up. Once a spontaneous regeneration starts, it will generally not stop until the sorb is fully regenerated.

To pump helium inside the 4 K shield, a sorb essentially covers the bottom inside surface of the shield. This sorb is named the "mothersorb" and is thermally connected to the 4 K shield by brass standoffs. Using the numbers above, the helium pumping speed of this sorb should be in excess of 10^4 l/s, though we have never attempted to measure this.

To keep the helium density low just outside the cell in the magnet bore, a copper tube coated with charcoal (called the "charcoal tube") was installed in the region and thermally-connected to the magnet bobbin. We see the loading efficiency of our apparatus decrease after about 20 sccm*hr of buffer-gas flow, which we attribute to the filling of the charcoal sorb by helium. Regeneration of the charcoal tube fixes this problem.

Sedgley *et al.* [171] found that the best pumping speed for the charcoal-helium system could be achieved with the charcoal silver-soldered to the copper. I was able to get a good mechanical bond by coating the top side of the copper with Stay-Silv 15 (J. W. Harris Co., Inc. Part #61035. This is essentially plumbers' solder.) and then sprinkling charcoal on the surface, followed by heating with a torch on the underside of the copper until the charcoal started glowing red. I was not able to test the performance of this method against our standard Stycast 2850 method.

Construction of a Charcoal Sorption Pump

This subsection is a brief description of how we make our charcoal sorbs, intended for people who do not have extensive cryogenics experience.

The substrate is typically made of copper 101 to ensure that the heat of adsorption

is carried away from the charcoal rapidly enough to allow it to keep pumping. For calculational purposes, it is reasonable to assume that the heat of adsorption is about 2.5 kJ/mol. Typically, 1/4 inch thick C101 plates no bigger than 4x4 inches are sufficient.

The charcoal we use is manufactured by Spectrum and is made from coconut shells. It is called coconut activated charcoal (CAS 68647-86-9) and we use mesh size 8-30. Do not expose this charcoal to large amounts of water as wet charcoal will preferentially absorb oxygen from the surrounding air.

To attach the charcoal to the copper, we paint epoxy onto the part of the copper we want to cover (leaving room to thermally and mechanically connect the edges of the plate where necessary), applying a liberal amount with a small brush. The epoxy is a special cryogenic epoxy from Emerson & Cuming designed to be thermally conductive and expansion-matched to copper. It is called Stycast 2850FT BLACK and we use this with catalyst 24LV, mixed in a ratio of 100:7.5 by weight.

We then sprinkle charcoal onto the coated copper, relying on gravity to cause the charcoal to contact the epoxy. The sorb should then be allowed to cure in a safe dry area for about 12-24 hours.

Initially, pumping on a chamber that has a sorb inside will actually cause the sorb temperature to drop due to the extracted latent heat, which we presume is water leaving the sorb. Pumping of helium will start around 40 K.

3.2.6 Laser-Induced Fluorescence Detection System

The molecules are detected using the $A \leftrightarrow X$ transition. The short wavelength (336 nm) and fairly long lifetime (τ = 440 nm) of this transition make it more difficult to detect in absorption than typical atomic species. As such, we performed fluorescence detection using a CCD camera with an MCP image intensifier[3] for the beam-loading demonstration experiment that preceded Phase I [58, 60].

In the first attempt to detect NH in the magnet bore, we tried to use this same camera. Since we excite and detect on the same wavelength, stray excitation laser scatter cannot be filtered out spectrally. Furthermore, to maximize the optical access to the excitation region, we positioned the camera to look into the cell from the back, so that it faces the molecular beam source. We had hoped to be able to trigger the camera after extinguishing the discharge. It turned out that the discharge glow lasted too long for this (see Fig. 3.5). The camera setup and its problems are discussed in Dima Egorov's thesis [60].

To avoid the problems of stray light scatter and discharge flash, we switched to a new geometry with a photomultiplier tube[4] (PMT) as our photon detector, as shown in Fig. 3.3. The PMT has a bialkali photocathode and an internal voltage gain stage so that it only requires ±5 V. The fluorescence collection lens was moved to be radial at the midplane (instead of axial at the back of the cell, as with the camera).

We perform our LIF detection using the PMT in photon-counting mode. This has been done using either a pair of counters[5] or a multi-channel scaler[6] (MCS). We amplify the signal from the PMT using a fast preamplifier[7] before pulse counting.

The molecular beam dissociation discharge causes electrical pickup in the signal coming from the PMT. The pickup lasts as long as the discharge is on and consists of a

[3]Princeton Instruments ITE/CCD
[4]Electron Tubes Limited, P25A-02
[5]Stanford Research Systems SR620
[6]Stanford Research Systems SR430
[7]Stanford Research Systems SR445A

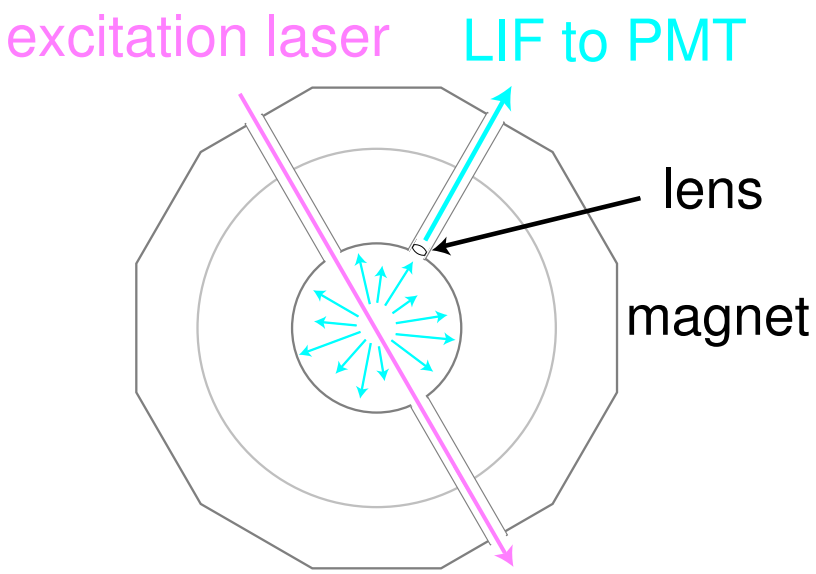

Figure 3.3: Laser-induced fluorescence (LIF) collection geometry for the PMT. The magnet midplane is shown in cross section, without the buffer-gas cell. The excitation laser crosses the center of the trap and molecules fluoresce isotropically. The center of the trap is imaged onto the face of the PMT using the lens shown and another lens at room temperature.

series of voltage oscillations with 10 ns period that are roughly symmetric about 0 V. This is clearly not photons hitting the PMT face since there is a large negative-voltage component. Grounding the PMT body had no effect.

We use the counters for maximum sensitivity in low signal conditions, such as free-flight beam detection. The excitation laser is chopped with an AOM and RF switches are used to ensure that one counter counts the photons while the laser beam is on (the reference counter) and the other counts photons after the beam has been turned off (the signal counter). The reference counter is then used as a gauge of the laser intensity for normalization of the signal counter data. An MCS trace of the AOM-chopped PMT signal with no molecular beam is shown in Fig. 3.4. It is clear from Fig. 3.4 (b) that the AOM extinguishes the beam on a timescale similar to what

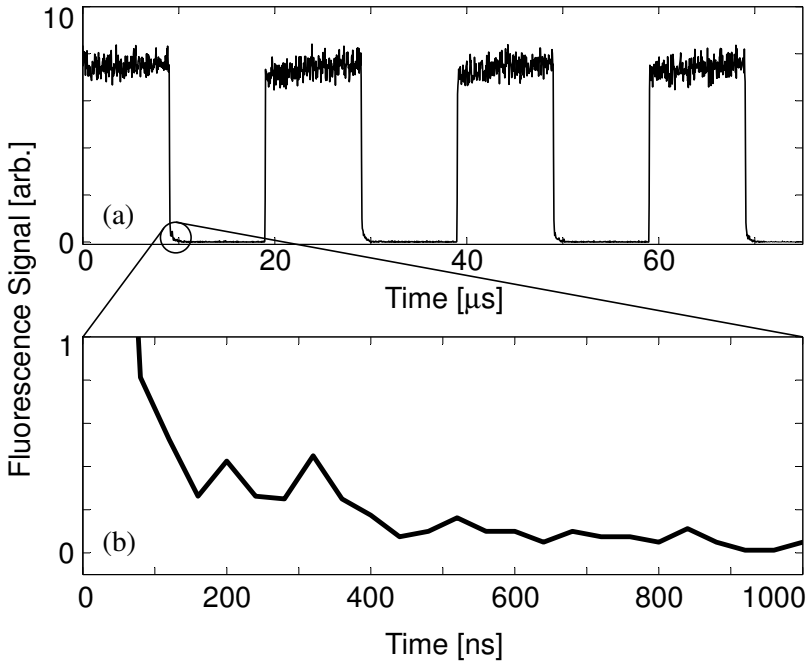

Figure 3.4: Laser-induced fluorescence (LIF) from the cell collected by the PMT while the excitation beam is being chopped by the AOM with no molecular beam. (a) The laser scatter causes a high count rate while the beam is on and a low count rate while the beam is off. (b) Close up of the decay of the signal tail showing that the AOM extinguishes the beam on a timescale of about 500 ns.

is expected from the 440 ns radiative lifetime of NH, which complicates data taking. Despite this, high signal-to-noise data were obtained using this method due to the large number of molecules in the cell and the repeatability of the AOM rolloff. Good signal in free-flight conditions were typically 5-10 signal photons per valve pulse.

The counter scheme can make it difficult to obtain temporal information and is mostly useful for obtaining spectra. The MCS, however, is better suited to time profiles since it provides the number of counts in sequential time bins. We do not typically chop the beam with the AOM for the MCS detection, which reduces the signal-to-noise compared to the counters. Most of the data for Phase I was taken with the counters, while most of the Phase II data was taken with the MCS.

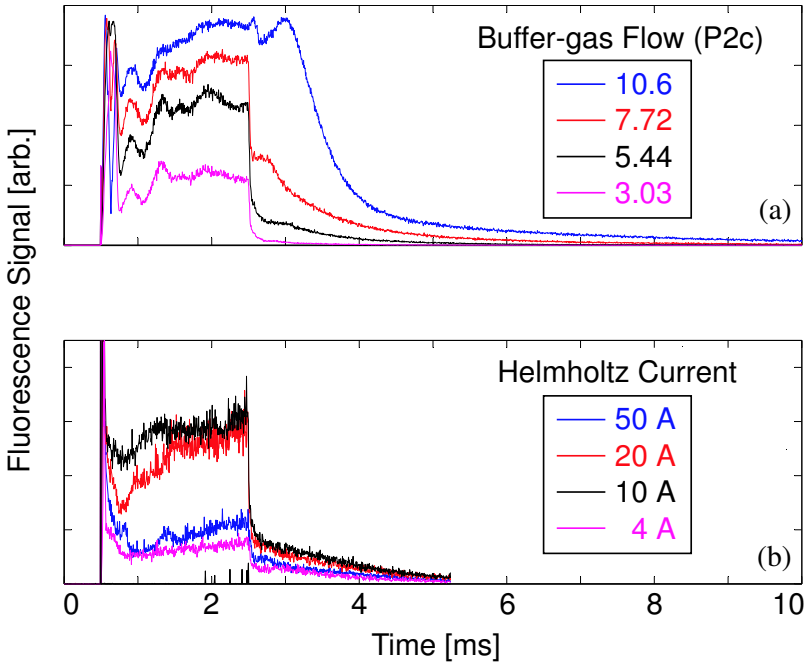

Figure 3.5: PMT signal showing the signal generated by the discharge. (a) Dependence on buffer-gas flow rate (units are reading on gauge "P2c") for a Helmholtz magnet current of 0.93 A. (b) Dependence on Helmholtz magnet current for a buffer-gas flow rate corresponding to P2c reading 1.15.

Magnetic-Field Stabilized Discharge

Fig. 3.5 shows the PMT signal under conditions of buffer-gas flow and Helmholtz magnet current. The discharge produces light that persists after the discharge voltage has been turned off at $t = 2.5$ s, and the amount of light increases with buffer-gas flow. The units for the flow are the uncalibrated readings of gauge "P2c," but a reading of 5.44 is typical of good signal in the buffer gas. Fig. 3.5(b) shows the effect of the magnet on the discharge, which works to "stabilize" the light production.

We believe that this is caused by the magnetic field focusing charged particles into the bore of the magnet, where they can continue to collide with helium atoms and cause light emission. The flash is worst under conditions of both buffer-gas flow and

magnet current, which is our operating mode. As a separate test, we measured that the magnetic field causes our PMT count rate to decrease by 8.4% at a Helmholtz current of 50 A.

3.3 Results

Before turning on the magnetic field or flowing buffer gas into the cell we were able to spectroscopically study the beam using LIF. Some of the hyperfine structure of NH is resolvable in these spectra and fits well to a simulated spectrum. The addition of buffer gas caused this spectrum to broaden into a Doppler profile consistent with 4 K. The addition of the magnetic field (in "Helmholtz" configuration) enabled Zeeman spectroscopy of the cold molecules that matched well with calculations. Finally, the $1/e$ lifetime of the molecules in the trapping region was seen to be enhanced by the anti-Helmholtz magnetic field, which may be called incipient trapping.

3.3.1 Detection of NH in the Magnet Bore

The first step that was taken toward loading the trap was to verify that the molecular beam is reaching the trap region. If the gas load from the beam itself is degrading the vacuum in the regions the molecules must traverse ballistically, it is possible that very few molecules will actually make it to the trap region. We tested this by looking for LIF from the free-flight molecular beam in the center of the magnet, where the trap center would be if the magnet were turned on.

Figure 3.6 shows data that was used to characterize the molecular beam. The discharge voltage does not cause a glow discharge until there is sufficient gas density

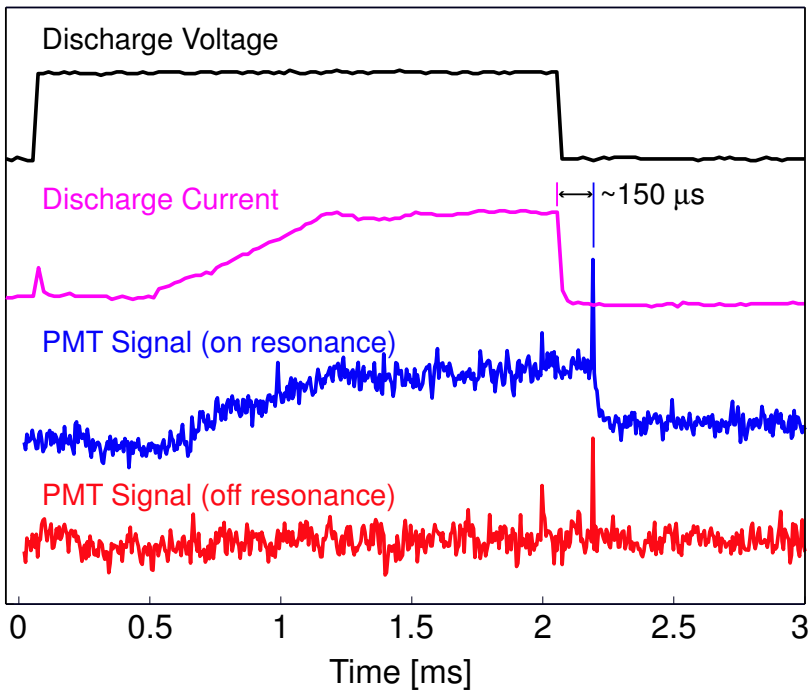

Figure 3.6: Laser-induced fluorescence from the molecular beam of NH in the center of the magnet under free-flight conditions (no buffer gas, no magnet current). The time lag between the discharge current and fluorescence signal correspond to a beam velocity of 1000 m/s. The LIF signal shows that the amount of ground-state NH in the molecular beam is proportional to the discharge current.

in the discharge region to initiate the discharge, so the current and voltage traces do not have the same shape. The voltage is turned off at 2 ms and the delay between that and the loss of fluorescence signal corresponds to at 1000 m/s beam velocity. It is not clear that there should be any NH in the beam in the electronic, rotational, and vibrational ground state, but our detection of this state indicates its production in the discharge. The population in this state may be enhanced by the supersonic expansion of gas exiting from the valve orifice.

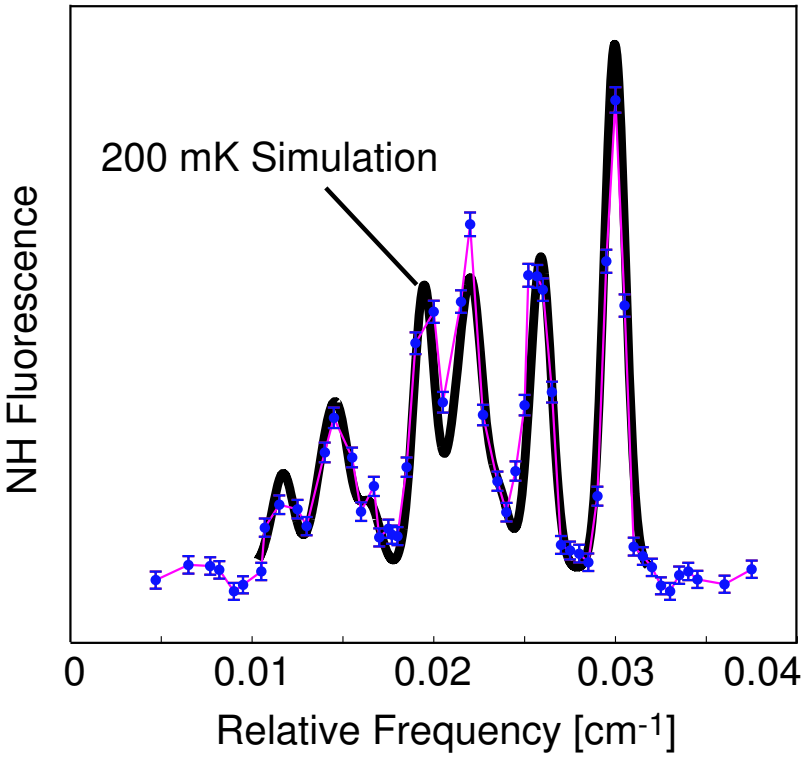

Figure 3.7: The hyperfine structure of NH $A^3\Pi_2(v = 0, J = 2) \leftarrow X^3\Sigma^-(v = 0, J'' = 1)$. The black trace is a simulated 200 mK spectrum with line positions from literature and line strengths from Eq. B.76.

3.3.2 Free-Flight Spectroscopy

The free-flight beam makes its way through a series of apertures before getting to the detection region. First, there is a hole in the 77 K shield, then the 4 K shield, and then the cell aperture. These holes effectively act as skimmers of the molecules that are hottest transversely, which means the molecules in the detection region should be fairly cold in the transverse direction. Since our fluorescence excitation laser intersects the molecular beam transversely, geometric calculations predict that the Doppler broadening of our signal should be smaller than the hyperfine splitting.

Figure 3.7 shows the hyperfine spectrum of NH on the $A^3\Pi_2 \leftarrow X^3\Sigma$ transition

between rotational and vibrational ground states. The simulated spectrum line positions are taken from [186]. To get the line strengths, hyperfine constants from [186, 194] were used to determine the makeup of the hyperfine states of the ground and excited parts of the transition. As a check, these calculations yielded hyperfine shifts that agree with Ubachs [186] to better than 10%. The resulting state mixtures and intensity calculations are given in Appendix B.

3.3.3 Zeeman Spectroscopy of NH

As Figure 3.7 shows, the frequency spread of the hyperfine lines is about 0.02 cm^{-1} wide. The Doppler width at 4.2 K will be given [52] by

$$\Delta\nu_{\mathrm{D}} = \frac{2\nu_o}{c}\sqrt{\frac{2\ln 2 k_{\mathrm{B}} T}{m}} \approx 0.01 \text{ cm}^{-1}, \tag{3.2}$$

which is comparable to this natural broadening. The cold buffer gas will therefore produce a spectrum that is broad enough to make resolution of individual hyperfine lines difficult but narrow enough to see some structure from the hyperfine interaction.

Figure 3.8 (upper) shows the buffer-gas cooled spectrum of NH in the center of the magnet with no current flowing through the magnet. Indeed, the spectrum shows some features that deviate from a single Gaussian or Voigt profile due to the hyperfine structure of NH. Because of this coincidence of frequency widths, the sensitivity of fitting a simulated spectrum to the measured spectrum is too low to determine a temperature to better than a few Kelvin.

The lower trace of Fig. 3.8 shows the triplet splitting when a uniform (Helmholtz) magnetic field is applied. Here the $J = 1$ triplet is split into $M_J = 0, \pm 1$ states corresponding to the three possible projections of the total electron spin on the magnetic

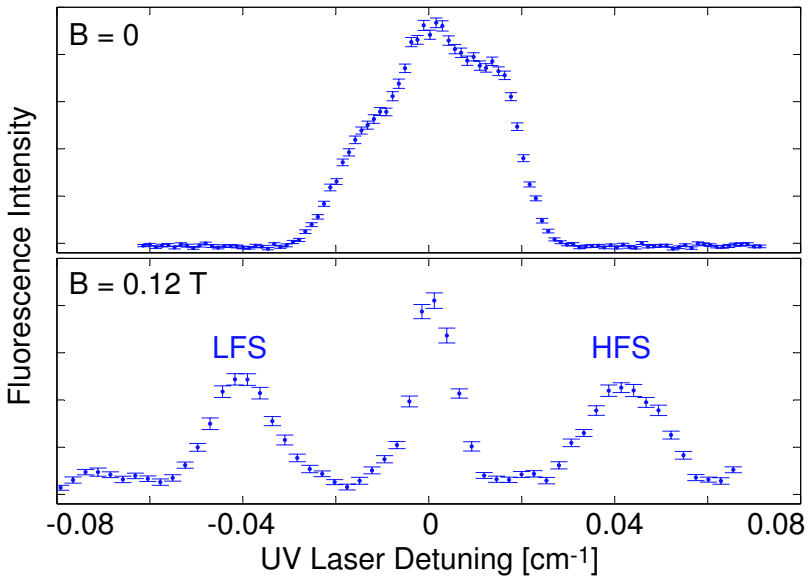

Figure 3.8: The $\Delta M_J = 0$ transitions on $A \leftarrow X$ of buffer-gas cooled NH in (upper) zero field and (lower) 0.12 Tesla uniform Helmholtz field. The zero-field spectrum is a mixture of Doppler broadening and hyperfine structure, which are roughly the same widths at 4.2 K. The 0.12 Tesla spectrum shows the $J = 1$ ground state triplet splitting into low-field seeking (LFS), high-field seeking (HFS) and unshifted Zeeman sublevels.

field axis. The $M_J = +1$ LFS state is the state we trap and the $\Delta M_J = 0$ transition experiences a negative line shift. Likewise, the HFS state experiences a positive shift with field for the $\Delta M_J = 0$ transition. By following these peaks as a function of field, we are able to map out the Zeeman effect in the ground and excited states of NH, as shown in figure 3.9.

The solid colored lines are based on the calculation in Appendix B and show deviations from Eq. 3.1 (black lines). The ground state energies are in fact very well described by Eq. 3.1, but the excited state deviates from linearity due to mixing in of the $\Omega = 1$ state.

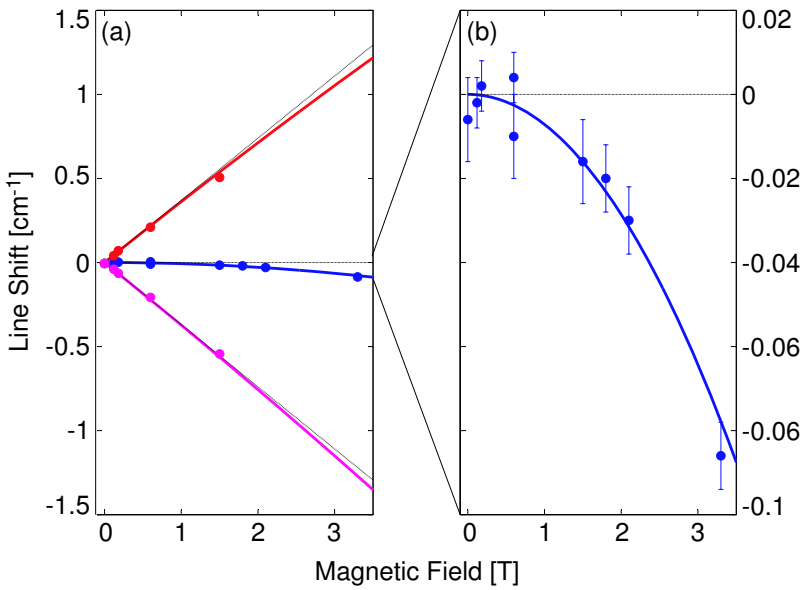

Figure 3.9: The $\Delta M_J = 0$ transition center frequencies of buffer-gas cooled NH as a function of magnetic field. (a) shows the HFS (red), "field-insensitive" (blue) and LFS (magenta) Zeeman shifts as measured (solid points). The black lines are what would be expected from Eq. 3.1 and the solid colored lines are from the calculation in Appendix B. (b) shows a close up of the "field-insensitive" state shift, which deviates from zero due to magnetic-field mixing of the $^3\Pi_2$ and $^3\Pi_1$ states.

3.3.4 Magnetic Field Enhancement of the Diffusion Lifetime

In order to measure the lifetime of NH in the buffer-gas cell, the laser was kept at a single frequency and the signal decay was monitored as a function of time. In order to see the effect of the magnetic trapping field on the lifetime, we operated the magnet in the anti-Helmholtz trapping configuration. By doing this for multiple frequencies, the spectrum evolution of cold NH in the trapping field was obtained. From these data we were able to see the HFS molecules leave the trap while the lifetime of the LFS molecules was enhanced. The diffusion lifetime in the cell with zero magnetic field was measured to be 4.0 ms, and the LFS molecule lifetime was enhanced by the trap field to 8.9 ms at our maximum of $\eta = 3$, as expected.

This result not only demonstrated the principle of buffer-gas loading a trap from a molecular beam, but also indicated that the Zeeman relaxation cross section was not anomalously high. Furthermore, the technological challenge of making a 2 K cryogenic apparatus compatible with a room-temperature molecular beam source was overcome successfully.

Chapter 4

Phase II Apparatus

The lifetime enhancement due to the magnetic field from Phase I was only a factor of two, as expected from the numerical calculation in Jonathan Weinstein's thesis [198]. To use the word "trapping," however, it must be demonstrated that the molecules are confined long enough to form a trapped thermal distribution. Since the magnet was running at the full design current for Phase I, the only way to increase η is to further lower the buffer-gas temperature. This was accomplished by constructing and installing a ^{3}He refrigerator. Since the magnet is still limited to the temperature of the helium bath, a buffer-gas cell that is thermally connected to the refrigerator and thermally disconnected from the magnet was introduced.

The Liquid helium boiloff due to heat loads on the apparatus was reduced through the introduction of a mechanical cryocooler called a pulse tube cooler (PTC). The PTC is able to extract heat at 40 K and 4 K using electricity, which enables us to dramatically reduce our liquid helium costs. Furthermore, we switched from vapor-cooled current leads to magnet leads made from high critical current (high T_c) su-

perconductor. These new current leads also dramatically reduced our liquid helium consumption compared to the copper vapor-cooled leads.

4.1 Pulse Tube Cooler

From an integration perspective, the pulse tube cooler is simply a device that has two stages with well-defined cooling power curves. The first stage has a base temperature around 35 K and the second stage can reach 3.5 K or so. The PTC takes electricity and uses it to extract heat from these low temperature stages (called heat exchangers) and dumps it into room-temperature reservoirs.

We chose to buy a pulse tube cooler instead of a Gifford-McMahon (G-M) cryocooler because the lack of moving parts at cold temperatures likely tends to increase device longevity and reduce vibrations.

! During each thermoacoustic cooling cycle ($\approx$ 1 Hz) the temperatures of the PTC heat exchangers tend to fluctuate considerably ($\leq$ 1 K amplitude). This has not been a problem for our experiment due to our loose temperature constraints for things connected to the PTC and the damping effect of the large amounts of copper attached to the PTC, but future experiments should keep this fluctuation in mind.

4.1.1 How Pulse Tube Coolers Work

The modern orifice pulse tube cooler uses aspects of both thermoacoustic cooling in the pulse tube and Stirling-cycle heat pumping on the regenerator [181]. In this section I will focus on the most simplistic model of thermoacoustic cooling I can in order to touch upon the basis of operation of a full orifice pulse tube cooler. A simplified diagram of a standard pulse-tube cooler is shown in Fig. 4.1. The pulse-tube

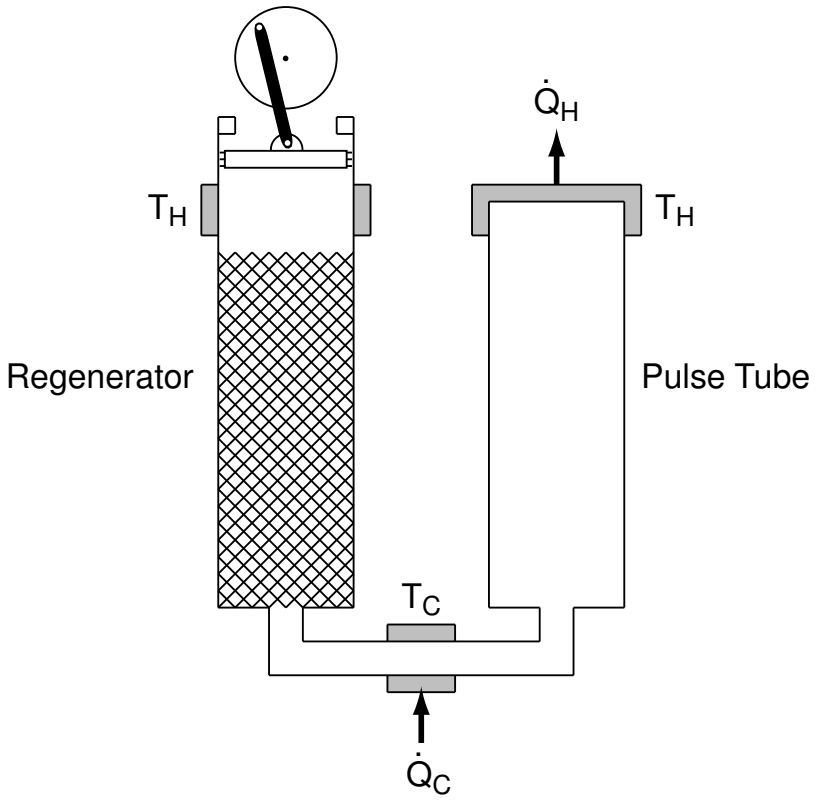

Figure 4.1: A simplified pulse-tube cooler.

cooler is filled with high-pressure helium and is surrounded by vacuum. A standing acoustic wave is set up in the pulse tube by a periodic pressure modulation at room temperature, shown here as a room-temperature piston. The regenerator tube houses the regenerator, which is a material of high surface area, thermal conductivity, and heat capacity, such as a stack of copper meshes or packed metal spheres. The regenerator's purpose in this simplified PTC is merely to thermally insulate the cold end from the warm gas at room temperature while transmitting the pressure wave. This regenerator could also be replaced by a displacer made of low thermal conductivity material that can move up and down to transmit the pressure wave.

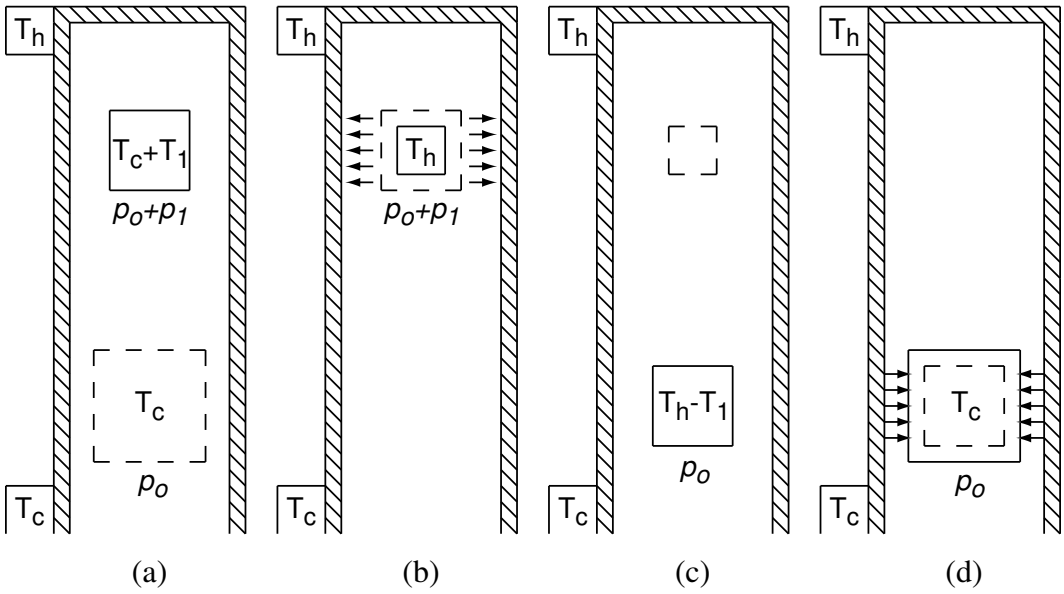

Figure 4.2: The pulse tube thermoacoustic cooling cycle. The pulse tube walls have low thermal conductivity along their length to support a thermal gradient. Gas packets are moved up and down the pulse tube to deposit their heat on the walls at the top and remove heat from the walls at the bottom.

The cold end heat exchanger is at the bottom of the pulse tube and this is where experimental parts are attached to utilize the PTC's cooling power. The pulse tube itself is no more than a thin-walled stainless tube with a closed end up at high temperature. The walls of the pulse tube have low thermal conductivity along their length and therefore support a large thermal gradient. The pressure wave set up by the piston pumps heat from the cold end of the pulse tube to the warm end using thermoacoustics.

A thermoacoustic cooling cycle is shown in Fig. 4.2. A packet of gas is used to pump heat up the walls of a the pulse tube and then returns to its original state. In part (a), the gas packet is moved from the cold end of the pulse tube to the closed, hot end due to an acoustic standing wave produced by a room-temperature energy

source. The compressed packet of gas is heated by the compression and is no longer in thermal equilibrium with the walls.

If this heated packet of gas is hotter than the pulse tube walls at its new location, it will deposit heat into the walls, which act as a reservoir at T_h (the opposite case, where $T_c + T_1 < T_h$ will be discussed in the box below). This cooling causes the gas packet to contract further, as shown in part (b).

In part (c), the second half of the acoustic wave cycle moves the gas packet back to the bottom of the pulse tube and expands it. The packet is now at a temperature $T_h - T_1$, which is colder than the walls. Part (d) shows the gas packet accepting heat from the walls at T_c, which will then be deposited at T_h a half-cycle later.

! If the thermal gradient on the pulse tube is high enough that $T_h - T_c > T_1$, the gas packet will be cooler than the walls in step (b) and will expand instead of contracting. This will then push the gas in the top closed end of the tube back downward, where it will be cooled by the cold end. This would be called a thermoacoustic prime mover instead of a pulse-tube cooler and would actually generate energy from the reservoirs. This is how Taconis oscillations and the familiar liquid helium level sensor called a "thumper" work.

A modern commercial PTC is actually called an *orifice* pulse tube cooler and has a few more elements to improve its cooling power, but the principle is the same as that described here. A detailed analysis is available from Swift [181].

Our pulse tube cooler is a cryomech PT-410 and was installed to cool two elements of the apparatus. The cooling power curves are shown in Fig. 4.3. The second stage (the coldest) is thermally connected to the 4 K radiation shield. The shield is mechanically connected to the helium bath by a set of G10 standoffs, and the second stage of the PTC is connected to it by a series of copper braids. The braids ensure that the differential thermal contractions during cooldown do not apply too much

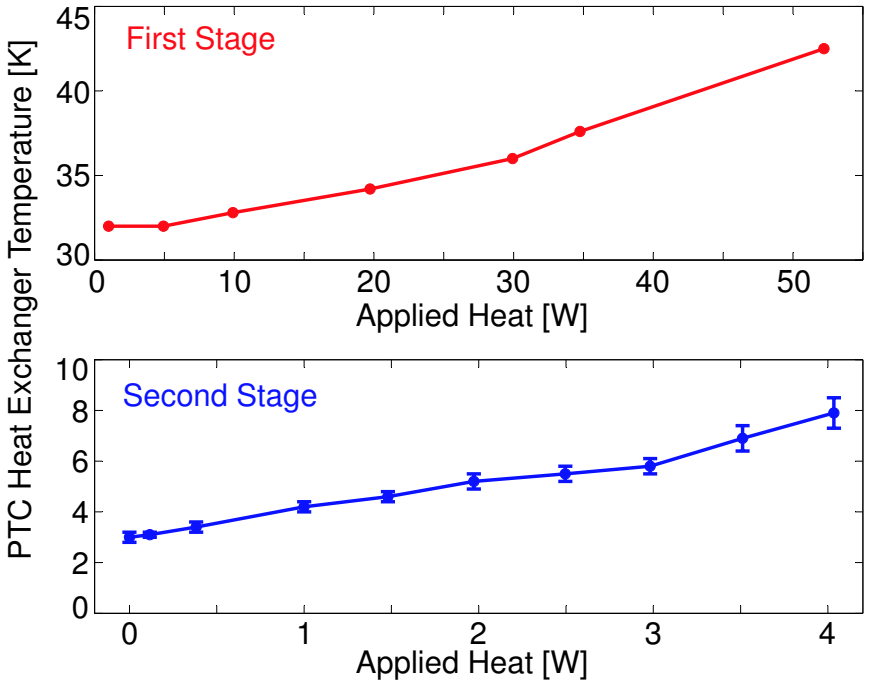

Figure 4.3: Power curves for the two stages of our pulse tube cooler. The base temperatures are 3 K and 32 K for the second and first stages, respectively. Application of more than 50 W heat to the first stage caused the second stage temperature to rise by about 0.3 K.

force or torque to the delicate PTC heat exchanger and also decouple the shield from the PTC cycle mechanical vibrations. The first stage of the PTC is used to cool the top of our high T_c superconducting leads using a flexible heat link made from thin copper strips.

! The heat link between the first stage of the PTC and the top of the high T_c leads is made from a stack of copper sheets bent at a right angle to be flexible in two dimensions. The foil sheets are sold as "101 Annealed Copper" by All Foils, Inc. and are 5 mils in thickness. We used a stack of 1500 1 in. wide strips that were held at the ends by clamps. We estimate from the PTC temperature that the thermal conductivity of this link is 175 W/m·K, which is about a factor of 2 worse than *room temperature* copper. We attribute this low thermal conductivity to the repeated boundary resistance conducting heat between layers. We could not find a way to heat link to the end face of the stack since heating the stack causes the layers to "glue together," presumably due to a layer of junk on each strip. In the future, copper braids should be used instead.

4.1.2 High-T_c Superconductor Magnet Leads

One major difficulty of superconducting magnets involves the details of how to get current to the magnet. This necessarily involves non-superconducting parts, which experience ohmic heating and will contribute to the heat load on cryogenic components. High quality copper and large cross-sectional area can be used to reduce this heating, but this will increase the conductive heat load down the leads, which adds to the heat load problem instead of solving it.

The two most common solutions to this problem are vapor-cooled leads and high T_c superconductor leads. Vapor-cooled leads are copper leads with an array of holes running through them along their length. The idea is to use the cold vapor produced by liquid helium boiloff to extract heat from the leads. The leads are inserted into the bath space through electrically-insulating compression fittings on the top plate and the bottom of the leads must remain above the liquid level. Low T_c superconductor can be attached to the bottom of the leads and thermally anchored to the liquid in the bath to form a superconducting path from that point onward. The bath space is then sealed at the top plate, so all of the boiloff vapor must flow through the leads to exit the bath. In this way, the enthalpy of the boiloff vapor is put to work to reduce heat loads on the bath instead of being thrown away in a standard exhaust system.

Our set of four vapor-cooled leads were rated for 250 A. Using the recommended value of 3.2×10^{-3} l/hr per Ampere for a pair gives us 0.9 l/hr for our four leads operating at the design current of 143 A and 0.5 l/hr at zero current.

The vapor cooled leads worked to allow us to run our magnet, but there are some problems associated with them. They have a tendency to become clogged with ice

both during cooldown and while in operation, so tremendous care must be taken to keep pure helium flowing through them during all stages of the experiment. Even then they sometimes clog, and certain leads generally have less flow than others, even at room temperature. Furthermore, pumping on the helium bath is not straightforward if dense, cold, helium gas must flow through the leads at all times. Lastly, a heat load of 1 W going into the helium bath is considerable and expensive.

Liquid nitrogen is far less expensive than liquid helium. In terms of latent heat at their respective atmospheric pressure boiling points, liquid nitrogen runs us 0.4 cents per W·hr while liquid helium costs about $10.50 per W·hr. Even if we add the enthalpy change for helium vapor in getting from 4 to 77 K, helium is still more than $1 per W·hr. One way to get the magnet current from 77 K to 4.2 K without dumping a large heat load into the 4.2 K side is to use a material that superconducts at 77 K, the so-called "high T_c" superconductors.

For this purpose, we purchased 250 Amp high T_c leads from HTS-110. These leads are rated for a conductive heat load of less than 100 mW per pair from 64 K to 4.2 K. Since HTS-110 is a spinoff from American Superconductor, it is likely that they use "HTS Cryoblock" wire from American Superconductor, which is a Bi-based superconductor in a silver-gold alloy matrix.

The current from room temperature can be brought to the top of the leads using copper conductors, where their heat load is absorbed by a cryocooler or relatively inexpensive liquid nitrogen. By using the first stage of a PTC to cool the top of the leads and the second stage to cool the bottom, it is now possible to make cryogen-free superconducting magnet systems. We use a combination of liquid nitrogen and the

PTC to cool the top of our leads. The copper sections connecting the tops of the high T_c leads to the room-temperature feed through is made from ∅ 0.25 in. C101 copper rod. These sections are heat-sunk to the 77 K shield about halfway to the high T_c leads, and the top of the high T_c leads are connected to the PTC first stage through the copper strip heat link. The room-temperature feed through gets frosty if left alone (especially of the magnet power supply is not connected) and we run a computer-case fan on it at all times to keep it at room temperature.

With the PTC and our high T_c current leads, our helium bath hold time is about 50 hours, corresponding to a heat load of less than 600 mW.

The room-temperature resistance of the high T_c leads was measured to be about 3.9 mΩ per lead. A four-wire measurement of the resistances while cold resulted in 1.8 $\mu\Omega$ for s/n L2819 and 1.2 $\mu\Omega$ for s/n L2818, likely dominated by the ohmic connections at the ends. The copper sections of lead in the vacuum chamber were measured to have resistances of 114 $\mu\Omega$ per lead at 128 Amps. Despite the fact that the rated 250 Amps is quoted for 60 K, our leads remained superconducting at 82 K with 170 A of current.

4.2 ^{3}He Fridge

In order to reach temperatures low enough for trapping NH (of order 500 mK), our ^{4}He cryostat needed to be augmented with either a ^{3}He fridge or a ^{3}He-^{4}He dilution refrigerator. The use of a commercial ^{3}He fridge has been demonstrated for trapping $2\mu_B$ species [79] in our lab, and the additional complexity and cost gained in going from a ^{3}He fridge to a dilution refrigerator was deemed unnecessary for our

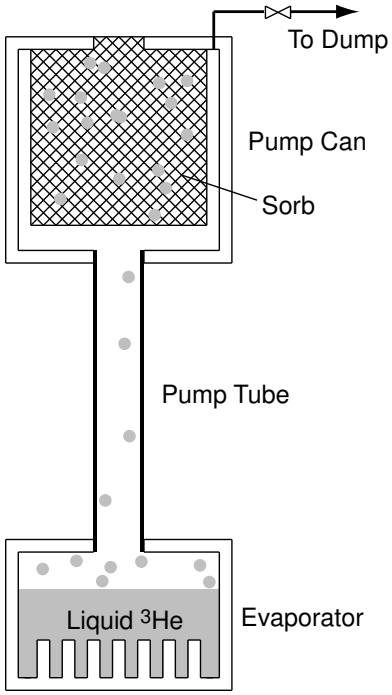

Figure 4.4: ^{3}He fridge schematic. The liquid in the evaporator is pumped by a cold charcoal sorb in the pump can.

application.

4.2.1 Design

Our ^{3}He fridge design constraints were somewhat unusual compared to typical (condensed matter physics) applications, which led us to design and build our own fridge ourselves. A schematic of the fridge is shown in Fig. 4.4. The evaporator holds the liquid ^{3}He and must be made of high thermal conductivity materials to efficiently exchange heat with the liquid. There should be a large contact area between the liquid and the evaporator body to overcome the Kapitza boundary resistance, which is shown as fins inside the evaporator. The pump tube should be made of low thermal conductivity material in order to minimize the conductive heat load down the tube

from the 4 K pump can to the 400 mK evaporator. The pump can holds the charcoal sorb and must provide an external thermal connection (shown at the top) to the sorb to keep it cold during operation.

In order to design the dimensions of the fridge parts, an estimation of the heat loads was undertaken. At a buffer gas flow rate of 50 sccm (a reasonable upper limit), the change in enthalpy from 4.2 K to 400 mK is 1.2 mW, so 1 mW was used as the design heat load in steady-state. This corresponds to 6.3 liquid cc per hour. If we want to run for a minimum of 10 hours at a time before regenerating the fridge, this means a fridge capable of providing 100 cc of 400 mK liquid ^{3}He.

In order to cool the liquid ^{3}He down to 400 mK, evaporation of some of the liquid will be used. Figure 4.5 shows the calculated fraction of the initial liquid amount that is left over in cooling to a given final temperature. For a starting temperature at the λ-point of ^{4}He, the cooldown wastes about 20% of the liquid. Things are about a factor of two worse if we start at the ^{3}He critical point. The ^{3}He specific heat was taken from Greywall [73] and the latent heat of vaporization used was a polynomial fit[1] to the data in Kerr [110] and Roberts and Sydoriak [158]. These considerations leave us with a total volume of about 150 cc of liquid ^{3}He at the start of the cooldown, which sets the volumes of the evaporator, and sorb to about 200 and 500 ml, respectively. 150 ml of liquid corresponds to about 100 stp l of gas, which sets the volume of the dump.

[1] $L = 11.7 + 49.4T - 34.2T^2 + 13.9T^3 - 2.4T^4$, L in J/mol and T in K

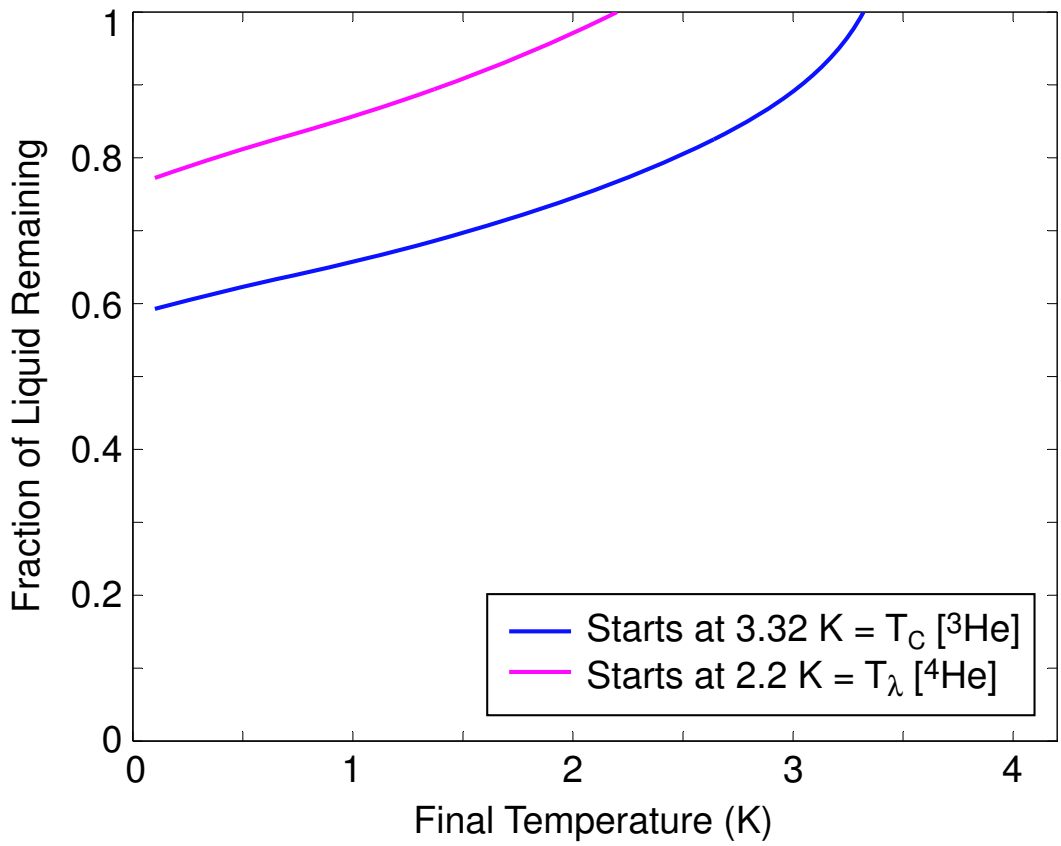

Figure 4.5: The amount of liquid ^{3}He that remains when the liquid is pumped to reach a given base temperature. The ^{4}He λ-point is a reasonable lower limit for the starting temperature cooled by a 1 K pot, while the ^{3}He critical point is the highest temperature at which there is a phase transition in ^{3}He.

1 K pot

The critical temperature for ^{3}He is 3.32 K [147], which means that during regeneration, the evaporator must be at least this cold to sustain a phase transition. To obtain this phase transition, we soft-soldered a copper sleeve onto the pump tube. For our test run of the fridge, this *condensation point sleeve* was cooled by a copper heat link to the ^{4}He bath, which was pumped down to 2.2 K by a room-temperature pump. We later found that the heat load on this sleeve due to the heating of the sorb

during regeneration was too great to achieve low temperatures for condensation. We therefore put another condensation point sleeve slightly lower on the pump tube and used the first sleeve to absorb the heat load from the sorb and the second to liquefy the ^{3}He.

In the trapping apparatus, we did not want to pump on the whole bath to condense the ^{3}He, which would restrict our access to the bath space during fridge operation. Instead, we made a 1 K pot that continuously sips helium from the bath space and then a pumping line to room temperature cools the liquid below the ^{3}He critical point.

In order to continuously sip helium from the atmospheric pressure bath and still maintain a low pressure in the 1 K pot, an impedance must be introduced into the sipping line. The impedance required is quite high and the total length of the sipper line is limited, so the impedance was constructed by putting a tight-fitting copper wire into a small stainless tube. The conductance of this system was measured at room temperature by applying a known pressure of helium to one side and filling an inverted water-filled graduated cylinder with the gas exiting from the other side. Using a stopwatch we were able to obtain the flow rate, and thereby the conductance. By assuming that the impedance is linearly proportional to the length of the copper wire, we were able to create a known impedance for use in the 1 K pot. Our 1 K pot cooling power was measured to be 1.3 mK/mW.

Heat Switch

During operation, the sorb must be kept below about 8 K to pump helium effectively. Since the heat of adsorption for ^{3}He on charcoal is about 50 times greater

than its latent heat of vaporization [57], the heat link from the sorb to the 4.2 K bath must be capable of supporting a 50 mW heat load. This suggests a tendency toward a heat link of high thermal conductivity. However, during the condensation phase, a heater must hold the sorb at 40 K, which would put a tremendous heat load on the bath, which suggests limiting the thermal conductivity of the heat link between the sorb and the bath.

! The original heat link between the sorb and 4 K was made of Sn since tin has a lower thermal conductivity at 40 K than at 4K. While this passive heat switch worked nicely for about four cooldowns, upon opening the chamber after a particularly slow warm-up we found that the heat like was missing and the 4 K shield was covered with powder. What had happened was an allotropic phase transition. Above 286 K, the ground-state configuration of bulk Sn is a metallic tetragonal crystal called β Sn [155]. Below 286 K the ground state is a diamond cubic structure called α Sn (or *grey tin*) that is essentially a powder. The slow warm up had allowed the tin to spend enough time just below the $\beta \rightarrow \alpha$ phase transition to drive the conversion, presumably seeded by a tiny amount of α Sn already present.

After having the tin thermal link fail (see box), we chose to use helium vapor taken from the bath. By impeding the exhaust from the bath with a tunable relief valve, we are able to create a flow of vapor from a sipper line to the fridge sorb and then out of the chamber into the exhaust. By closing off this cooling line at room temperature, the sorb can be effectively thermally disconnected from the bath. Once the ^{3}He has condensed in the evaporator, the vapor cooling can be restarted and the sorb will begin to pump on the liquid.

4.2.2 Performance

Before filling the fridge with ^{3}He, we did a test run with ^{4}He. The evaporator temperature was monitored with a resistor and achieved a base temperature of 770

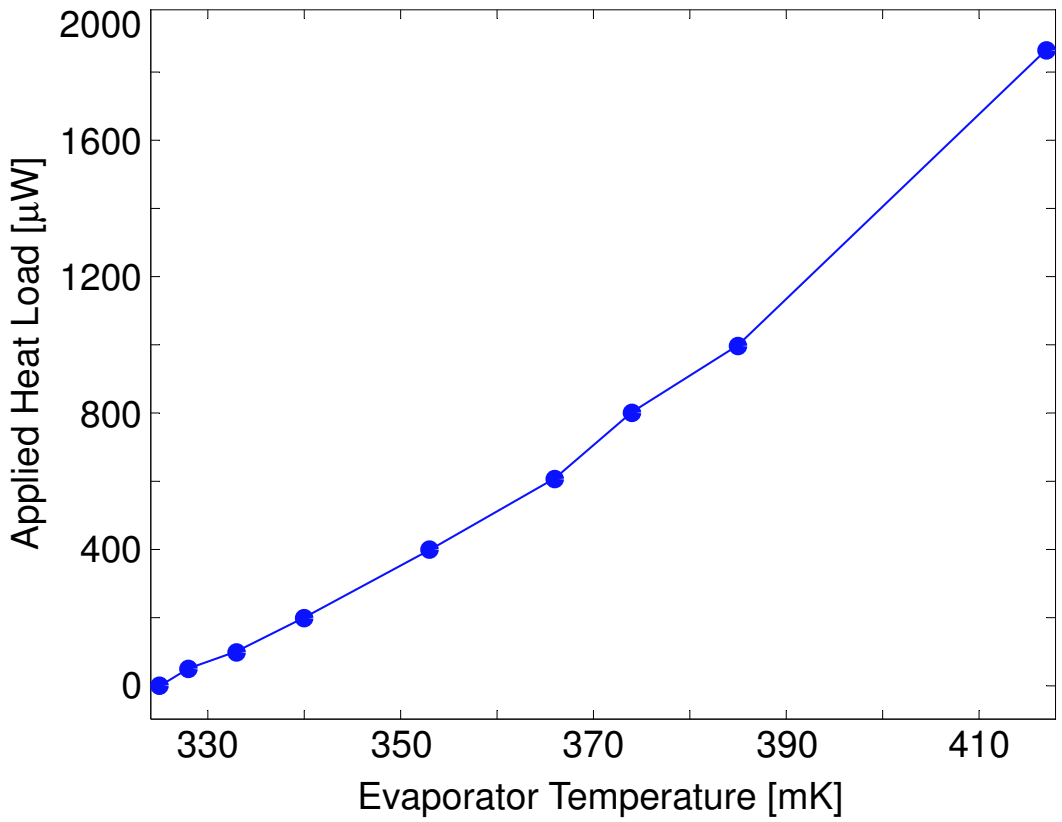

Figure 4.6: ^{3}He refrigerator evaporator temperature as a function of applied heat load.

mK. In order to condense ^{3}He, the condensation point sleeve temperature was reduced by pumping on the bucket dewar bath to which the sleeve was connected. The power curve for the fridge is shown in Fig. 4.6.

4.3 Buffer Gas Cell

The buffer gas cell is essentially a cold surface surrounding the buffer gas. The cell itself must be thermally conductive enough to maintain a cold temperature for thermalizing the helium. Our lab has constructed various types of cells, but the

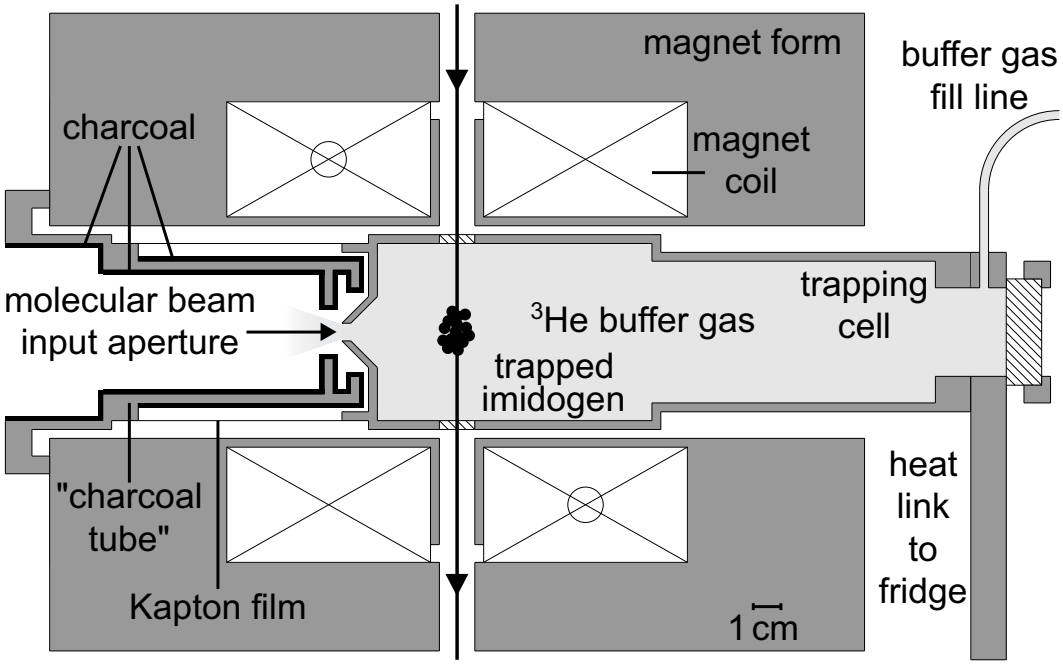

Figure 4.7: Schematic of the magnet and buffer-gas cell. The molecular beam enters the cell entrance aperture from the left. The LIF excitation laser crosses the center of the trap to generate fluorescence. The cell is held mechanically by G10 and Kevlar lassos and Vespel SP-22 "dog collar" cones.

experimental cell in this work was made from annealed copper C10100. The cell has windows to allow the laser through in the midplane of the magnet, as well as a molecular beam input aperture for the radicals to enter, as shown in Fig. 4.7. The cell is thermally connected to the ^{3}He fridge by a flexible copper heat link and is suspended in the magnet bore with a combination of G10/Kevlar lassos and Vespel 22 "dog collar" cones.

4.3.1 Cell body

The trap depth in our spherical quadrupole field is set by the inner diameter of the cell at the midplane of the magnet. The field near the cell wall increases linearly

in the radial direction, and therefore so does the trap depth. To obtain the maximum trap depth, the walls of the cell must be as thin as possible here, and as close as possible to the magnet bore. At the midplane of the magnet, the cell wall is 1 mm thick with a 7.12 cm inner diameter, which gives a little more than 2 mm clearance on the radius between the cell and the magnet.

The molecular beam input aperture is at the end of a 90° conical protrusion to reduce the effect of beam products bouncing back off the copper and degrading the vacuum in that region. The hole is 3 mm in diameter. The back of the cell has an indium sealing surface to which the heat sink foot can be attached.

The cell windows are attached by a two step process that will be described in detail in Edem Tsikata's thesis. Essentially, windows are epoxied to copper foil that is then soft-soldered to the cell, thus making a leak-tight seal without stressing the windows mechanically during cooldown.

All copper parts were fully annealed in forming gas prior to being brazed together.

4.3.2 Heat Link

Since the cell is delicately suspended in the magnet bore and must be thermally detached from the 4.2 K magnet, torques and forces from the heat link to the fridge had to be minimized. We accomplished this by constructing a flexible heat link made from copper rope. The rope for the phase I apparatus was probably C102. The phase II apparatus rope was made from copper alloy C10100 in a custom run by Cooner Wire, Inc and is the only such certified copper 101 rope of which we are aware. The product we purchased is called rope lay with construction 7x7x108/36, which means

it is made from 36-gauge filaments in groups of 108 in groups of 7 in groups of 7. If we denote the second-largest unit (7x108/36) as a "strand," two strands fit snugly in a 0.25 in diameter hole. These strands were used to make the heat link by welding the ends to lugs and then bolting the lugs on the heat sink foot and the evaporator of the fridge.

It is possible to braze copper rope for making thermal and mechanical connections to copper pieces. The drawback of using this process is the fact that the solder will try to wick up the braid, which can compromise its mechanical flexibility. This can be overcome to some extent through maintenance of heat during the brazing or the application of an oxidizing agent (*e.g.* white-out or milk of magnesia) to the part of the braid you want to keep solder-free. However, the welding process described here (see Fig. 4.8) worked nicely, and probably made th best thermal connection possible.

The lugs were copper blocks with a 0.257 in through hole for the rope and then other holes and tabs for bolting to things. The braid was inserted in the hole in double thickness by wrapping steel wire around a strand, twisting the wire to affix it to the strand, and the folding the strand over at that point, as shown in Fig. 4.8(a). The rope was then pulled through the 0.257 in hole by grabbing the twisted wire with pliers and pulling it through the hole (see b). The appropriate amount to leave hanging out the other side is about 1 hole diameter, at which point the steel wire can be cut off.

The TIG welding seemed to work well in DC reverse (DC-) mode with about 80A max current. A sharp tip worked, but it would sometimes round off a bit in the process. The shield gas used was 75% He and 25% Ar, which is what we use for

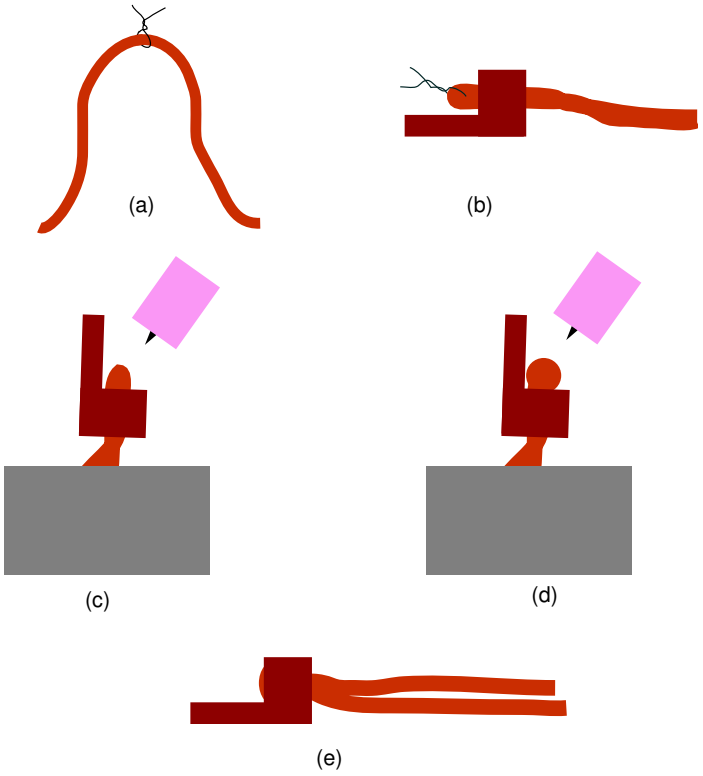

Figure 4.8: The process of welding copper rope to a copper lug.

aluminum. The braid was held in a vice so that the weld surface (the 1 hole diameter worth of braid sticking out of the hole) was facing up (important for gravity, see Fig. 4.8(c)). An arc was started directly to the braid, which rapidly turns it into a molten sphere of copper (d). The copper blob doesn't wick up the braid since the braid is too cold, and it does not wet the lug yet for the same reason. By continuing to put heat into this ball of molten copper, the lug would eventually heat up and the copper very suddenly fuse to the melting surface. At this point it was important to back off on the current pedal rapidly to keep the whole lug from turning into a puddle. Through a little practice the whole end of the braid can be welded evenly to the face of the lug without deforming the other parts of the lug (e).

This phase I apparatus heat link was measured to have a thermal conductivity of 28 mK/mW at ^{3}He fridge temperatures. This was made from 14 "strands" of the C102 rope that were approximately 10 cm long, giving a linear thermal conductance of 3.9 K·cm/mW for a "strand."

It is possible that annealing the braid will improve its thermal conductivity, but it is unclear how the gentle handling typical of installation will affect its thermal conductivity. Furthermore, torch annealing in air does not work since the large surface area quickly oxidizes and strands become glued together by oxide, and individual strands easily become too hot and melt under the torch flame. Furnace annealing in forming gas is also bad since the clean surfaces cold weld together and the annealed rope becomes rather rigid. Vacuum furnace annealing is therefore the most likely method of annealing to succeed.

4.3.3 Charcoal and Kapton Tubes

The most difficult technical challenge of the experiment is finding a way to keep the helium that exits the molecular beam entrance aperture from causing problems. First, the helium can scatter molecules out of the molecular beam before they get to the trapping region. If we assume that one scattering event results in molecule loss, the probability P of a molecule traveling a distance l to propagate without collisions will be given by Beer's law:

$$P = e^{-n_{\mathrm{He}}\sigma_d l} \tag{4.1}$$

where n_{He} is the helium density and σ_d is the cross section. If we restrict ourselves to the region outside the cell but inside the magnet bore (l = 10 cm) and assume $\sigma_d = 10^{-14}$ cm^2 we get a $1/e$ attenuation length of 10 cm for $n_{\mathrm{He}} = 10^{13}$ cm^{-3}. We expect the density in the cell to be of order 10^{15} cm^{-3}, and the area of the end of the magnet bore is $A_{\mathrm{bore}} = 45.6$ cm^2. The helium density in this region will be equal

to the density in the cell times the ratio of the area of the molecular beam input aperture to A_{bore} if there is no additional pumping. This would be borderline for a 3 mm diameter cell orifice and insufficient for 1 cm.

The second problem posed by the helium gas outside the cell but inside the magnet bore is that it can thermally connect the cell to the magnet bore, resulting in a heat load on the cell. To estimate this heat load, the annular region between the cell and the magnet has an area of about $A_{\text{overlap}} = 450$ cm^2. Assuming an accommodation coefficient of 1, the heat load will be [147] 1 mW for a density of 7×10^{11} cm^{-3}. This region is therefore extremely sensitive to helium gas and a high vacuum must be maintained while the fridge is running.

To solve these problems we introduced two parts to the region inside the magnet bore: the *charcoal tube* and the *Kapton tube*. The charcoal tube is shown in Fig. 4.7 and consists of a copper cylinder coated with charcoal. This charcoal acts as a pump in the magnet bore to reduce the helium density. The charcoal tube is fitted with heaters and a tuned thermal connection to the magnet to enable the regeneration of the surface without warming up the entire magnet.

The Kapton tube (also shown in Fig. 4.7) connects the cell to the charcoal tube to keep helium out of the annular region between the cell and the magnet bore. Kapton was chosen for its low thermal conductivity. The tube was constructed from 2 mil Kapton film that is glued into a tube shape with Loctite Superbonder 495. The Kapton tube is then glued to the end of the cell, and slides snugly around the end of the charcoal tube during assembly. Upon cooling down, the Kapton shrinks and makes a sort of seal around the charcoal tube.

We estimate that the charcoal tube can be used without regeneration for 15 hours at 1 sccm, which corresponds to 1.0 cc of liquid helium, in accordance with what would be expected for the amount of charcoal on the tube.

Chapter 5

Results

The five main results from the Phase II apparatus (Chapter 4) are presented here. The first is the demonstration of magnetic trapping of NH, followed by a calibration of the NH density in the trap using absorption spectroscopy. The other three results come from studying the properties of the trapped molecules. Measurement of the elastic-to-inelastic collision rate ratio γ was performed first, with the promising result that this ratio is favorable for buffer-gas loading. We next investigated the predicted scaling of the inelastic collision rate with rotational constant by trapping and studying all four stable isotopomers of NH with both stable isotopes of He. Last, we trapped vibrationally-excited NH($v = 1$) and measured the spontaneous emission lifetime, which is a vital number for astrophysics.

5.1 Magnetic Trapping of Imidogen

There is not a rigorous definition of trapping accepted by the atomic physics community. One possible definition would be to say that a sample is trapped when its lifetime in the trap region is much longer with the trap than without it. This definition is problematic from the perspective that a simple buffer-gas cell would then constitute at trap, whereas such a trap has no definable trap depth or restoring force. We will nonetheless use this definition of trapping for our magnetic trap with the understanding that there are some problems with this definition.

5.1.1 Buffer-Gas Density Calibration

One of the first steps in getting our buffer-gas loaded magnetic trapping apparatus characterized was to characterize the buffer-gas density. This is important both to understand when the conditions in the cell are appropriate for trapping and for calibrating our measurements of collision cross sections.

Calibration of gas densities at low temperatures is nontrivial. There are no commercially available pressure gauges for operation at the temperature and pressure ranges necessary for buffer-gas loading. Room temperature measurements will be affected by thermal transpiration [163], and can depend on parameters that are difficult to control, such as the surface roughness of the tube connecting the gauge to the cold cell and Taconis oscillations.

At high pressures where the mean-free-path λ is short compared to the radius R of the tube connecting the warm pressure gauge to the cold cell, the *pressures* will be

equal in the two volumes, *i.e.*

$$P_{\rm c} = P_{\rm w} \tag{5.1}$$

$$n_{\rm c} = \frac{P_{\rm w}}{k_{\rm B}T_{\rm c}} \tag{5.2}$$

where the subscripts w and c refer to the warm and cold sides, respectively. Convenient units for Boltzmann's constant here are $k_{\rm B} = 1.036 \times 10^{-19}$ Torr/cm^{-3}K.

At low pressures where $\lambda \gg R$ (the so-called Knudsen regime), the pressures will be related by

$$\frac{P_{\rm c}}{\sqrt{T_{\rm c}}} = \frac{P_{\rm w}}{\sqrt{T_{\rm w}}} \tag{5.3}$$

$$n_{\rm c} = \frac{P_{\rm w}}{k_{\rm B}\sqrt{T_{\rm c}T_{\rm w}}}. \tag{5.4}$$

The difficulty comes in trying to decide where each regime ends and what happens in the intermediate regime. One way around this problem is to use empirical data that someone else has calibrated. The Weber-Schmidt equation [159] is one such description of the relationship between the pressures, but it is analytically difficult to handle. Figure 5.1 shows a numerical solution to the Weber-Schmidt equation for parameters that are typical of buffer-gas loading. The intermediate regime tends to lie right about where buffer-gas loading occurs. I have made a reasonable fit to the numerical solution to give an analytic form for the solution to the Weber-Schmidt equation as follows. The mid-point (on a log-log scale) between the Knudsen and normal regimes of Fig. 5.1 can be written in terms of the Knudsen number at the warm end $K_{\rm w}$:

$$K_{\rm w} \equiv \frac{\lambda_{\rm w}}{2R} \tag{5.5}$$

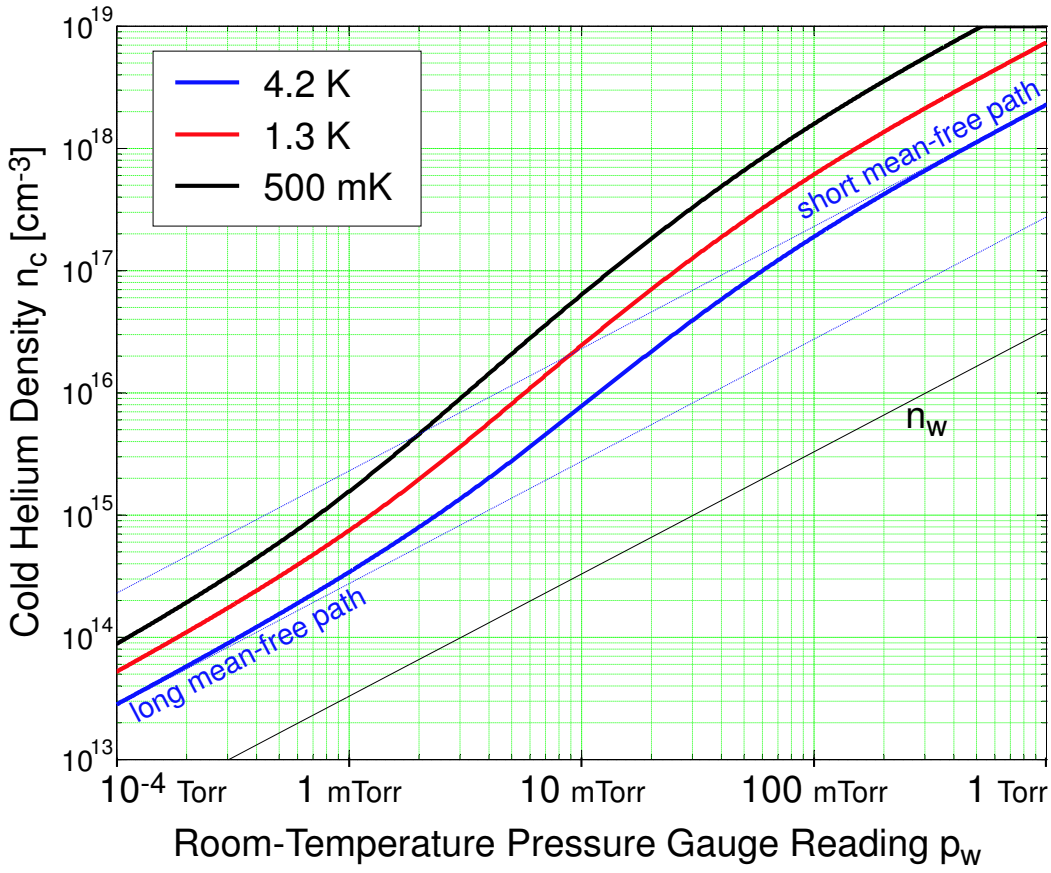

Figure 5.1: Cold helium density as measured by a room-temperature pressure gauge connected by a $R = 2.36$ mm tube, according to the Weber-Schmidt equation. The short mean-free path approximation is given by Eq. 5.2 and the long mean-free path approximation is given by Eq. 5.4

where

$$\lambda_w = \frac{0.01342}{p_w[\text{Torr}]} \left(\frac{T_w}{273.15\ \text{K}} \right)^{1.147} \tag{5.6}$$

is the mean-free path of helium in cm [159]. The pressure reading corresponding to the mid-point will happen at $K_w \approx 3$ for $T_c = 4.2$ K and $K_w \approx 7$ for $T_c = 500$ mK:

$$p_w^{mid}[\text{Torr}] = \frac{0.01342}{R[\text{cm}]K_w} \left(\frac{T_w}{273.15\ \text{K}} \right)^{1.147}. \tag{5.7}$$

The solution to the Weber-Schmidt equation is approximately given by

$$n_{\mathrm{c}} = \frac{p_{\mathrm{w}}}{k_{\mathrm{B}} T_{\mathrm{w}}} \left(\frac{T_{\mathrm{w}}}{T_{\mathrm{c}}}\right)^{\frac{1}{4}\left(3+\mathrm{erf}\left[\frac{\ln\left(p_{\mathrm{w}}/p_{\mathrm{w}}^{mid}\right)}{2.5}\right]\right)} . \tag{5.8}$$

We have not measured pressures in an attempt to verify these equations, but the upper and lower bounds are hard limits given by simple kinetic gas theory and the solution is well-behaved in these limits.

Pumpout Time Calculation

The method outlined above for measuring the cold helium density using a room-temperature gauge will in general not work for all tube materials. If the accommodation coefficient is different for different tube materials, the thermal transpiration effect will give different pressure readings for the same cold helium density. Furthermore, our system involves helium *flow*, which can complicate the measurement at the room-temperature end.

Instead of using a room-temperature pressure gauge to calibrate our density, we chose instead to calibrate the conductance of our flow system. By separately calibrating a helium flow meter we can use our flow rate as a measurement of the helium density in the cell.

The pumpout time of a cell with volume V and an aperture conductance C_a will be given by $\tau = V/C_a$. Our cell has volume $V = 690$ cm^3 and we can estimate the conductance C_a a number of different ways. In the molecular flow regime, if we take the aperture to be an ideal hole of area A in a flat wall we can use $C_{a,\mathrm{molec.}} = \bar{v}A/4$ where $\bar{v} = \sqrt{8k_{\mathrm{B}}T/\pi m}$ is the average helium velocity (6500 cm/s for ^{3}He and 5600 cm/s for ^{4}He at 600 mK).

Table 5.1: Calculated pumpout times for the buffer-gas cell filled with 600 mK ^{3}He for the two aperture diameters (d) used in the experiment.

	$d = 3$ mm	$d = 10$ mm
$C_{a,\text{molec.}}$	6.01 s	0.54 s
$C_{\text{choked,molec.}}$	11.7 s	1.06 s
$C_{\text{choked,visc.}}$	1.19 s	0.11 s

It may also be the case, however, that the flow velocity derived for the conductance above exceeds the speed of sound in helium. In such a case, we have *choked flow*, wherein the actual throughput out of the aperture is limited by the sonic velocity of the helium [123]. The maximum throughput will correspond to $\dot{Q}_{\text{choked}} = C(P_\text{u} - P_\text{d})$ where the ratio of the upstream pressure P_u to the downstream pressure P_d cannot exceed the critical pressure ratio [123]

$$\frac{P_\text{u}}{P_\text{d}} \leq \left(\frac{\gamma+1}{2}\right)^{\gamma/(\gamma-1)} = 2.049 \tag{5.9}$$

where $\gamma = 1.67$ for helium. This results in an effective conductance of $C_{\text{choked,molec.}} = 0.512 C_{a,\text{molec.}}$. For the molecular flow regime, Roth [163] gives the conductance of an aperture in terms of the pressure ratio across it:

$$C_{a,\text{visc.}} = \frac{A}{1 - P_\text{d}/P_\text{u}} \left(\frac{P_\text{d}}{P_\text{u}}\right)^{1/\gamma} \sqrt{\frac{2\gamma}{\gamma-1}\frac{k_\text{B}T}{m}\left[1 - \left(\frac{P_\text{d}}{P_\text{u}}\right)^{(\gamma-1)/\gamma}\right]} \tag{5.10}$$

so $C_{\text{choked,visc.}} = 1.258 A\bar{v} = 5.03 C_{a,\text{molec.}}$. Pumpout times for our cell at 600 mK are given in Table 5.1.

Pumpout Time Measurement

In order to measure the pumpout time of our cell, we monitored the helium density just outside the cell orifice using a fast ion gauge (FIG)[1]. After closing a valve at room

[1] Beam Dynamics Inc., FH-1

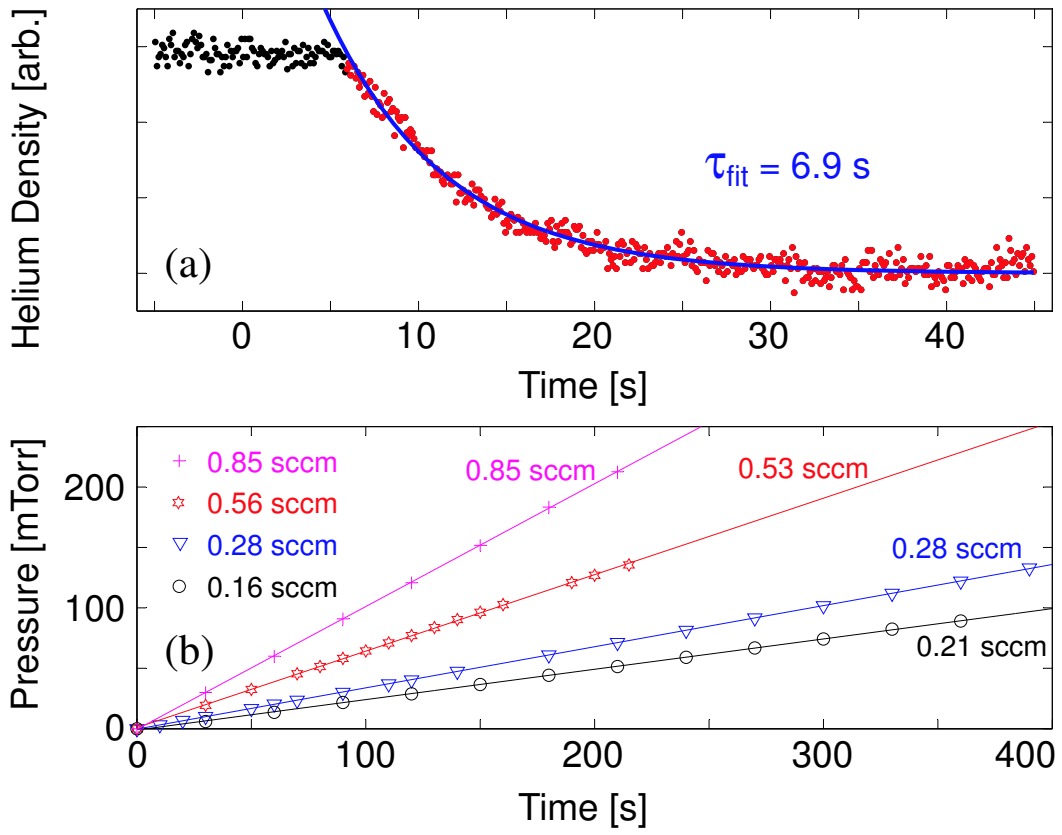

Figure 5.2: Buffer gas density calibration. (a) Time profile of the ^{3}He density measured outside the cell (3 mm diameter molecular beam input aperture) by a FIG at 520 mK. (b) Calibration of the flowmeter using the pressure rise in a known volume.

temperature, the helium density at the position of the FIG decreases as the cell is pumped out. The pumpout time of the fill line is estimated at 20 s, and its total volume should not contribute significantly to the FIG signal. Figure 5.2(a) shows a time profile for and initial flow of 4.3 sccm ^{3}He at 510 mK for the 3 mm diameter cell orifice. Repeated measurements are consistent with the molecular flow calculation and give a pumpout time of $\tau_{\rm fit} = 6.2 \pm 0.7$ s.

To check the calibration of the flowmeter itself, the pressure in an evacuated known volume was measured as a function of time for a given flow rate reading on the gauge.

Results are shown in Fig. 5.2(b). The lines are least squares fits to the points, with the fitted slopes labeled. The points correspond to flowmeter readings in the legend. The agreement is good above 0.3 sccm.

This measurement of our cell conductance gives $C_{\text{exp.}} = 0.11 \pm 0.01\ \ell/\text{s}$ at 515 mK. If f_{sccm} is the flow rate measured by the flowmeter, the ^{3}He density for a cell temperature T (K) will be given by

$$n = \frac{f_{\text{sccm}}}{\sqrt{T}} \times 2.92 \times 10^{15}\ \frac{\sqrt{\text{K}}}{\text{sccm}}\ \text{cm}^{-3} \pm 10\%. \tag{5.11}$$

For the 10 mm diameter hole, divide the right side by $10^2/3^2 \approx 11$.

5.1.2 Loading and Trapping

The verification of trapping relies on a measurement of the lifetime of the trapped molecules. We first saw trapped NH in September 2006, about 4 1/2 years after our first notebook entry for the experiment. Fig. 5.3 shows the fluorescence signal from the trap region with and without buffer gas.

The dissociation discharge causes our PMT signal to go off scale due to electrical pickup while there is a discharge current, which is shown by the sharp over-ranging on the left. Once the discharge has extinguished, the PMT signal shows a combination of fluorescence and scattered light. We utilize a Schott glass filter and an interference filter (10 nm band pass) in front of the PMT for all of the work presented here.

With an evacuated cell (no buffer gas), the PMT signal reverts back to the level of the scattered light once the discharge extinguishes. With buffer gas flow, however, the fluorescence signal persists for more than 100 ms after the discharge has been

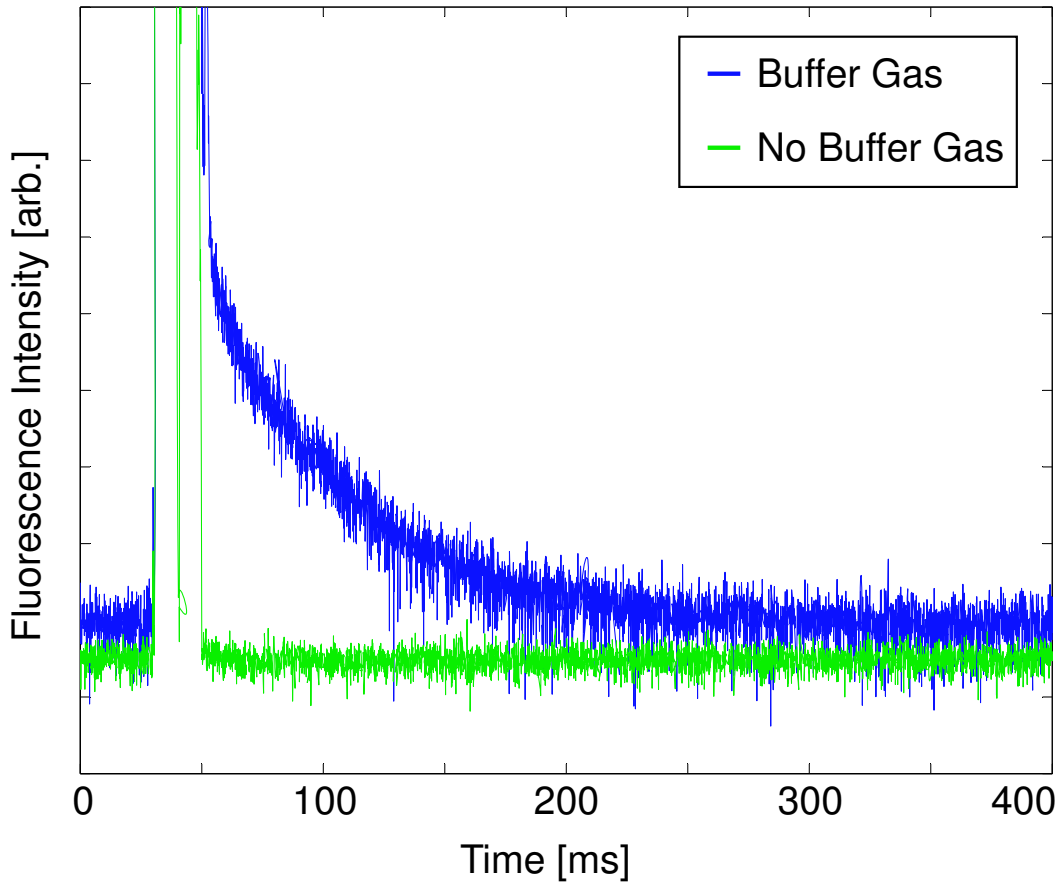

Figure 5.3: Magnetic trapping of NH. Electrical pickup causes the signal to go off-scale while the discharge is on, at the left. The trap depth shown was 1.4 T, lower than our maximum.

turned off. The fluorescence signal shown in Fig 5.3 is for the ground rotational state, low-field seeking Zeeman sublevel only ($\sigma_{\mathrm{UV}} = 29770.654\ \mathrm{cm}^{-1}$).

To examine the loading process, we performed a study of the effect of the duration of the molecular beam pulse on the trapped NH density and lifetime. Fig. 5.4 (Top) shows the NH density for different loading pulse durations with 1.9×10^{15} cm^{-3} ^{4}He at 730 mK. Each curve fits well to a single exponential decay with time constant $\tau = 90 \pm$ ms, but the NH density loaded into the trap changes dramatically with loading pulse duration. Continuous loading of the magnetic trap is verified by the

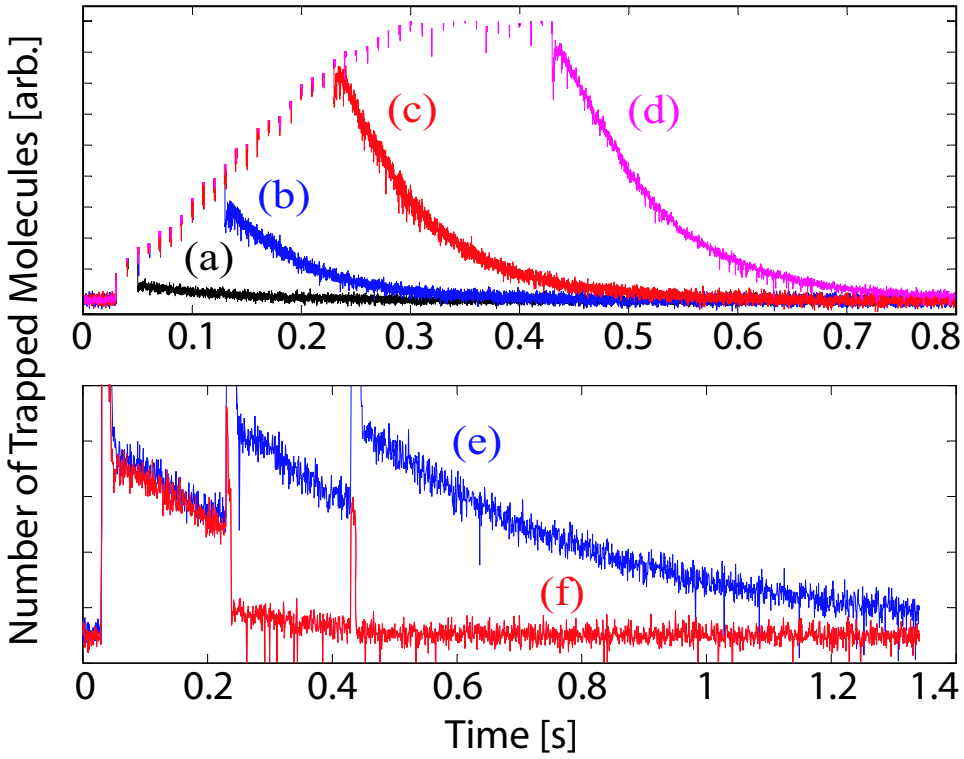

Figure 5.4: Top: Continuous loading of NH into a magnetic trap. Traces correspond to loading pulse durations of (a) 10 ms, (b) 100 ms (c) 200 ms, and (d) 400 ms. The decay portion of each curve fits well to the same exponential time constant. Bottom: At lower temperatures and lower buffer-gas densities, successive pulses knock molecules out of the trap. (e) shows the fluorescence signal for three successive valve pulses, where no buildup is present (f) shows the same number of valve pulses, with the high voltage turned off after the first pulse. The second valve pulse clearly knocks molecules out of the trap.

increase in NH density for longer loading durations until the density saturates to steady-state at around 200 ms of loading.

In the bottom half of Fig. 5.4, a similar analysis has been done at lower buffer-gas density. For these traces, the buffer gas is ^{3}He at a density of 6.5×10^{14} cm^{-3}. Trace (e) shows loading with three successive valve pulses, spaced apart by 100 ms. The second pulse clearly does not add to the first, which can be verified by looking at trace (f), where only the first valve pulse has the high voltage turned on. The second

pulse clearly knocks molecules out of the trap.

It appears that in order to continuously load the trap, the buffer-gas density must be high enough to stop the beam before beam products get to the trap center. This precludes continuous loading of species with high spin-relaxation cross sections since the density should be kept low to achieve long lifetimes. In section 5.3 we show that ^{4}He has a lower Zeeman relaxation cross section than ^{3}He, which helps to explain the data in Fig. 5.4.

5.1.3 Spin-Depolarization and Diffusion Cross Section Measurements

In order to measure the diffusion cross section of NH with helium, in principle we could measure the zero-field diffusion lifetime and use our calibrated buffer-gas density to calculate the cross section. However, we find experimentally that (at zero field) we cannot load molecules into the buffer-gas cell efficiently above $n_{\mathrm{He}} \approx 10^{16}$ cm^{-3}. Without the magnetic trap field to draw molecules into the center of the trap, we also suffer from decreased signal due to a decrease in density and the fact that only the fluorescence from the center of the cell is collected efficiently. While these are solvable problems, we decided to measure the lifetime in the trap and calculate the effect of the trap on the lifetime to extract the elastic cross section.

We first calculate the diffusion lifetime in the cell in zero field. This problem can be solved as a series expansion of the modes of diffusion, but we here take only the lowest-order mode. For a more detailed discussion, see Dima Egorov's thesis [60].

The lowest order mode lifetime can be written as [81]

$$\tau_o = \frac{16 n_{\mathrm{He}} \sigma_{\mathrm{d}}}{3\sqrt{2\pi}} \sqrt{\frac{m_{\mathrm{red}}}{k_{\mathrm{B}} T}} \left[\left(\frac{\alpha_1}{R}\right)^2 + \left(\frac{\pi}{h}\right)^2 \right]^{-1} \tag{5.12}$$

where σ_{d} is the thermal average of the diffusion cross section, R and h are the radius and length of the cell, m_{red} is the reduced mass of the NH-He system and α_1 is the first root of the Bessel function J_0 of order zero ($\alpha_1 \approx 2.4048$ [4]).

The effect of the magnetic trapping field is addressed in Jonathan Weinstein's thesis [198]. For a given trap depth η, the lifetime of the trapped molecules can be calculated from the diffusion lifetime and the magnetic field enhancement. By measuring the lifetime of NH at various trap depths, a one-parameter fit can be made to the data to extract the diffusion cross section. Fig. 5.5 (a) shows the fit, which results in a measured energy transport cross section of $\sigma_{\mathrm{d}} = 2.7 \pm 0.8 \times 10^{-14}$ cm^2 [34] for NH-^{3}He at 690 mK, which corresponds to a rate coefficient of $k_{\mathrm{d}} = 2.1 \pm 0.6 \times 10^{-10}$ cm^{3}s^{-1}.

Fig. 5.5 (b) shows the measured NH trap lifetime vs. ^{3}He buffer-gas density. The dotted line shows the field-free diffusion lifetime calculated from Eq. 5.12. The temperature of the cell increases with buffer-gas density due to the heat load of the incoming and exiting helium gas. For this measurement, the temperature was held at 710 mK to ensure constant temperature all the way up to $n_{\mathrm{He}} = 10^{16}$ cm^{-3}.

One conclusion that can be drawn from Fig. 5.5 (b) is that the workable buffer-gas density range for trapping NH is between 5×10^{14}-5×10^{15} cm^{-3}. This is a far lower density than previous buffer-gas loading experiments, which tend to work above 10^{16} cm^{-3}. If a limit of 500 ms is used as the minimum trap lifetime necessary for an experiment, this permits working with $2\mu_{\mathrm{B}}$ molecules whose collision-induced loss

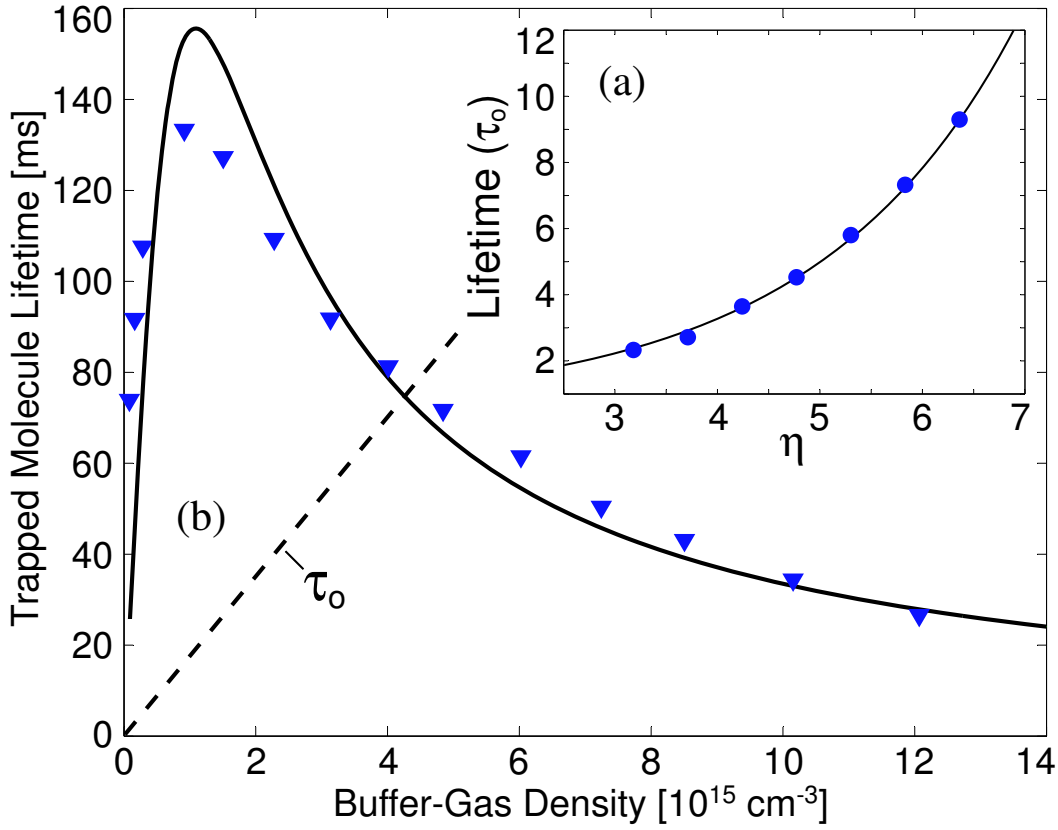

Figure 5.5: Measurements of the diffusion and Zeeman relaxation cross sections. (a) Lifetime vs. trap depth, lifetime in units of the field-free diffusion lifetime (τ_o), trap depth in units of buffer-gas temperature (η).

cross sections are of order $\sigma_{\text{loss}} \approx 3 \times 10^{-19}$ cm^2, which was not previously possible. Furthermore, if the buffer-gas density must be reduced to a certain level to achieve thermal isolation in the future, starting closer to that level may make thermal isolation easier to achieve.

On the left side of Fig. 5.5 (b), the lifetime increases with increasing buffer-gas density. This is expected, and represents the diffusion enhancement of the lifetime. In order for molecules to be lost from the trap, they must either undergo a collisional loss process, or spatially leave the trap. As the buffer-gas density is increased in this

range, the helium enforces diffusive motion of the molecules, lengthening the time it takes for molecules to spatially exit the trap.

As the buffer-gas density is increased further, the lifetime stops increasing and begins to decrease. Here the buffer-gas is causing molecule loss through collision-induced Zeeman relaxation (the temperature is far too low for this to be electronic, vibrational, or rotational excitation).

The Zeeman relaxation cross section can be measured by fitting the data to a model. The diffusion enhancement of the lifetime should be proportional to the buffer gas density (see Eq. 5.12), which means the number of trapped molecules should scale as $N(t) \propto e^{-tA/n_{\mathrm{He}}}$. In contrast, the collision-induced Zeeman relaxation rate should increase linearly with buffer-gas density, so the lifetime set by Zeeman relaxation should scale as $1/n$ and the number of trapped molecules would go as $N(t) \propto e^{-tk_{\mathrm{ZR}}n_{\mathrm{He}}}$. We can then model our trapped molecule number as

$$N(t) = N_o e^{-tA/n_{\mathrm{He}}} e^{-tk_{\mathrm{ZR}}n_{\mathrm{He}}}. \tag{5.13}$$

The effective lifetime, therefore, will be given by

$$\tau_{\mathrm{eff}} = \left[\frac{A}{n_{\mathrm{He}}} + n_{\mathrm{He}}k_{\mathrm{ZR}}\right]^{-1} \tag{5.14}$$

where A contains all of the information about diffusion and the magnetic trap.

The solid curve in Fig. 5.5 (b) is a fit to the data using Eq. 5.14. The two fitting parameters are A and the collision-induced Zeeman relaxation rate, for which we obtain $k_{\mathrm{ZR}} = 3.0 \pm 0.9 \times 10^{-15}$ cm^{3}s^{-1} for NH-^{3}He at 710 mK. This corresponds to a cross-section of $\sigma_{\mathrm{ZR}} = 3.8 \pm 1.1 \times 10^{-19}$. For the ratio of diffusive to inelastic

cross sections, therefore, we obtain

$$\gamma \equiv \frac{\sigma_{\text{diffusion}}}{\sigma_{\text{ZeemanRelaxation}}} = 7 \times 10^4. \tag{5.15}$$

The rule of thumb for buffer-gas loading is that we require $\gamma > 10^4$, which is easily satisfied by NH.

These cross sections for for NH-^{3}He collisions were calculated by Krems and co-workers [121, 45]. They obtained rate coefficients of $k_{\text{ZR}} = 4.20 \times 10^{-16}$ cm^{3}s^{-1} and $k_{\text{d}} = 1.49 \times 10^{-10}$ cm^{3}s^{-1} at a collision energy of 0.5 K. A naive scaling of the calculated rate coefficients with $\sqrt{T}$ results in good agreement with our measured diffusive rate coefficient, but the Zeeman relaxation we measure is about an order of magnitude higher than the predicted value.

The discrepancy may be attributable to two things. First, the predicted $l = 3$ shape resonance position in energy is highly sensitive to the details of the NH-^{3}He potential, which are calculated from limited experimental data. Scaling the potential by 10% shifts the position of the resonance by about 1 K, which should dramatically affect our measured rate. Second, the rate we measure is averaged in temperature and magnetic field, while the calculated rates are quoted for uniform fields and precise collision energies (note the difference between collision energy in Kelvin units and temperature in Kelvin units). It is possible that even though the average collision energy misses the shape resonance, the thermal average effectively means the effects of the resonance are present for all molecules, which may explain the discrepancy.

5.2 Calibration of Trapped Molecule Density

All of the results from section 5.1 were achieved with a ∅3 mm molecular beam input aperture on the cell. While taking the measurements presented above it became clear that our charcoal tube could handle higher flow rates than we were using and still not cause too much heating on the cell. The aperture was then increased to 1 cm diameter to allow the loading of higher number of molecules.

The fluorescence spectroscopy we used for the data in section 5.1 gave us an estimate of 10^8 ground-state NH molecules, but the collection efficiency of fluorescence detection systems is often difficult to estimate, and the 10^8 was our best order-of-magnitude guess.

In order to calibrate our fluorescence system, we performed laser absorption spectroscopy of the trapped imidogen simultaneous with fluorescence. Fig. 5.6 shows the signal from balanced absorption spectroscopy of trapped NH. These data were taken at the peak of the *fluorescence* spectrum at a dye laser frequency of 14885.335 cm^{-1}. The relative heights of the fluorescence and absorption features change dramatically above this frequency, so future calibrations should be made at the peak of the fluorescence spectrum. The average of the input and output laser powers was 1.2 μW, in which range it has been empirically verified that the fractional absorption is independent of the laser power.

There are some subtleties involved in converting a fractional absorption into a trapped molecule number, so this section begins with a description of how this would work in zero-field before adding the effect of an inhomogeneous magnetic trapping field.

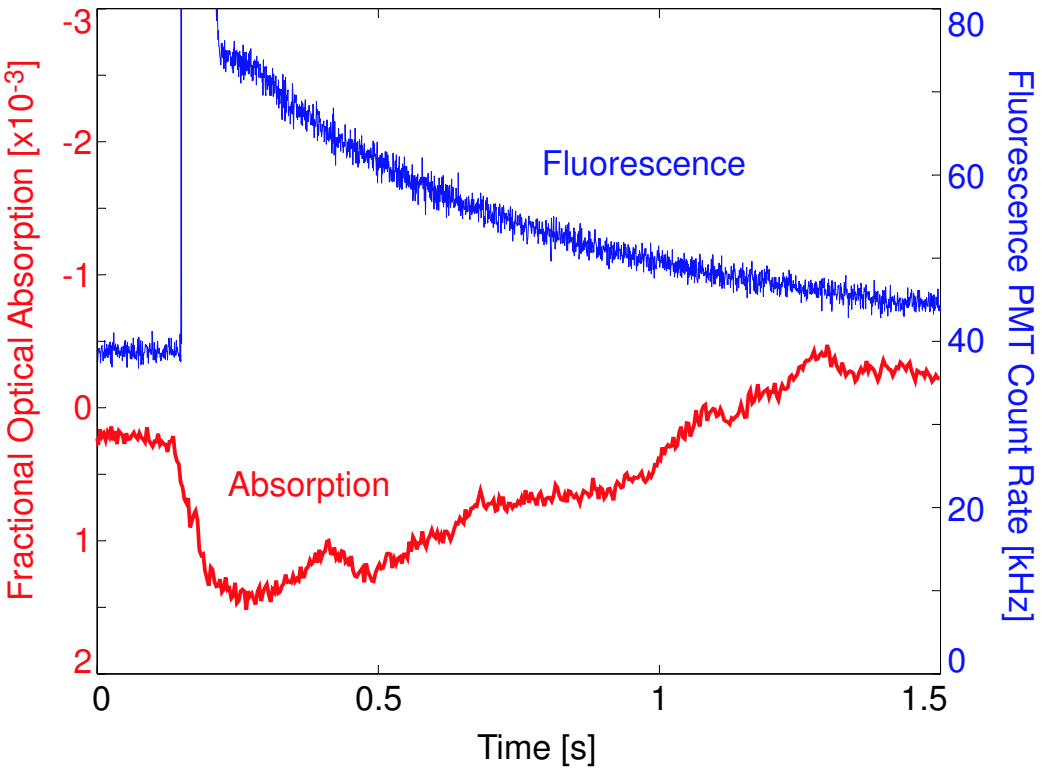

Figure 5.6: Absorption signal of magnetically trapped NH molecules.

In zero field, the fractional optical absorption is given by Beer's Law (Eq. 4.1):

$$\frac{I}{I_o} = e^{-\sigma n_{\mathrm{NH}} \ell} \tag{5.16}$$

where σ is the photon scattering cross section and ℓ is the interaction distance. The narrow-band laser excitation will not be resonant will all molecules due to the Doppler and Hyperfine effects. One way to include this consideration is to define an *effective* cross section:

$$\sigma_{\mathrm{eff}} = \frac{\Delta\nu_{\mathrm{nat}}}{\Delta\nu_{\mathrm{I}}}\sigma = \frac{\Delta\nu_{\mathrm{nat}}}{\Delta\nu_{\mathrm{I}}}\frac{3\lambda^2}{2\pi} \tag{5.17}$$

where $\Delta\nu_{\mathrm{nat}} = 1/2\pi\tau_{\mathrm{nat}}$ is the natural linewidth of the transition and $\Delta\nu_{\mathrm{I}}$ contains inhomogeneous broadening such as Doppler broadening and Hyperfine broadening.

We will here ignore the Hyperfine broadening for simplicity (both of these terms will be far smaller than the magnetic broadening caused by the trap when we include the effect of the field).

Eq. 4.1 and 5.17 can be used together to convert a zero-field fractional laser absorption into an average molecule density, as was done for the beam loading demonstration experiment [58]. When the trapping field is turned on, however, there is additional inhomogeneous broadening due to the Zeeman shift of the transition frequency. One way to include this effect would be to identify $\Delta\nu_{\mathrm{I}}$ with the Zeeman broadening, the lineshift for which can be found in Appendix A and is given by

$$\Delta\nu = \frac{\partial\nu}{\partial B}\frac{\partial B}{\partial z}\ell. \tag{5.18}$$

In the limit of small fractional absorption we can combine Eq. 4.1 and 5.18 to give us

$$\frac{I}{I_o} \approx n_{\mathrm{NH}}\sigma\frac{\Delta\nu_{\mathrm{nat}}}{\frac{\partial\nu}{\partial B}\frac{\partial B}{\partial z}}. \tag{5.19}$$

This analysis, however, has neglected the effects of optical pumping, saturation and molecular motion in the trap. We can first address potential optical pumping by examining the size of the region of the trap that is resonant with our laser. For any particular molecule moving through the trap with some speed relative to the direction of the laser beam, the Doppler effect can be ignored. There will be some field value for which this molecule is resonant with the laser, and the molecule need only to find it to be on resonance. Each molecule may have a different location where resonance is met due to their different Doppler shifts, but we will assume they all have equal probabilities of passing through their respective resonant regions.

If the laser beam has a large diameter compared to the trap and if we ignore

polarization effects, the region of space where the resonance condition is met is a surface of constant magnetic field magnitude with some thickness. The thickness is given by the natural width of the transition ($\Delta\nu_{\mathrm{nat}}$), the magnetic field gradient $\partial B/\partial z$ and the Zeeman shift of the line $\partial\nu/\partial B$:

$$\Delta z = \frac{\Delta\nu_{\mathrm{nat}}}{\frac{\partial\nu}{\partial B}\frac{\partial B}{\partial z}}. \tag{5.20}$$

For our trapped NH, this amounts to a thickness of $\Delta z = 5$ μm, which a 2500 cm/s NH molecule will traverse in about 20 ns.

Clearly, then, we need not worry about optical pumping since molecules will never spend enough time in the resonance region to be eligible for more than one excitation. The fluorescence (and absorption) rate will be entirely limited by the incidence rate of molecules onto this thin resonant region. This incidence rate will be given by

$$\dot{N}_{\mathrm{molecule}} = \frac{1}{4} n_{\mathrm{NH}} \bar{v} A \tag{5.21}$$

where $\bar{v}$ is the average molecule velocity and A is the surface area of the resonance region.

If the probability of excitation for a molecule that passes through the resonance region is unity, then the photon scattering rate is equal to $\dot{N}$, the incidence rate of molecules onto the resonant region. However, this is where it becomes important to examine in detail the probability of excitation.

A molecule with a magnetic field dependent transition frequency moving through an inhomogeneous magnetic field with a fixed-frequency laser field is equivalent to a stationary molecule experiencing a chirped laser frequency. The probability of

excitation will then depend on the chirp rate, which will be given by

$$\frac{\mathrm{d}\nu}{\mathrm{d}t} = \frac{\partial\nu}{\partial B}\frac{\partial B}{\partial z}v_z \approx 20 \text{ THz/s}. \tag{5.22}$$

The excitation probability will be given by the Landau-Zener diabatic transition rate [165]:

$$P_{\mathrm{ex}} = 1 - e^{-\Omega^2/\frac{\mathrm{d}\nu}{\mathrm{d}t}} \tag{5.23}$$

where Ω is the Rabi frequency, which we can write in terms of the natural lifetime τ_{nat} and the saturation parameter $s_o \equiv I/I_{\mathrm{sat}}$ as

$$\Omega^2 = \frac{s_o}{2\tau_{\mathrm{nat}}^2}. \tag{5.24}$$

If we are saturating the transition ($s_o = 1$), this gives us a coupling strength of $\Omega^2 = 2\pi \times 411$ GHz/s. This is smaller than our maximum angular chirp rate of $2\pi \times 20$ THz/s, so we can expand the exponential to write

$$P_{\mathrm{ex}} \approx \frac{\Omega^2}{\frac{\mathrm{d}\nu}{\mathrm{d}t}} = \frac{s_o/2\tau_{\mathrm{nat}}^2}{\frac{\partial\nu}{\partial B}\frac{\partial B}{\partial z}v_z}. \tag{5.25}$$

We have a thermal distribution and therefore need to take the ensemble average:

$$\langle P_{\mathrm{ex}}\rangle = \frac{s_o}{2\tau_{\mathrm{nat}}^2\frac{\partial\nu}{\partial B}\frac{\partial B}{\partial z}}\left\langle\frac{1}{v_z}\right\rangle. \tag{5.26}$$

For a Maxwell-Boltzmann distribution, numerical integration yields $\langle 1/v_z\rangle \approx 3.52/\bar{v}$, giving us

$$\langle P_{\mathrm{ex}}\rangle = \frac{(3.52)\pi s_o}{\bar{v}\ \tau_{\mathrm{nat}}}\frac{1}{2\pi\tau_{\mathrm{nat}}\frac{\partial\nu}{\partial B}\frac{\partial B}{\partial z}} \tag{5.27}$$

$$= \frac{(3.52)\pi s_o}{\bar{v}\ \tau_{\mathrm{nat}}}\Delta z \tag{5.28}$$

where we have used Eq. 5.20 in getting from Eq. 5.27 to Eq. 5.28. For saturation parameters greater than about 20%, the full exponential form must be used because $\langle P_{\rm ex}\rangle$ approaches unity. At saturation we expect an excitation probability of 99.3%.

Eq. 5.28 can be understood in the following manner. The average time a molecule spends in the resonant region is simply the width of the region divided by the rms speed along the direction of the width:

$$t_{\rm transit} = \frac{\Delta z}{\sqrt{\bar{v_z^2}}} = \frac{\Delta z}{\sqrt{\frac{\pi}{8}}\bar{v}} \approx \frac{(1.60)\Delta z}{\bar{v}}. \tag{5.29}$$

We can now rewrite Eq. 5.28 in terms of the transit time across the resonant region:

$$\langle P_{\rm ex}\rangle = (6.43)\frac{t_{\rm transit}}{\tau_{\rm nat}} s_o. \tag{5.30}$$

To within a factor of unity, Eq. 5.30 is what we might have expected from the beginning. The probability of excitation should be about 1 for a transit time equal to the natural lifetime when the transition is being saturated.

For low laser intensities, we can combine Eq. 5.28 with Eq. 5.21 to get the photon scattering rate $\dot{N}_{\rm photon}$:

$$\dot{N}_{\rm photon} = \dot{N}_{\rm molecule}\langle P_{\rm ex}\rangle = (3.52)\frac{\pi}{4}\frac{A s_o \Delta z}{\tau_{\rm nat}} n_{\rm NH}. \tag{5.31}$$

The incidence rate of photons will be $IA_{\rm L}/\hbar\omega$ for incident intensity I with a laser beam cross-sectional area $A_{\rm L}$. If the laser beam radius is smaller than the distance between the resonant field and the center of the trap, we can identify $A_{\rm L}$ with (half of) the surface area A of the resonant region. We can now write and expression for the fractional absorption

$$\frac{I}{I_o} = \frac{\dot{N}_{\rm molecule}\langle P_{\rm ex}\rangle}{IA/2\hbar\omega} \tag{5.32}$$

$$= (3.52)\pi\ \Delta z\ n_{\rm NH}\ \frac{\hbar\omega}{2\tau_{\rm nat}\ I_{\rm sat}} \tag{5.33}$$

$$= (3.52)\pi\ \sigma\ n_{\rm NH}\ \Delta z \tag{5.34}$$

where for the last step we have used the following expression for the photon absorption cross section

$$\sigma = \frac{\hbar\omega}{2\tau_{\rm nat} I_{\rm sat}}. \tag{5.35}$$

Comparing Eq. 5.34 to Eq. 5.19, we see that the result be obtained from Beer's Law and the result from Landau-Zener dynamics are identical within a numerical factor ($3.52\pi \approx 11.1$), which sets the point at which each is valid. For saturation parameters less than 1/10 or so, the Landau-Zener formalism must be used because the excitation probability is low. Above that point, the photon scattering rate is simply given by Eq. 5.21 and the fractional absorption will be

$$\frac{I}{I_o} = \frac{dotN_{\rm molecule}}{IA/2\hbar\omega} \tag{5.36}$$

$$= \frac{\sigma\ n_{\rm NH}\ \bar{v}\ \tau_{\rm nat}}{s_o}. \tag{5.37}$$

The data in Fig. 5.6 were taken in the laser-intensity insensitive regime, so Eq. 5.34 is applicable here. The fractional absorption of $I/I_o \approx 1.2 \times 10^{-3}$ gives us a density of 3.6×10^8 cm^{-3} at the resonance region. The total photon absorption rate is then 2.4 GHz, so our 35 kHz PMT count rate corresponds to a detection efficiency of 1.4×10^{-5} for a fundamental frequency of 14885.335 cm^{-1}.

5.3 Spin Relaxation of all Stable He-NH Isotopic Pairs

The measurement of the spin relaxation rate for NH-^{3}He does not really address the mechanism for the relaxation described by Krems and co-workers. Not only is there a bit of disagreement in the numbers, but it is possible to achieve numbers that agree as a matter of coincidence. In order to investigate whether the qualitative description of the collision-induced Zeeman relaxation occurring due to the spin-spin interaction mixing in some $N = 2$ is a good model, multiple experiments can be done to investigate scaling laws.

One approach to this would be to change the temperature and try to trace out the $l = 3$ shape resonance. Unfortunately, the fact that we have a thermal average tends to smear out the resonance to the point that we would not be able to resolve it in our work here.

Instead, we decided to investigate the predicted $1/B^2$ scaling of the relaxation rate with the rotational constant. This was chosen for multiple reasons. First, it is easy to change B by a factor of 2 by switching from NH to ND. Since our production and loading method is insensitive to the internal details of the molecule under investigation, implementing this shift is trivial. Second, by making the shift from NH to ND, the electronic properties remain almost identical and we will in large part leave the spin-spin interaction λ_{SS} and the imidogen-helium potential unaffected. This allows us to separate out the influence of these parameters on the relaxation rate. Last, the scaling with B is the most important part of the model from our perspective since

rotational constants are easily found in the literature (as opposed to He-molecule potentials). These considerations will likely determine which molecules will be pursued for buffer-gas loading.

There are four stable isotopomers of the imidogen radical: two fermions (NH, ^{15}ND) and two bosons (ND, ^{15}NH). There is good spectroscopic data available for NH and ND, a small amount on ^{15}NH [194], and we were not able to find any data on ^{15}ND. Furthermore, since collisional shape resonances are a result of the bound states of the NH-He complex, changing helium isotopes will provide a check for their influence. In fact, the $l = 3$ state of NH-^{4}He is a true bound state, so the $l = 3$ shape resonance does not even exist for the ^{4}He system.

5.3.1 Spectroscopy and Isotope Shifts

In order to verify that we are trapping the proper isotopomers of imidogen, we would like to be able to separate them spectroscopically. There is good data on the $A \leftrightarrow X$ transitions of NH and ND, and the isotope shift is more than 5 cm^{-1}, which is far more broad than our Zeeman-broadened spectrum and is therefore easily distinguishable from NH.

We were unable to find $A \leftrightarrow X$ data for the ^{15}N-bearing isotopomers. This is potentially problematic for two reasons. First, we need to find the transitions in order to detect our trapped molecules. Second, there is an effect called "hydrogen substitution" wherein deuterated ammonia ND_3 will exchange hydrogen isotopes with the walls of tubing and become NH_3. We therefore require that all four of our isotopomers be distinguishable in the magnetic trap so that we can be sure of the isotopic identity

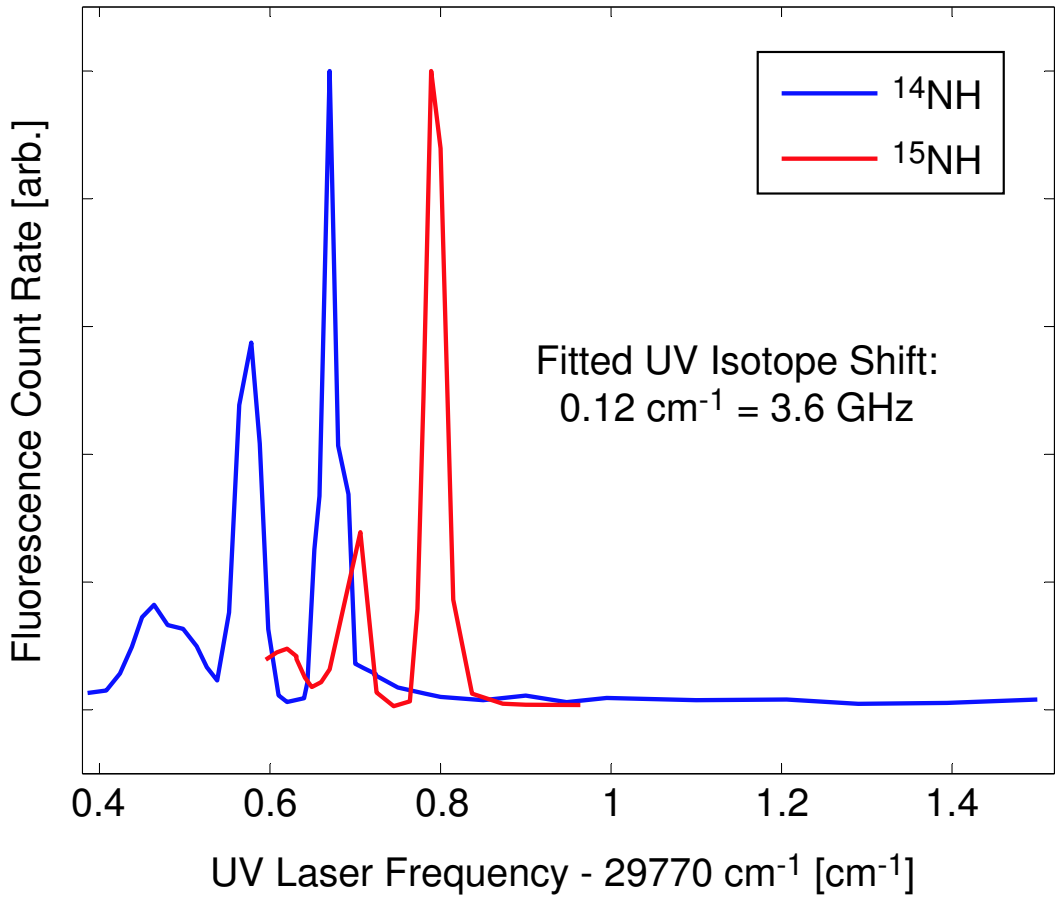

Figure 5.7: Fluorescence spectra of ^{14}NH and ^{15}NH in the magnetic trap. The shift measured from these spectra is 0.12 cm^{-1}, and the ^{14}N to ^{15}N shift for ND is the same within this precision. Note that the shift is given for the second harmonic beam, not the fundamental.

of our trapped sample.

Figure 5.7 shows the spectra of NH and ^{15}NH in the magnetic trap. The substitution $^{14}\text{N} \rightarrow {}^{15}\text{N}$ gives a frequency shift of $\Delta\nu = +0.12$ cm^{-1} for the R_1 line of the $A \leftrightarrow X$ transition of both the deuterated and undeuterated isotopes. The spectra are distinguishable from one another by shifting laser frequency, so we are able to address each of the four isotopes separately.

Table 5.2: Zeeman relaxation rate coefficients for imidogen in collisions with helium in units of 10^{-15} cm^{3}s^{-1}. The uncertainties below are statistical, and the uncertainty in the absolute buffer-gas density results in a systematic uncertainty of $\pm 30\%$ common to all points. The ^{3}He measurements were taken at $T = 580 - 633$ mK and the ^{4}He measurements were taken at $T = 720 - 741$ mK

	^{3}He	^{4}He
^{14}NH	4.5 ± 0.3	1.1 ± 0.1
^{15}NH	5.1 ± 0.4	1.4 ± 0.2
^{14}ND	9.3 ± 0.8	4.0 ± 0.7
^{15}ND	13.0 ± 0.8	2.8 ± 0.6

5.3.2 Analysis of B Dependence

The Zeeman relaxation rate coefficient was measured for each isotopomer with each isotope of helium buffer-gas separately, and they are summarized in Table 5.2. Figure 5.8 shows the measured rate coefficients vs $1/B^2$. The solid lines are one-parameter fits to a/B^2 where a is the fitting parameter. The ^{4}He data fit well to the predicted scaling law. If the exponent is also free for the fit, the best fits to a/B^b give $b = 1.6 \pm 0.4$ for ^{4}He and $b = 1.4 \pm 0.2$ for ^{3}He. It is clear that there is good agreement for the ^{4}He data, but the ^{3}He data do not fit well to $1/B^2$.

Another conclusion that can be drawn from Fig. 5.8 is that ^{3}He is far more likely to cause collisional Zeeman relaxation than the less-standard ^{4}He buffer-gas. Both this and the deviation from $1/B^2$ for ^{3}He can be attributed to the presence of the predicted $l = 3$ shape resonance in the imidogen-^{3}He system.

The shape resonance arises because there is a bound state for the rotating collision complex with $l = 3$ that is unbound for the nonrotating complex. A helium atom can approach the imidogen and the two can start rotating with the helium trapped behind the centrifugal barrier, which can lead to an enhanced probability for the imidogen

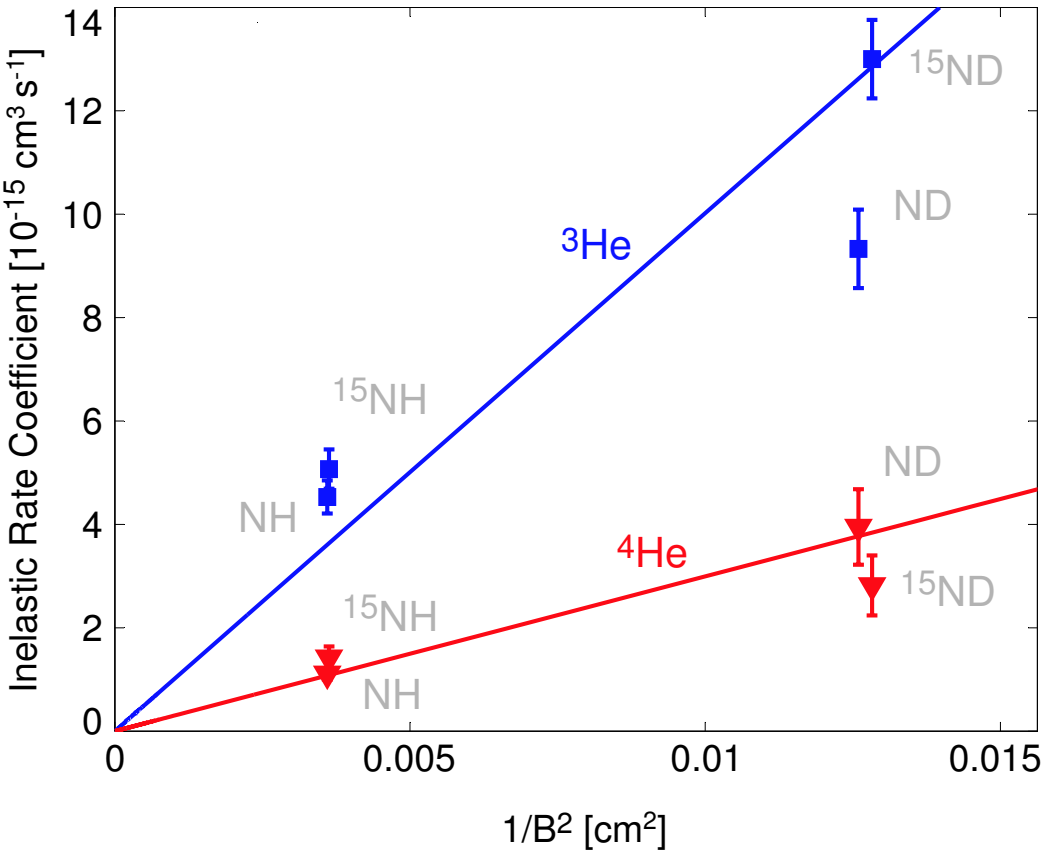

Figure 5.8: Scaling of the collision-induced Zeeman relaxation cross section with $1/B^2$. Straight lines that include the origin obey the $1/B^2$ dependence, and agreement is good for ^{4}He. The ^{3}He data do not exhibit this dependence due to the proximity of the $l = 3$ NH-^{3}He shape resonance in this temperature range.

to emerge in a different Zeeman sublevel. The $l = 3$ state, however, is a true bound state for ^{4}He since the rotational level spacing is smaller with the larger mass helium atom. There is no $l = 3$ shape resonance for imidogen-^{4}He.

Shape Resonance Shift

We can also estimate the effect of the imidogen isotopomer on the shape resonance energy. The helium-imidogen complex can be modeled as Hund's case (a) [45], so the rotational energy of the whole complex will go as $Bl(l+1)$ to first order. The energy

shift of the rotational level with rotational quantum number l that occurs in switching from a collisional complex with rotational constant B_o to one with B' will be given by

$$\Delta E_{\text{rot.}} = (B_o - B')l(l+1). \tag{5.38}$$

But we can estimate the new rotational constant to be $B' = (\mu_o/\mu')B_o$ where μ is the reduced mass of the complex, giving us

$$\Delta E_{\text{rot.}} = B_o \left(1 - \frac{\mu_o}{\mu'}\right) l(l+1). \tag{5.39}$$

Changing the mass of the collision complex will also shift the binding energy of the $v = 0$ vibrational state due to its effect on the zero-point energy ($E_{\text{z.p.e.}}$) of vibration.

$$\Delta E_{\text{vib.}} = \left(1 - \sqrt{\frac{\mu_o}{\mu'}}\right) E_{\text{z.p.e.}} \tag{5.40}$$

The rotational constant of NH-^{3}He is calculated to be approximately $B_o = 0.37$ cm$^{-1} \approx$ 500 mK and the zero-point energy is $E_{\text{z.p.e.}} = 16.28$ cm$^{-1} \approx 23.4$ K [45]. Switching from NH to ND or ^{15}NH should move the $l = 3$ resonance energy by $\Delta E_{\text{rot.}} = 65$ mK and $\Delta E_{\text{vib.}} = 120$ mK. This results in the resonance moving to lower energy by about 200 mK.

The consequence of this estimate is that we do expect to see the position of the resonance to be somewhat different for imidogen isotopomers with different masses. The spread of collision energies between our trapped imidogen and helium will be of order 500 mK, so shifting the resonance by 200 mK should change (but probably not eliminate) its contribution to the Zeeman relaxation cross section. This mass shift would also lead us to expect that the two isotopomers with equal masses, ^{15}NH and ND, should experience similar contributions from the shape resonance.

5.4 Vibrational Spontaneous Emission Lifetime Measurement

In the first neutral molecule trapping experiment, our group cooled CaH in both the $v = 0$ and $v = 1$ states [197, 198]. The CaH($v = 1$) molecules were observed to persist in the buffer gas for a time that was indistinguishable from the CaH($v = 0$) lifetime, and a limit was placed on the vibrational quenching rate coefficient of $k_q < 10^{-16}$ cm^{3}s^{-1}. The $v = 1$ population was about a factor of 100 times smaller than the $v = 0$ population, which corresponds to a vibrational temperature of nearly 400 K. Clearly, the vibrational degree of freedom remained far out of thermal equilibrium with the translational and rotational temperatures of a fraction of a Kelvin.

Following this experiment, the Meijer group in Berlin was able to prepare and Stark-decelerate OH($v = 1$) to load an AC electric trap [190]. The beam of OH($v = 0$) radicals was produced by photodissociation of an expanding supersonic jet of HNO_3 by an ArF excimer laser. The OH($v = 1$) state was prepared by optical pumping of the $A^2\Sigma^+(v = 1) \leftarrow X^2\Pi_{3/2}(v = 0)$ transition, followed by spontaneous decay to $X^2\Pi_{3/2}(v = 1)$. They measured the trap loss rate and were able to measure the spontaneous emission lifetime of the upper Λ-doublet component of $X^2\Pi_{3/2}$ OH($v = 1$) to be $\tau_{rad,\mathrm{exp.}} = 59.0 \pm 2.0$ ms, which agrees with their calculated value of 58.0 ± 1.0 ms. The $v = 1$ state lies about 5000 K above the $v = 0$ state.

Since buffer-gas cooling is state-insensitive with respect to the molecule being cooled, we have not worked hard to produce molecules in any particular internal state. It was possible that our glow discharge was producing vibrationally excited molecules

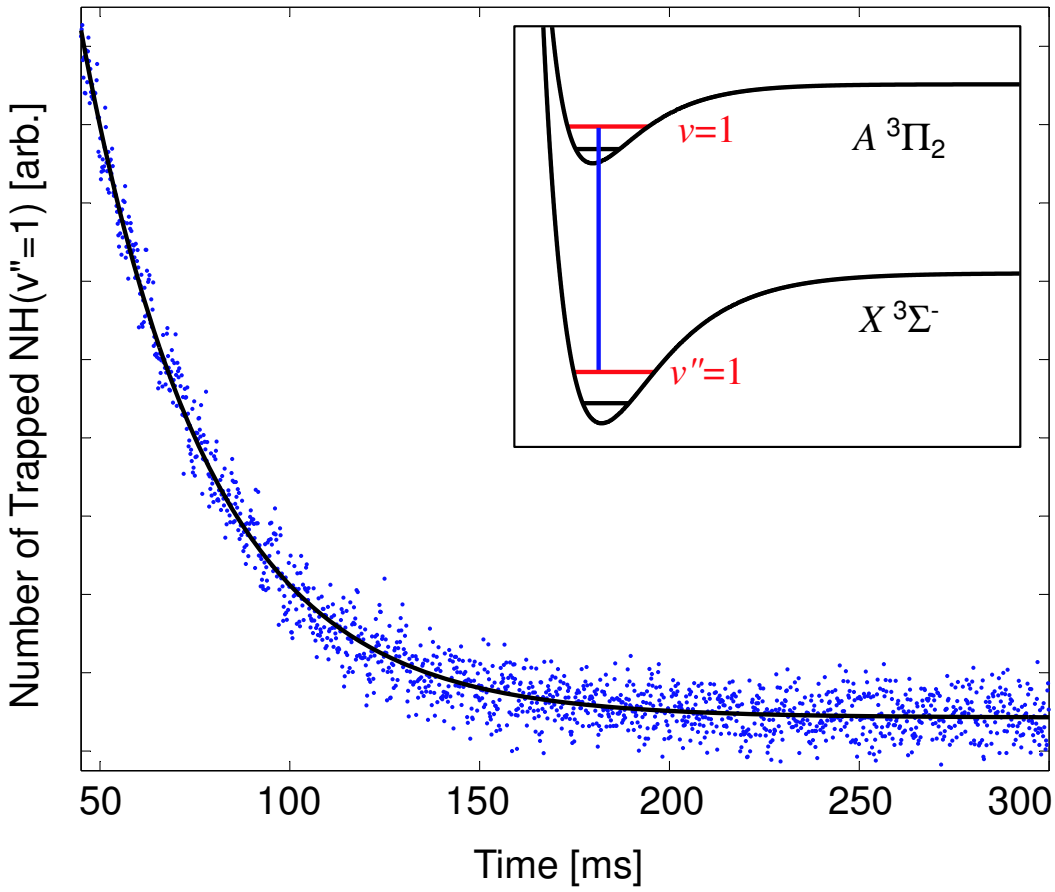

Figure 5.9: Time profile for trapped NH($v = 1$) measured using (1,1) laser-induced fluorescence.

and they were being loaded into the trap during our work with the vibrational ground state molecules. To investigate this, we tuned our detection laser to the $1 \leftarrow 1$ transition and found that we had about 1/10th as many NH($v = 1$) in our trap as NH($v = 0$), which corresponds to a vibrational temperature of about 2000 K. We were not able to detect any NH($v = 2$) molecules above our noise.

Figure 5.9 shows the time profile of the fluorescence signal from trapped NH($v = 1$). The lifetime of the signal is much shorter than NH($v = 0$) (*e.g.* Fig. 5.3), which we found to be due to spontaneous emission.

5.4.1 Vibrational Spontaneous Emission Theory

It is straightforward to show that vibrational spontaneous emission rate is proportional to the square of the slope of the transition dipole moment function (μ) with the internuclear spacing of the molecule. To see this, we can write the spontaneous emission lifetime as

$$\tau = \frac{3c^2e^2}{4\alpha\omega^3} \left|\langle \Psi' \left|\boldsymbol{\mu}\right| \Psi\rangle\right|^{-2} \tag{5.41}$$

where ω is the transition frequency and $|\Psi\rangle(|\Psi'\rangle)$ is the total wavefunction of the initial(final) state. We can write $|\Psi\rangle$ as a product of the electronic, vibrational, and rotational wavefunctions, to give us

$$\langle \Psi' \left|\boldsymbol{\mu}\right| \Psi\rangle = \langle \psi'_{\rm rot} \left|\langle v' \left|\langle \psi'_{\rm el} \left|\boldsymbol{\mu}\right| \psi_{\rm el}\rangle\right| v\rangle\right| \psi_{\rm rot}\rangle \,. \tag{5.42}$$

The rotational part will enforce the selection rule $\Delta J = \pm 1$ but will otherwise not affect our analysis here, so we will ignore it in the following. Also, since we are interested in vibrational transitions within the same electronic state, $\psi'_{\rm el} = \psi_{\rm el}$.

The dipole moment *operator* $\boldsymbol{\mu}$ is given by

$$\boldsymbol{\mu} = \sum_i e_i \mathbf{r}_i \tag{5.43}$$

where the sum occurs over all of the charges in the molecule. We will here restrict ourselves to the electrons. We can use the dipole moment *operator* $\boldsymbol{\mu}$ to construct the dipole moment *function* $\mu(R)$ by integrating over the electronic wavefunctions:

$$\mu(R) \equiv \langle \psi_{\rm el} \left|\boldsymbol{\mu}\right| \psi_{\rm el}\rangle \tag{5.44}$$

$$= e \sum_i \int \mathrm{d}^3\mathbf{r}_i \; \psi_{\rm el}(\mathbf{r}_i, R) \; \mathbf{r}_i \; \psi_{\rm el}(\mathbf{r}_i, R) \tag{5.45}$$

where R is the internuclear separation. If we assume that the dipole moment function is independent of the internuclear spacing in the molecule since it operates on the electrons only, we can factor out the vibrational wavefunctions to get

$$\mu \times \langle v'|v\rangle \,. \tag{5.46}$$

The problem with this assumption becomes obvious when we notice that the vibrational wavefunctions in the same potential well are orthonormal ($\langle v'|v\rangle = \delta_{v'v}$). If the dipole moment function were independent of internuclear spacing, there would be no dipole-allowed vibrational transitions within the same electronic state. For example, heteronuclear molecules have no dipole moments, and their dipole moment functions are therefore constant ($\mu(R) = 0$) and they also do not exhibit pure vibrational electric dipole transitions.

If we instead notice that the dipole moment function will depend on the internuclear spacing (R), we can write it as a series expansion:

$$\mu(R) = \mu_o + \frac{\partial \mu}{\partial R} R + \cdots . \tag{5.47}$$

The transition matrix element of the first term will be zero as in Eq. 5.46, but the second term is nonzero:

$$\langle v' \left|\mu(R)\right| v\rangle = \left\langle v' \left| \frac{\partial \mu}{\partial R} R \right| v \right\rangle . \tag{5.48}$$

This expression, along with Eq. 5.41, shows that the spontaneous emission rate will be proportional to the square of the slope of the dipole moment function with internuclear spacing R.

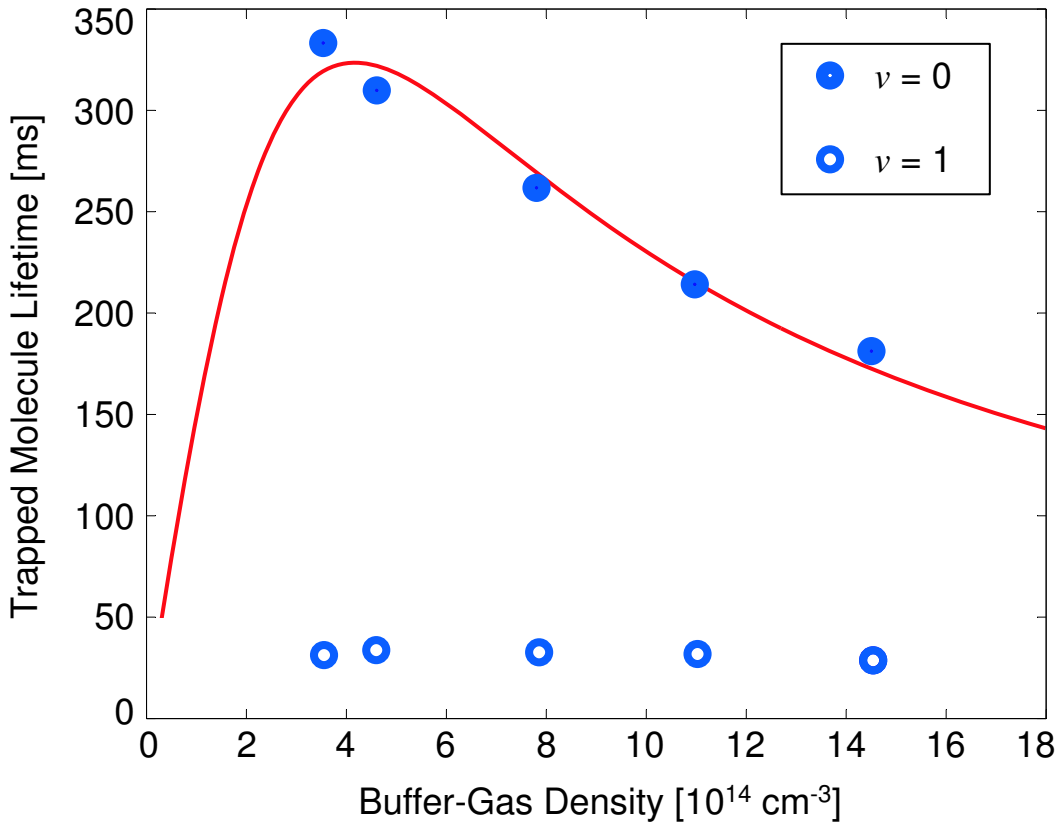

Figure 5.10: Measured NH($v = 0, 1$) lifetime vs buffer-gas density. The NH($v = 0$) lifetime shows behavior similar to Fig. 5.5, but the NH($v = 1$) lifetime is relatively insensitive to the buffer-gas.

5.4.2 Vibrational Quenching Rate Coefficient

In order to use our trapped NH($v = 1$) to measure the vibrational lifetime, we need to ensure that we are not being fooled by vibrational quenching collisions. To examine this, we measured the NH($v = 1$) lifetime in the trap as we changed buffer-gas densities. The results of this measurement are shown in Fig. 5.10. The lifetime of the vibrational ground state depends on the buffer-gas density in the same way as described by Eq. 5.14. The NH($v = 1$) state lifetime, however, is dramatically shorter and comparatively insensitive to the buffer-gas density, as expected for spontaneous

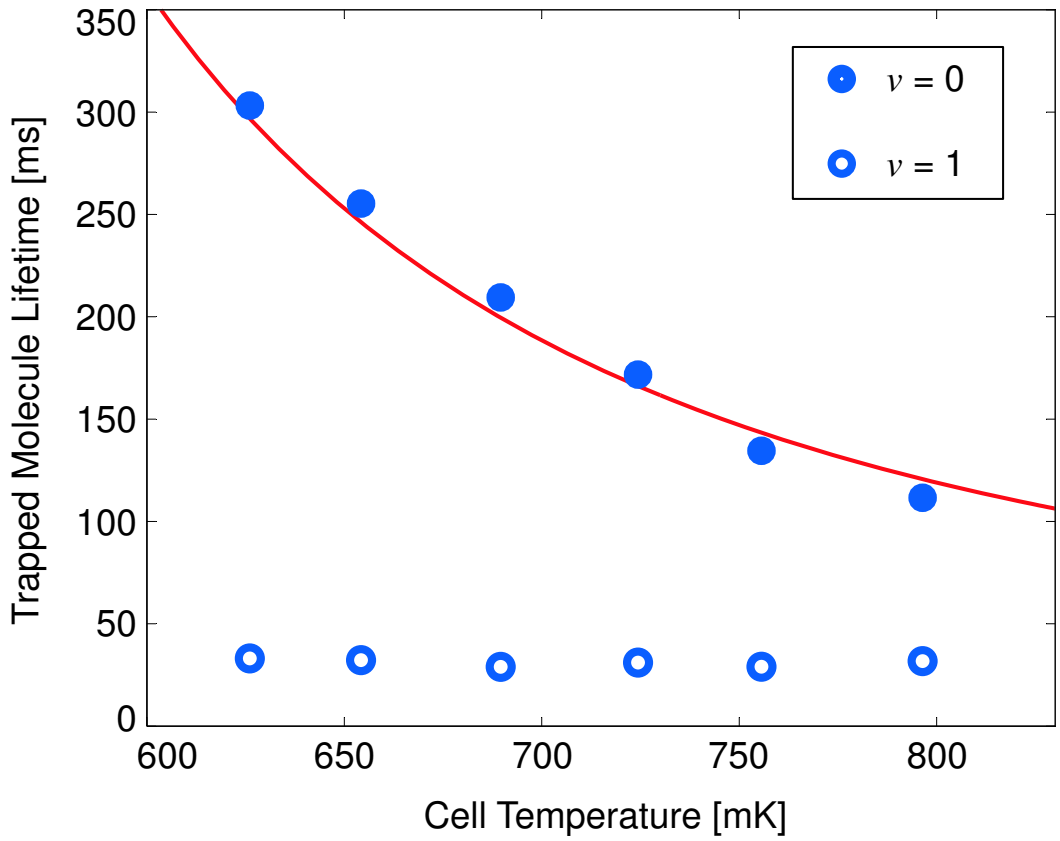

Figure 5.11: Measured NH($v = 0, 1$) lifetime vs buffer-gas temperature.

emission.

Another important test to show that the lifetime we measure is limited by the spontaneous emission lifetime is shown in Fig. 5.11. Here the temperature of the buffer-gas was changed by heating the cell, which changes the helium collision rate and the trap depth. Once again, we see that the NH($v = 0$) shows the previously studied dependence (see Fig. 5.5(b)) and that NH($v = 1$) has a much shorter lifetime that is relatively insensitive to the buffer-gas density. This further supports the conclusion that the lifetime is limited by spontaneous emission.

In order to quantify the possible effect of collisional quenching of the $v = 1$ state,

we must first correct for the finite hold time of the trap. We can model the density in the trap as

$$N(t) = N_o e^{-tA/n_{\mathrm{He}}} e^{-tk_{\mathrm{ZR}}n_{\mathrm{He}}} e^{-tk_{v=1}n_{\mathrm{He}}} e^{-t/\tau_{\mathrm{spon}}}. \tag{5.49}$$

Eq. 5.49 closely resembles Eq. 5.13, but there are now two additional terms. The first new term includes the effect of a finite collisional quenching coefficient, $k_{v=1}$. The last term contains the effect of spontaneous emission, where we are trying to measure the spontaneous emission lifetime τ_{spon}.

The effective time constant characterizing this decay will be given by

$$\tau_{\mathrm{eff}} = \left[\frac{A}{n_{\mathrm{He}}} + n_{\mathrm{He}}k_{\mathrm{ZR}} + n_{\mathrm{He}}k_{v=1} + \frac{1}{\tau_{\mathrm{spon}}}\right]^{-1}. \tag{5.50}$$

This first two terms come from the diffusion enhancement of the lifetime and the collision-induced Zeeman relaxation, as in Eq. 5.14. Since the magnetic moment, mass, and elastic cross section should be identical for NH($v = 0$) and NH($v = 1$), we can separate the lifetime into parts that are measurable from our NH($v = 0$) data and parts that are not. If we say that these finite hold time effects (which we will call τ_{hold}) correspond to the measured lifetimes of the NH($v = 0$) molecules at the same density and temperature as the NH($v = 1$) molecules, we can rewrite Eq. 5.50 as

$$\tau_{\mathrm{spon}} = \left[\frac{1}{\tau_{\mathrm{eff}}} - \frac{1}{\tau_{\mathrm{hold}}} - n_{\mathrm{He}}k_{v=1}\right]^{-1} \tag{5.51}$$

where τ_{spon} is the spontaneous emission lifetime (what we are trying to measure), τ_{eff} is the measured lifetime of NH($v = 1$) in the trap (open circles in Fig. 5.10), τ_{hold} is the hold time of the trap (closed circles in Fig. 5.10), and the last term contains any collision-induced quenching of the $v = 1$ state.

One thing that is worth mentioning is that the Zeeman relaxation and collisional quenching terms cause the lifetime to scale the same way with buffer-gas density. The consequence of this is that if the collision-induced Zeeman relaxation is significantly different for NH($v = 1$), it will manifest itself as a trap loss mechanism that is indistinguishable from collisional quenching of the $v = 1$ state. Likewise, if the Zeeman relaxation rate is *lower* for NH($v = 1$) than NH($v = 0$), the coefficient $k_{v=1}$ will end up being negative. This does not mean that we are collisionally populating the $v = 1$ state from the $v = 0$ molecules, and we will refer to $k_{v=1}$ as the collisional quenching coefficient even though it can also include differences in Zeeman relaxation rates. Since the vibrational motion is much faster than the helium interaction time, we expect the NH($v = 1$) Zeeman relaxation to be indistinguishable from the NH($v = 0$) rate due to the averaging of vibrational motion.

The data shown in Fig. 5.10 were fit by Eq. 5.51 with $k_{v=1}$ as a free fitting parameter. The result was a vibrational quenching rate coefficient of $k_{v=1} = 1.1 \pm 2.8 \times 10^{-15}$ cm^{3}s^{-1}, which is consistent with zero. We therefore believe that there is not a significant amount of collisional quenching present, and we put an upper limit on the rate coefficient of $k_{v=1} < 3.9 \times 10^{-15}$ cm^{3}s^{-1}.

5.4.3 NH $X^3\Sigma^-(v = 1)$ Lifetime Measurement

In order to measure the spontaneous emission lifetime of NH($v = 1$), we repeatedly measured the lifetime in our trap at the low end of our buffer-gas density range. We trapped NH($v = 1$) 1041 times and recorded the fluorescence collected by our PMT over the course of about 4 hours. The fluorescence traces were averaged directly into

groups of about 40 traces by continuing accumulations on the multi-channel scaler and each of those groups was fit to a single exponential decay using a three-parameter fit.

That collection of 26 lifetimes was used to gather statistics for our systematic error bars. The standard deviation of the sample was 2.6 ms, which we used as the error bars for the data that was fit for vibrational quenching, above. The result was a measured trap lifetime of $\tau_{\text{eff}} = 33.5 \pm 0.5$ ms where the uncertainty is the standard error of our 26 lifetimes.

Using Eq. 5.51 to correct for the finite hold time of the trap (correction is $\Delta\tau = +3.5 \pm 0.1$ ms) and the possible effect of vibrational quenching (systematic uncertainty -0.8 $+2.0$ ms) gives us the final measured value of:

$$\tau_{v=1} = 37.0 \pm 0.5_{\text{stat}} \, {}^{+2.0}_{-0.8}{}^{\text{sys}} \text{ ms.} \tag{5.52}$$

Our collaborator Gerrit Groenenboom at Nijmegen preformed a calculation of the lifetime [33] of 36.99 ms, in excellent agreement with our measured value.

We can re-cast this lifetime into a measurement of the transition dipole moment using Eq. 5.41. Since the dipole transition requires that $\Delta J = \pm 1$, the exact quantum numbers for our transition are $X^3\Sigma^-(J = 1, N = 0, v = 1) \rightarrow X^3\Sigma^-(J = 0, 2, N = 1, v = 0)$. This means that we are making a transition from the rotational ground state to the first rotationally excited state. The frequency for this transition can be taken from literature [153, 148] and is given by $\omega = 3092.88\ \text{cm}^{-1}$. The transition dipole moment we are measuring is

$$\mu_{10} \equiv \langle \phi_{v=1,N=0} \left| \mu(R) \right| \phi_{v=0,N=1} \rangle \tag{5.53}$$

where the $\phi_{v,N}$ are the vibrational wavefunctions (including the rotation of the molecule). This gives us a measured value of

$$|\mu_{10}| = ce\sqrt{\frac{3}{4\alpha\omega^3\tau_{v=1}}} = 0.0540\,^{+0.0009}_{-0.0018}\text{ D.} \tag{5.54}$$

5.4.4 Comparison with Published Values

While both our measured and calculated values for the transition dipole moment agree, they differ significantly from previously published values. Chackerian, Jr. *et al.* [38] have observed the Herman-Wallis effect and combined their spectroscopic data with the 1974 measured value of the static dipole moment of ground-state NH [170]. This results in a measured value for the transition dipole moment of $|\mu_{10}| = 0.0648 \pm 0.008$ D, which they present with a calculated *ab initio* value [38] of $|\mu_{10}| = 0.0594$ D. These transition dipole moments are inconsistent with our result of $|\mu_{10}| = 0.0540\,^{+0.0009}_{-0.0018}$ D. Grevesse *et al.* provide a plot of the calculated dipole moment matrix element (including rotation) vs. N'' that gives a value of $|\mu_{10}| > 0.06$ D for $N'' = 1$ [72]. Cantarella *et al.* use a series of different published potentials and dipole moment functions to calculate dipole matrix elements falling in the range of $0.0528 \leq |\mu_{10}| \leq 0.0618$ D [35]. Das *et al.* calculate and oscillator strength corresponding to $|\mu_{10}| = 0.0526$ D [47].

Our measured lifetime $\tau_{rad,\text{exp.}} = 37.0 \pm 0.5_{\text{stat}}\,^{+2.0}_{-0.8\,\text{sys}}$ ms can also be compared to published values of the Einstein A coefficient using $A_{10}^{-1} = \tau_{rad,10}$. Rosmus and Werner [162] calculate $A_{10}^{-1} = 28.7 \pm 4$ ms, and Dodd *et al.* [56] calculate $A_{10}^{-1} = 19.3$ ms. Both of these calculations neglect rotation, and we find convergence for our calculated value only after inclusion of the large basis and active space described above. Despite these

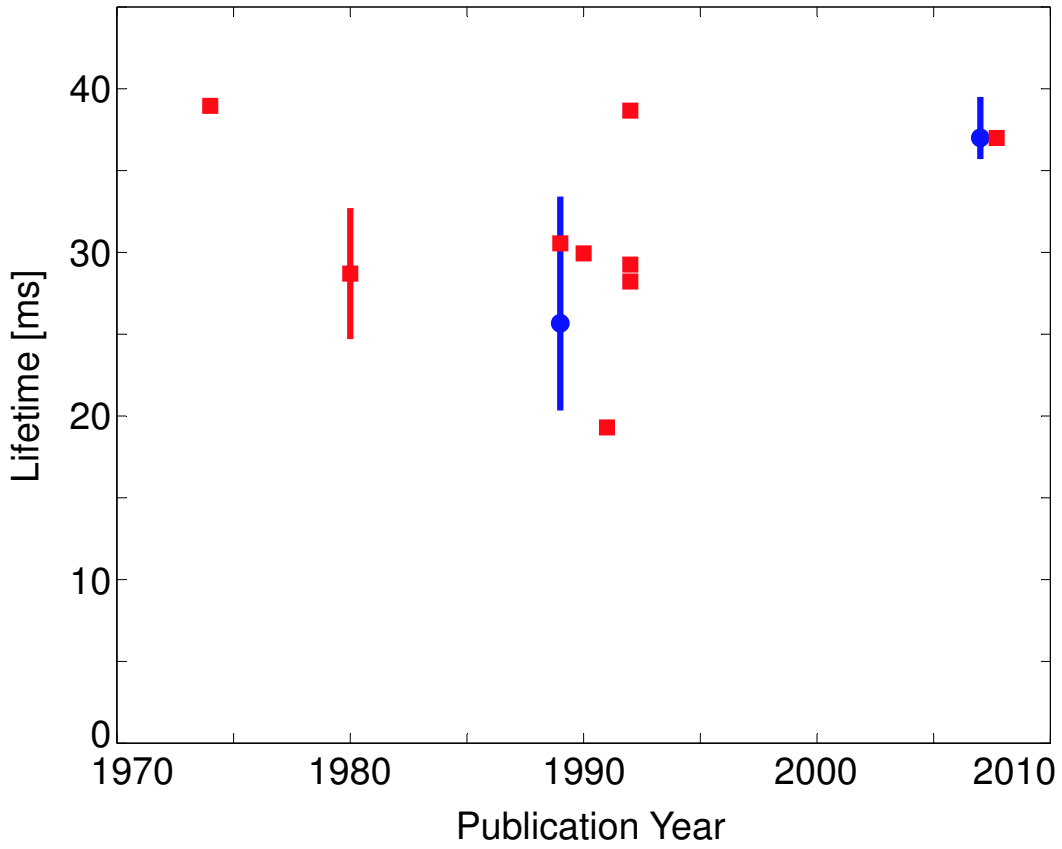

Figure 5.12: Comparison of our measured NH($X^3\Sigma^-, v = 1, N = 0$) radiative lifetime to other published values by publication year. Circles are experiments, squares are calculations. The two points on the right represent our work [33].

discrepancies, our measurement is in agreement with our *ab initio* calculated value and we believe this new value to be the most accurate yet reported. The NH vibrational radiative lifetime τ_{rad} is a vital number for astrophysical studies since the $\Delta v = 1$ transitions of the $X^3\Sigma^-$ state fall in the 3 μm atmospheric transmission window. The absolute line strength of the 0-1 vibration-rotation (V-R) transition (A_{10}) plays a crucial role in determining the nitrogen abundance in cool stars [127, 177, 126, 125], which, in turn, is tied to questions of stellar evolution and internal mixing. The estimated absolute nitrogen abundance of the sun is based on atomic nitrogen (NI)

lines and NH V-R absorption [71]. The lack of precise knowledge of A_{10} has been the dominant source of uncertainty in observed abundances based on V-R lines [72]. Despite their importance, measurements of the NH V-R transition strengths have been particularly lacking [124, 56, 72].

Since previously published values for the transition dipole matrix element are almost all larger than our measured value, it is likely that NH densities that have been inferred from V-R absorption on this line are lower than the actual density of NH radicals. We estimate that current solar nitrogen abundance estimates derived from this transition [72, 5, 71] will require a correction of about 30%.

5.5 Summary

We have been able to demonstrate magnetic trapping of NH molecules using buffer-gas loading. This is the first time that a $^3\Sigma$ molecule has been trapped, and the first time any species has been trapped by loading the buffer-gas cell from a beam. We also preformed the first Zeeman relaxation rate measurements on $^3\Sigma$ molecules, and verified the explanation of that process put forward by Krems and coworkers by changing isotopes. Finally, we were able to trap vibrationally excited molecules and measure the spontaneous emission lifetime of the $X^3\Sigma^-(J = 1, N = 0, v = 1)$ state of NH.

The key technical challenges encountered during this experiment were related to the integration of our buffer gas technique with a molecular beam and the retrofitting of the apparatus with the pulse-tube cooler and high-T_c leads. The former required the construction and testing of an *in vacuuo* trap magnet (the first of its kind for our

group) and the mechanical and thermal connection of the magnet to the liquid helium bath. We also had to solve the problem of helium escaping from the cell orifice, which led us to the Kapton tube and charcoal tube solutions.

Our unusual experiment geometry also led us to design, build, and test a custom ^{3}He refrigerator for our experiment, which was another first for our lab. The apparatus was also the first in our group to utilize a cryocooler and high-T_c leads, which have since been integrated into other experiments as well.

In the next chapter, some possible future directions for the experiment are examined. It is important, however, to note that NH has done quite well. It is my understanding that Gerard Meijer was the first to point out NH as a potential molecule for us, and in very many ways it has been ideal.

Chapter 6

Future Directions

In this final chapter, I explore some of the possible directions for the current apparatus of molecule trapping in general. Thermal isolation of the NH by removing the buffer-gas is the obvious next step, and description of that work will go into Edem Tsikata's thesis, and will not be discussed here. Failed attempts to produce detectable amounts of NH in cold buffer gas using laser ablation are presented, followed by a study of other molecules to pursue for buffer-gas loading using what was learned in this experiment as a guide. Difficulties associated with seeing trap-beam collisions are discussed next, and an analysis of the conditions necessary for laser-cooling molecules is discussed. Last, an investigation of the feasibility of performing a β-decay endpoint energy measurement using buffer-gas loading is introduced.

6.1 Laser Ablation for Imidogen Production

Laser ablation of solids for the production of NH was not pursued in our lab before we preformed the experiments described in this thesis. This was due mainly to the enthusiasm we had for making a beam-loading apparatus, whose generality was estimated to be useful for other types of experiments as well.

Since the collision-induced Zeeman relaxation of NH was sufficiently slow for us to trap it for more than 1 s, we began to wonder if it could be thermally isolated using one of the atomic trapping apparatus in the lab. This would more-or-less require that we find a way to produce NH through laser ablation.

We have since then tried to produce and detect cold NH in a closed buffer-gas cell in a small IR Labs dewar using laser ablation. Detection was balanced laser absorption on $A \leftarrow X$ from the absolute ground state. The solid precursors that were tried were urea, ammonium nitrate, ammonium bromide, and ammonium chloride. For those samples that were in powder form, they were melted into chunks on a piece of copper using a Mapp gas torch under a fume hood.

None of the samples gave us a laser absorption signal. Our sensitivity was about 10^{-3}, with a cell that was about 3 cm on a side. We do not know why we were unable to see any NH, but we can use this to place a limit on the ground state density produced in the cell. The effective absorption cross section can be written as

$$\sigma_{\mathit{eff}} = \frac{\gamma/2\pi}{\Delta\nu_{\mathrm{D}}} \frac{3\lambda^2}{2\pi} \tag{6.1}$$

where $\gamma/s\pi$ is the natural linewidth ($= 1/2\pi\tau$) and $\Delta\nu_{\mathrm{D}}$ is the Doppler width, given by Eq. 3.2. The lifetime of our detection transition is $\tau = 440$ ns [63] and the wavelength

is $\lambda = 335.9$ nm. The Doppler width for NH at 4.2 K is 337 MHz ($= 0.011$ cm^{-1}) and the natural linewidth is 0.36 MHz, which makes the ratio in front 1.1×10^{-3}. The effective absorption cross section, therefore, is $\sigma_{\mathit{eff}} = 5.8 \times 10^{-13}$ cm^2.

To put an upper limit on the ground state NH density in the cell, we can use Beer's Law (Eq. 4.1) to write

$$1 - 10^{-3} < e^{-\sigma_{\mathit{eff}} n_{\mathrm{NH}} l}. \tag{6.2}$$

The laser was passing through the 3.2 cm cell 3 times, corresponding to $l = 9.6$ cm. This gives us a limit of $n_{\mathrm{NH}} < 1.8 \times 10^8$ cm^{-3}.

6.2 Other Molecules

Figure 6.1 lists relevant properties of other known $^3\Sigma$ ground-state molecules. The column labeled "BGTF" is intended to be a "Buffer-gas Trapping Factor" indicating how much worse each molecule is than NH:

$$\mathrm{BGTF} \equiv \frac{\lambda_{\mathrm{SS}}^2 / B_e^2}{\lambda_{\mathrm{SS}}^2[\mathrm{NH}] / B_e^2[\mathrm{NH}]}. \tag{6.3}$$

A large BGTF indicates an increased probability of collision-induced Zeeman relaxation (the BGTF for NH is defined to be 1). NH has by far the lowest BGTF of the $^3\Sigma$ ground state molecules. The next best chemically distinct molecule is PH, which should be about 22 times worse than NH, followed by CaC, NF and O_2.

Table 6.2 lists some metastable states that may work as well. Both of these molecules will be discussed in more detail below.

Table 6.3 shows diatomic molecules with Σ ground states and higher-than-triplet

Table 6.1: Molecular properties for $^3\Sigma$ ground state neutral molecules.

Molecule	B_e [cm^{-1}]	λ_{ss} [cm^{-1}]	BGTF	Notes
AsF	0.37			[143]
AsH	7.20	58.9	22000	[55]
B_2	1.22			[28]
BiH	5.14	2458	7×10^7	[83, 187]
CaC	0.34	0.11	35	[77]
LiN	(1.0)			[22]
LiP	(0.54)			[22]
NBr	0.45	11.6	2×10^5	[167]
NCl	0.65	1.88	2800	[204]
NF	1.21	1.21	327	[94]
NH	16.7	0.920	$\equiv$1	[153]
ND	8.91	0.919	3.51	[151]
NT	6.3	0.919	7	(predicted)
NI	0.34	43.8	5×10^6	[168]
NiO	0.51	25.1	8×10^5	[98]
$^{16}O_2$	1.44	1.98	620	[102]
PBr	0.16			[156]
PCl	0.25	4.3	97000	[105]
PF	0.57	2.95	8800	[203]
PH	8.54	2.21	22	[151]
ReN	0.48			[152, 36]
SO	0.72	5.3	4800	[21]
S_2	0.30	11.8	5×10^5	[146]
SbF	0.28			[149]
SbH	5.8	333	10^6	[187]
SeO	0.46	86.6	10^5	[12]
SeS	0.18			[149]
Se_2	0.09			[84]
Si_2	0.24			[149]
Te_2	0.04			[149]
WO	0.42	514	5×10^8	[154]

Table 6.2: Molecular properties for long-lived metastable Σ state neutral molecules.

Molecule	State	lifetime	B_e [cm^{-1}]	λ_{ss} [cm^{-1}]	BGTF	Notes
N_2^*	$A^3\Sigma_u^+$	$\approx$1 s	1.45	1.32	272	[164]
CH^*	$a^4\Sigma^-$	12 s	15.0	0.093	0.013	[87, 142]

Table 6.3: Molecular properties for highly magnetic Σ ground state neutral diatomic molecules. Rotational constants in parentheses are calculated from published equilibrium internuclear separations.

Molecule	State	B_e [cm^{-1}]	λ_{ss} [cm^{-1}]	BGTF	Notes
AlC	$^4\Sigma$	0.53	$\pm$0.0062	0.045	[26]
BC	$^4\Sigma$	1.32	0.028	0.15	[64]
CrN	$^4\Sigma$	0.62	2.6	5700	[172]
KC	$^4\Sigma$	0.29	0.56	1280	[201]
LiC	$^4\Sigma$	(1.1)			[157]
LiSi	$^4\Sigma$	(0.53)			[22]
MoN	$^4\Sigma$	0.52	21.4	6×10^5	[182]
NaC	$^4\Sigma$	0.29	0.0058	0.14	[173]
NbO	$^4\Sigma$	0.43	15.6	4×10^5	[1]
RuH	$^4\Sigma$	(6.5)			[8]
VO	$^4\Sigma$	0.55	2.0	4300	[41]
WN	$^4\Sigma$	0.47	220	7×10^7	[150]
ReH	$^5\Sigma$	(6.3)			(may be $^7\Sigma$) [37, 46]
CrCl	$^6\Sigma$	0.17	0.27	834	[107]
CrF	$^6\Sigma$	0.40	0.54	662	[107]
CrH	$^6\Sigma$	6.2	0.23	0.45	[31]
MnO	$^6\Sigma$	0.5	0.57	430	[99]
MnS	$^6\Sigma$	0.2	0.35	1050	[14, 185]
MoH	$^6\Sigma$	(6.0)			[9]
WH	$^6\Sigma$	5.21			[136, 67]
MnCl	$^7\Sigma$	0.16	0.037	18	[14]
MnF	$^7\Sigma$	0.35	-0.0046	0.054	[129, 174]
MnH	$^7\Sigma$	5.69	-0.004	0.00016	[149, 68]
GdO	$^9\Sigma$	0.36	-0.10	25	[104]

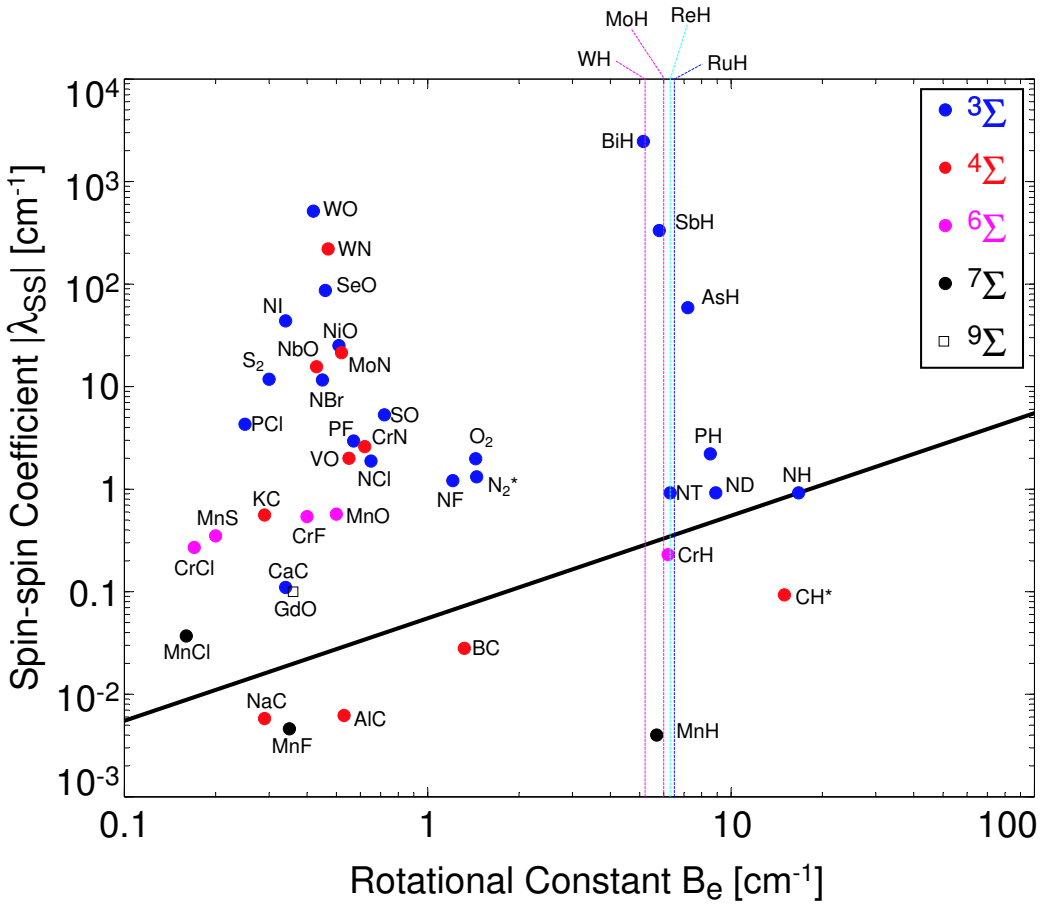

Figure 6.1: Spin-spin coefficient vs rotational constant for Σ state molecules of triplet and higher spin multiplicity. The diagonal line is constant BGTF (see Eq. 6.3). Molecules above the line will likely spin relax faster than NH, those below will spin relax more slowly (modulo interaction anisotropy).

spin multiplicity. Much of the data for this table was first organized by the Berlin group [6].

All of the fairly magnetic ($2\mu_B$ and up) Σ state diatomic molecules for which B_e and λ_{ss} could be found are shown in Fig. 6.1. The BGTF for NH is represented by the solid black line. If the anisotropy of the helium interaction is the same for all molecules (it is not, but this is the data we do have), those lying above the line will spin relax more quickly than NH, those below will spin relax more slowly. Furthermore, in order

to make a deep magnetic trap, the level crossing between the LFS Zeeman level of the ground state and the HFS of the rotationally excited state must occur at more than a few Tesla. This limits heteronuclear molecules to $B_e > 3$ cm^{-1} and homonuclear molecules to $B_e > 1$cm^{-1}. If we cut off molecules at BGTF=40, that leaves O_2, N_2^*, PH, imidogen, CrH, CH^* and MnH.

6.2.1 O_2

At a BGTF of 620, molecular oxygen will likely spin relax in less than 10 ms. Nonetheless, the possibility of capillary filling makes it an interesting possibility because the density could be extremely high. The detection, however, is very difficult. The following data are from Krupenie [122] unless otherwise noted.

The only dipole-allowed transition from the ground state is the *Schumann-Runge system* ($B^3\Sigma_u^- \leftrightarrow X^3\Sigma_g^-$). The (0,0) line is at 202.5 nm and has an f-value of 3.45×10^{-10} (radiative lifetime of 1.8 s) while the (19,0) line is at 175 nm with an f-value of 1.44×10^{-5} (radiative lifetime of 32 μs). The problem with using this transition for fluorescence is that the excited state predissociates due to the presence of four unbound potentials ($2^3\Sigma_u^+$, $^5\Pi_u$, $^3\Pi_u$, and $^1\Pi_u$) that cross the B state. The predissociation widths are of order $0.1 - 3$ cm^{-1} [103], corresponding to lifetimes of less than 1 ns. The fluorescence yield, therefore, should be fairly small. Furthermore, the line broadening from the predissociation will reduce the excitation probability by a narrow-band source.

The $a^1\Delta_g \leftrightarrow X^3\Sigma_g^-$ *atmospheric IR system* starts at 1268 nm for the (0,0) transition with a lifetime of about 1 hr.

The $b^1\Sigma_g^+ \leftrightarrow X^3\Sigma_g^-$ *red atmospheric system* has its (0,0) transition at 762 nm with a Franck-Condon factor of 0.93. The (0,0) band is still weak, however, with a lifetime of 11.8 s.

The *Herzberg I system* ($A^3\Sigma_u^+ \leftrightarrow X^3\Sigma_g^-$) starts with (0,0) at 285 nm with a lifetime of 5000 s. The (11,0) transition at 243 nm has a higher Franck-Condon factor (1.7×10^{-3} compared to 1.8×10^{-6} for the (0,0) transition) and a transition dipole moment of $\mu_{11,0} = 5.5 \times 10^{-5} e a_o$, which corresponds to a lifetime of 2.4 s.

The *Herzberg II system* ($c^1\Sigma_u^- \leftrightarrow X^3\Sigma_g^-$) is predicted to have a (0,0) transition at 306 nm and has a lifetime of around 3 hrs.

The *Herzberg III system* ($C^3\Delta_u \leftrightarrow X^3\Sigma_g^-$) has a (6,0) band at 258 nm and a (5-0) band at 262 nm with a lifetime of more than a day.

The longest wavelength ionization system from the ground state is the $O_2^+ X^2\Pi_g \leftarrow O_2 X^3\Sigma_g^-$ system starting at 102.7 nm for the (0,0). A pulsed dye laser at 616 nm could be easily doubled to yield 308 nm light for a three-photon transition.

6.2.2 N_2^*

The nice thing about triplet N_2^* is that there is a transition in the first positive system at 687.5 nm: $B^3\Pi_g(v = 3) \leftrightarrow A^3\Sigma_u^+(v = 0)$ with a Franck-Condon factor of 0.034 [164, 135]. The lifetime of the excited state is 8 μs, which makes this a fairly weak transition. The rate coefficient for quenching by room-temperature He has been measured to be less than 10^{-17} cm^{3}s^{-1} [32]. Even so, the collision-induced Zeeman relaxation should be almost 300 times worse than NH, so there is not too much hope for a long lifetime in the trap.

The lifetime of the A metastable state is of order 1s, and a precision time-domain measurement of this lifetime may be possible in the trap.

6.2.3 PH

The most straightforward way to produce PH is by discharging phosphine (PH_3) in analogy to how we make NH from ammonia. Phosphine, however, is toxic and flammable. Furthermore, even if a better precursor could be found, the $A \leftrightarrow X$ transition has a lifetime of 440 μs [149], which is roughly 10^3 times weaker than the analogous transition in NH. Despite this, if the helium interaction anisotropy is the same as NH, PH should be trappable for 30 ms or more.

6.2.4 CH^*

Metastable CH should be 77 times less likely to spin relax than NH. Furthermore, it will have $3\mu_B$ magnetic moment. The problem with a-state CH is detection. The state was only recently detected by doing rotational spectroscopy at 333 μm using laser magnetic resonance [142]. The detection is made difficult by the lack of another bound state with spin multiplicity of 4 (the $^4\Pi$ state is unbound). The most likely nonionizing detection would probably be to drive the spin-forbidden $B^2\Sigma^- \leftarrow a^4\Sigma^-$ transition to get a 389 nm fluorescence photon from the $B^2\Sigma^- \rightarrow X^2\Pi$ decay. This excitation transition has not been observed, but spectroscopic parameter calculations [114] suggest it will be somewhere around 498 nm. If the spectroscopy could be worked out beforehand and the helium quench rate is low, CH^* should work nicely for buffer-gas loading.

6.2.5 CrH

Since CrH has a 5 μ_B magnetic moment and a BGTF of 0.45, it is a strong candidate for buffer-gas loading. The Berlin group has already investigated this molecule and details can be found in the upcoming thesis of Micheal Stoll. Detection can be done on the $A^6\Sigma^+ \leftrightarrow X^6\Sigma^+$ transition, where the (0,0) and (1,0) lines are at 866 nm and 767 nm, respectively. Despite the fact that this transition is Σ to Σ of the same spin multiplicity, there is significant magnetic broadening of this transition [39] of order 1 μ_B. The transition is also of intermediate strength, with a lifetime of 939 ns for the $A^6\Sigma^+(v = 0)$ state [175]. Off-diagonal excitation could be accomplished on the (1,0) with a 767 nm Ti:sapphire laser and the resulting 866 nm (1,1) fluorescence could be detected through a band-pass filter. The work of Kleman and Uhler [115] suggests that the (1,0) transition is about 40% as strong as the (0,0).

6.2.6 MnH

MnH looks like the strongest candidate for buffer-gas loading. The Berlin group has already done work with it similar to their CrH work. The BGTF is more than 6000 times better than NH, but the spin-rotation parameter is larger than the spin-spin coefficient ($\gamma = 0.032$ cm^{-1}) and therefore may dominate the Zeeman relaxation [1].

Detection can be accomplished on the $A^7\Pi \leftrightarrow X^7\Sigma^+$ transition. The (0,0) line is at 568 nm and has a radiative lifetime to $X^7\Sigma^+(v'' = 0)$ of $A_{0,0}^{-1} = 110$ ns. The $A^7\Pi(v = 0)$ state will emit back to $v'' = 0$ with 85% probability but will also emit a

[1] For comparison, for CaH $\gamma = 0.044$ cm^{-1} [11]

Table 6.4: Molecular properties for Σ ground state neutral polyatomic molecules.

Molecule	State	B_e [cm^{-1}]	λ_{ss}	BGTF	Notes
KCH	$^3\Sigma$	0.24	0.27	398	[202]
Li_2C	$^3\Sigma_g^-$	(0.72)			[138]
NaCH	$^3\Sigma$	0.38	0.30	213	[202]
$MnBr_2$	$^6\Sigma$				[14]
$MnCl_2$	$^6\Sigma$				[14]
MnF_2	$^6\Sigma_g$				[53]
MnI_2	$^6\Sigma$				[14]

624 nm photon 13% of the time [128] by decaying to the $v'' = 1$ state. CW excitation with Rhodamine 6G should therefore be sufficient.

6.3 Collisions of a Beam with the Trap

The fact that the trap magnet and cell are suspended in vacuum (instead of submerged in liquid) allows us to also consider the possibility of sending tunable-velocity a beam of atoms or molecules through the trap. If thermal isolation of the trapped sample can be achieved, there is the possibility to observe collisions between the trapped sample and an intense beam. If the velocity of the beam is tunable, one could consider tracing out collision resonances using this method. Recently, Tim Softley and coworkers have reported reactive cold collisions between a beam of molecules and trapped ions [200].

To determine the feasibility of this proposal, we will start with the trapped density we have achieved with NH. We have trapped about 10^8 molecules at a density of 10^8 cm^{-3} in a trap that is roughly 1 cm in size.

The types of collisions that could be observed include Zeeman relaxation, vibra-

tionally and rotationally inelastic collisions, chemical reactions, any sort of state-changing collisions and elastic collisions. For the moment, we will consider the example of rotational excitation. If the incoming beam is atomic, there will be a momentum kick imparted to the collisionally rotationally-excited NH that will kick it out of the trap. If, however, the incoming beam consists of molecules that have a large fraction of the energy necessary for rotational excitation stored internally (*e.g* ^{15}NH(N=1)), the rotational excitation of the trapped sample can be detected by looking for the appearance of NH($N = 1$) in the trap.

If we assume that in order to observe these collisions, we require that the whole trapped sample be excited in 10 s, we can calculate how intense the beam must be. Assuming a rotational transfer cross section of 10^{-16} cm^2 means that the incidence rate of beam molecules onto the 1 cm^2 target must exceed 10^{15} s^{-1}. This shows the difficulty of such schemes–the detection efficiency is so low that collision products must be accumulated at a tremendous rate in order to be detected. Despite this, the flux calculated here may be possible. A buffer-gas beam source operating at 1 sccm of helium would need a 1/100 dilution of molecules to achieve this number. Any type of collision that can be detected more sensitively will reduce these constraints.

6.4 Laser Cooling of Molecules

It has been noted [89, 161] that NH is a good candidate for laser cooling. In this section I will present considerations that apply to laser cooling of molecules and examine the feasibility of performing laser cooling on molecules.

6.4.1 Vibrational State Leakage

The fundamental limitation that prevents molecules from being easily laser coolable is not rotational state leakage. Because of rigid angular-momentum selection rules, it is possible to close an electronic transition rotationally with enough lasers. For instance, for NH one may consider using the ${}^{R}P_{31}(J'' = 1)$ line for laser cooling (see Fig. 3.1.1), which would require only one rotational repumper on the $P_3(J'' = 1)$ line about 100 cm^{-1} to the red of the main cooling line.

The vibrational state leakage, on the other hand, cannot be rigorously closed. Selection rules do not forbid transitions between vibrational levels of an excited electronic state and any of the vibrational states (or continuum states) of the lower lying electronic level in a dipole-allowed transition system. If cooling is being performed on the $(v, v'') = (0,0)$ transition, state leakage can occur via (0,1) spontaneous emission. Adding a (0,1) repump laser will plug this hole, but not only must it also be rotationally closed, it must also be fairly strong to account for the (hopefully) comparatively weak (0,1) transition. State leakage is still allowed, however, via (0,2) fluorescence. From this it becomes clear that closing the transition absolutely will require as many lasers as vibrational levels in the ground electronic state times the number of rotational lines being pumped. If the excited electronic state lies above the dissociation threshold of the ground electronic state, it is also to have bound-to-unbound transitions to the continuum.

One way to mitigate this issue is to choose a molecule whose *likelihood* of leakage is low enough to permit cooling of some finite duration. This information is typically available as a calculated Franck-Condon factor, described below. Many of the aspects

of this analysis will be similar to Section 5.4.1.

The probability of emission $P_{vv''}$ from some state $A(v)$ to $X(v'')$ will be proportional to the square of the transition dipole matrix element for the transition:

$$P_{vv''} \propto \left|\langle A, v \left|\boldsymbol{\mu}\right| X, v''\rangle\right|^2 . \tag{6.4}$$

We can use the dipole moment *operator* $\boldsymbol{\mu}$ from Eq. 5.43 to construct the dipole moment *function* $\mu(R)$ by integrating over the electronic wavefunctions:

$$\begin{aligned} \mu(R) &\equiv \langle A \left|\boldsymbol{\mu}\right| X\rangle & (6.5)\\ &= e\sum_i \int \mathrm{d}^3\mathbf{r}_i \; \psi_A(\mathbf{r}_i, R)\; \mathbf{r}_i \; \psi_X(\mathbf{r}_i, R) & (6.6) \end{aligned}$$

where R is the internuclear separation. If the electric dipole moment function $\mu(R)$ is a function of the electronic states and is independent of the vibrational state (coordinate R), we can factor this expression as we did in Eq. 5.46

$$P_{vv''} \propto \left|\mu \left\langle v \right| v''\right\rangle\right|^2 . \tag{6.7}$$

That last term is called the Franck-Condon factor ($q_{vv''} \equiv \left|\left\langle v \right| v''\right\rangle\right|^2$ subject to $\Sigma q_{v,v_i} = 1$) and is nonzero as long as A and X are different electronic states. The vibrational state leakage to $v'' = 1$, then, is proportional to $q_{0,1}$, the Franck-Condon factor.

When we look at NH, however, we find that $q_{0,0} = 0.99989$ [206]. This implies that the vibrational leakage only happens once every 9000 photon cycles. If this were true, NH would not even need a vibrational repumper for most laser-cooling applications.

However, this is not the end of the story. As was the case with vibrational spontaneous emission within a single electronic state, the dependence of the transition dipole moment on the internuclear spacing must be included. Any correction larger than

1 part in 9000 becomes important on this level due to the incredibly large Franck-Condon factor. The Franck-Condon factor, then, becomes less meaningful than the whole transition dipole moment (with dependence on internuclear separation R included):

$$P_{vv''} \propto |\langle v\,|\mu(R)|\,v''\rangle|^2 = \left|\int \mathrm{d}R\;\phi_v^A(R)\;\mu(R)\;\phi_{v''}^X(R)\right|^2 \tag{6.8}$$

where the ϕ are the vibrational wavefunctions.

The ratio $P_{0,1}/P_{0,0}$ is calculated by Yarkony to be 1.09×10^{-2} [206], corresponding to a vibrational leakage once every 92 photon cycles. Fairchild *et al.* calculate 6.2×10^{-3} [63], which implies leakage every 161 photons. Lents measures a ratio corresponding to 178 cycles per leakage [132] and Anderson and Crosley measure a ratio corresponding to 149 ± 27 photons before leakage [2]. For our purposes we will assume a vibrational leakage to $v'' = 1$ happens once every 150 cycles. If we are near saturation, this corresponds to 70 μs.

If we were to repump on the (0,1) line at 375 nm, the laser cooling could be extended to 5578 photons [206], which corresponds to 2.5 ms. 375 nm laser light could be produced by frequency doubling a dye laser at 750 nm or using a diode such as Nichia NDU1113E, which provides 20 mW at 375 nm. The fact that this transition is so weak makes it tempting to use a pulsed dye laser, but if the NH is being cycled once every 450 ns, the rep rate necessary would be more than 14 kHz. In fact, since the vibrational spontaneous emission lifetime for $v'' = 1$ is 37 ms, having a pulsed vibrational repump laser with a repetition rate slower than about 50 Hz will still be lossy for any cooling cycle time.

Table 6.5: CaH state decay probabilities on $A \leftrightarrow X$.

v'' \ v	0	1	2
0	0.9828	0.0129	(< 0.0004)
1	0.0168	0.9541	0.0244
2	0.0003	0.0317	0.0926
3	(< 0.0001)	0.0014	0.0456

6.4.2 Repumping Through Spontaneous Emission

In general, the method of using repump lasers on the off-diagonal transitions suffers from the complexity involved with finding such lasers. They are often 50-100 nm more red than the main cooling laser, and may require the use of multiple different laser technologies. Here an alternative approach is presented and analyzed that utilizes lasers that are less than 5 nm apart.

Instead of repumping the $v'' = 1$ molecules by driving the (0,1) transition, cooling could also be accomplished on the (1,1) transition. Some of the excited $v = 1$ molecules will decay to the $v'' = 0$ ground state, effectively accomplishing the repumping. Furthermore, those that decay on the (1,2) line have the possibility of being repumped by a (2,2) cooling laser, and so on.

To examine the feasibility of this scheme, we will use CaH as an example since it may be possible to use diode lasers (*e.g.* Toptica LD-0690-0035-1) for cooling. The $A^2\Pi_r \leftrightarrow X^2\Sigma^+$ transition has a (0,0) line at 693.0 nm. Table 6.5 shows the fractional state leakage calculated from [131, 15].

We can define a leakage rate due to off-diagonal spontaneous emission as the reciprocal of the number of cycles required to deplete the initial population to $1/e$ of

Table 6.6: CaH state leakage rates on $A \leftrightarrow X$, in units of number of $A \leftrightarrow X$ optical cycles. Diagonal entries are the total leak rate from that state.

${v''}^{v}$	0	1	2
0	$1/\sum\Gamma_{0i} = 57.5$	$1/\Gamma_{10} = 77.3$	$1/\Gamma_{20} > 2811$
1	$1/\Gamma_{01} = 59.2$	$1/\sum\Gamma_{1i} = 21.5$	$1/\Gamma 21 = 40.5$
2	$1/\Gamma_{02} = 3003$	$1/\Gamma_{12} = 31.0$	$1/\sum\Gamma_{2i} = 13.4$
3	$1/\Gamma_{03} > 7186$	$a/\Gamma_{13} = 736$	$1/\Gamma_{23} = 21.4$

its initial value by leakage only to that state:

$$\Gamma_{ik} \equiv -\ln(1 - q_{ik}) \tag{6.9}$$

where q_{ik} is the fractional leakage from $v = i$ into $v'' = k$ (normally given by the Franck-Condon factor). The q_{ik} are given in Table 6.5 and the leak rates are given in Table 6.6.

With only the (0,0) transition being driven, leakage occurs every 58 cycles. If we were to repump on (0,1) at 760 nm, this would be extended to 3003 cycles. To compare this to the case where both (0,0) and (1,1) are being driven, we can model the $v'' = 0, 1$ state populations (N_0 and N_1) as follows:

$$\dot{N}_0(n) = -N_0(n)(\Gamma_{01} + \Gamma_{02}) + N_1(n)\Gamma_{10} \tag{6.10}$$

$$\dot{N}_1(n) = -N_1(n)(\Gamma_{10} + \Gamma_{12}) + N_0(n)\Gamma_{01} \tag{6.11}$$

where n is the number of photon cycles and the dot represents $\mathrm{d}/\mathrm{d}n$. We can solve this system of linear homogeneous differential equations by rewriting them in matrix form:

$$\frac{\mathrm{d}}{\mathrm{d}n}\begin{pmatrix} N_0 \\ N_1 \end{pmatrix} = \begin{pmatrix} -\Gamma_{01} - \Gamma_{02} & \Gamma_{10} \\ \Gamma_{01} & -\Gamma_{10} - \Gamma_{12} \end{pmatrix}\begin{pmatrix} N_0 \\ N_1 \end{pmatrix}. \tag{6.12}$$

The resulting decay rates are now given simply by the eigenvalues of the matrix above.

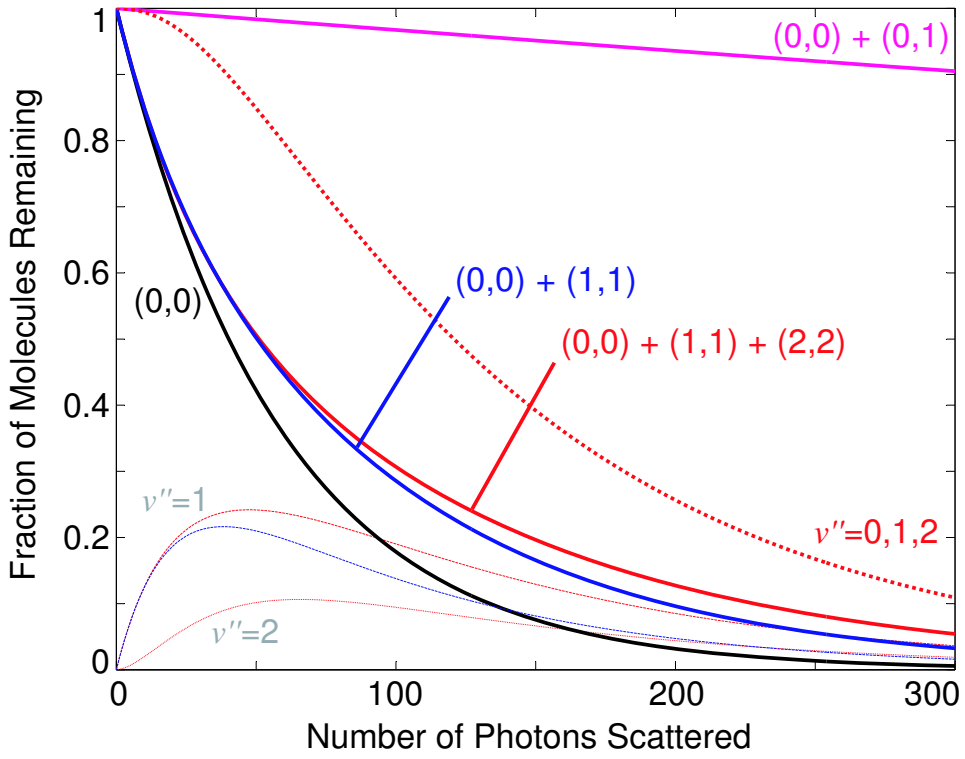

Figure 6.2: Fraction of NH molecules remaining vs. number of photon cycles for four different laser cooling schemes. The black curve shows cooling on the (0,0) band only. The magenta curve adds the effect of a (0,1) repump laser. The blue curve shows cooling on (0,0) and (1,1), and the red curve represents cooling on (0,0), (1,1) and (2,2). Solid bold curves are the $v'' = 0$ ground state population. The dashed bold red curve shows the sum of populations in the $v'' = 0, 1, 2$ levels for the three-laser scheme.

The results of this analysis are shown in Fig. 6.2. The solid curves are the populations of the $v'' = 0$ ground state as a function of photon cycle number. The black curve represents cooling on the (0,0) with no repump laser, while the magenta curve shows the same with a (0,1) repumper. The blue trace shows the effect of adding a (1,1) laser, while the red trace has a (1,1) and a (2,2) cooling laser. Clearly, this scheme does not buy much for CaH compared to having a vibrational repump laser.

6.4.3 Number of Photons

Each photon absorbed from a molasses takes $\Delta p = \hbar k$ of momentum from the molecule. If we start at an initial temperature T, the number of photon cycles necessary to completely cool the molecule is given by

$$N_p = \frac{\sqrt{3 k_{\mathrm{B}} T m}}{\hbar k}. \tag{6.13}$$

For NH starting from room temperature, this is 8952 photons. If we start from 4.2 K, it will take 1059 photons. Starting from 500 mK brings this down dramatically to 366 photons. The light mass and relatively large amount of momentum per photon make NH a fairly good candidate for laser manipulation.. For CaH, the longer wavelength and heavier mass result in $N_p = 1241$ for a starting temperature of 500 mK, which is still far below the 3003 photons cycles that can be achieved with a (0,1) repump.

6.4.4 Rotational Leakage

The rotational state leakage has to this point been ignored because it is possible (in principle) to completely plug the leaks with enough lasers. For instance, two lasers could be used to cool on the $P_3(1)$ and ${}^{R}P_{31}(1)$ lines for each vibrational state for NH. A similar scheme has been proposed for CaH by Di Rosa [161]. The detuning required for this rotational repump laser is such that it may be possible for some species with small rotational splittings to use an EOM to create the repump light. This is not possible for the 3 THz frequency difference in NH.

6.4.5 Hyperfine Repumping

The number of hyperfine levels in the ground state should be minimized through isotopic choices to reduce the number of laser frequencies required. For the case of NH, this means ^{15}NH should be used. For total nuclear spin $T = 1$ and the rotational ground state of NH ($J'' = 1$), $F'' = 2, 1, 0$ are possible. For $T = 0$, we have $F'' = 1$, giving us 4 hyperfine states. The same is true of the $J = 1$ rotationally excited state from the previous section. The excited state is $J = 0$, so we only have two hyperfine states there, $F = 1, 0$.

Ideally, the total angular momentum quantum number F of the excited state is larger than the stretched level of the ground state so that the stretch transition can be used to avoid having to repump hyperfine levels. Unfortunately, the ease of creating hyperfine repump lasers compared to rotational repump lasers makes this impossible since we wish to have an excited state with $J = J'' - 1$ to reduce the number of rotational repump lasers. Nonetheless, if we choose to cool using the $F = 0$ level of the excited state, decay to $F'' = 2$ is forbidden and we only need to generate three laser frequencies for each rotational line.

The hyperfine interaction will split the transition over about 600 MHz. Creation of the hyperfine repump beams should be possible using commercial EOMs.

6.4.6 Conclusion

Laser cooling of NH will require two frequency-stabilized dye lasers and two resonant doubling cavities for the 336 nm (0,0) transition. There will also be two 375 nm diode lasers for the (0,1) vibrational repump. Each of these four lasers will be split

into three different frequency components using 12 total EOMs (it may be possible to share some of these between vibrational lines). This is the minimum equipment required for cooling from 4.2 K, and if we start from 300K, fully 20% of the molecules should be cooled to the ground state.

6.5 β-decay Neutrino Mass Measurement with Tritium

We have demonstrated the ability to trap both NH and ND, which suggests that tritiated imidogen (NT) should also be possible. Table 6.1 shows that the BGTF for NT is only 7, making it about 2 times worse than ND from the perspective of spin relaxation. This suggests that it may be possible to trap molecules with tritium. This section discusses the feasibility of using trapped, tritiated molecules or tritium atoms to measure the electron anti-neutrino rest mass.

Neutron beta decay happens when a neutron decays into a proton, an electron (the β-particle) and an electron anti-neutrino $\bar{\nu}$. In the case of the tritium nucleus, the decay results in a ^{3}He nucleus. For a neutral tritium atom, we have the reaction

$$\mathrm{T} \rightarrow {}^3\mathrm{He}^+ + \mathrm{e} + \bar{\nu}. \tag{6.14}$$

This process releases 18.591 keV of energy and happens with a half-life of 12.32 years [13], corresponding to a $1/e$ lifetime of $\tau = 17.77$ a.

If the neutrino has no mass, then when we measure the total energy of the ^{3}He ion and the electron we will get values for all energies less than 18.591 keV. A measured energy of 18.591 keV would correspond to a neutrino with zero kinetic energy and (of

course) zero mass.

If, on the other hand, the neutrino has mass, the distribution of energies will stop early at $E = 18.591$ keV $- m_\nu c^2$ and we will never measure a total energy greater than this value. In fact, the distribution will be truncated rather sharply near the end and the difference between 18.591 keV and where the measured distribution ends will be the mass of the electron anti-neutrino.

While it is possible that the neutrino has some mass, current measurements of the neutrino mass seem to indicate that it is no more than 2 eV [205].

There are two types of tritium measurements that have been used to try to measure a nonzero neutrino mass. The first method had been to use condensed matter samples containing tritium [24, 108, 91, 195]. The problem with this type of measurement is the lack of knowledge of how much energy has been left in the material, either through recoil effects or deposition by the electron on its way out. The second method uses circulating molecular tritium gas and differential pumping with electron collection to measure the spectrum of the electrons [160, 179]. The resulting energy of the $^3He^+$ ion remains unknown here as well, and there is a tremendous amount of radioactive material in use for such experiments. The escaping electron can also deposit energy into the T_2 gas before it gets to the differentially-pumped region that houses the spectrometer.

One way to measure the energy distribution would be to trap atomic tritium and set up ion optics to measure the energy of the $^3He^+$ ion and the electron. Unfortunately, the technique that was used to trap atomic hydrogen [86] does not work for tritium. It may be possible to use buffer-gas loading to trap atomic tritium, but

the optical transitions in the hydrogen isotopes are far in the UV, which makes trap diagnostics difficult. Nonetheless, this possibility may still be feasible.

Another possibility would be to trap some molecule that has tritium as one of its atoms. The molecular structure could be used to make the tritium more easily trapped and detected. If NT were used, the 2 μ_{B} magnetic moment would make it easier to trap than atomic tritium and the optical detection at 336 nm is essentially already in place in our lab. The decay would be

$$\mathrm{NT} \rightarrow {}^{3}\mathrm{HeN}^{+} + \mathrm{e} + \bar{\nu} \tag{6.15}$$

where the ${}^{3}\mathrm{HeN}^{+}$ molecular ion would either be in a molecular state of discrete internal energy or in a dissociated or doubly-ionized state. In the case of T_2, there is roughly 85% probability of the resulting ion being in a singly-ionized molecular state [62].

The probability of an interesting β-decay during the experiment will determine how many tritium atoms must be trapped. The fraction of decay events that disappear for a 10 eV neutrino mass is 2×10^{-10} and scales as m_{ν}^{3} [119], so for a 2 eV neutrino mass limit, the fraction of decays that are "interesting decays" is something like 1.6×10^{-12}. A single deuterium atom will emit 1.78×10^{-9} betas per second, and therefore 2.86×10^{-21} interesting decays per second. If the total number of trapped NT molecules were an astronomical 10^{14}, there would be an interesting decay every 40 days. Stopping at 10 eV brings this up to every 10 hours.

Bibliography

[1] A. G. Adam, Y. Azuma, J. A. Barry, A. J. Merer, U. Sassenberg, J. O. Schröder, G. Cheval, and J. L. Féménias. Hyperfine structure in high spin multiplicity electronic states: Analysis of the $B^4\Pi - X^4\Sigma^-$ transition of gaseous nbo. *J. Chem. Phys.*, 100(9):6240–6262, 1994.

[2] William R. Anderson and David R. Crosley. Laser-excited fluorescence in the A-X system of NH. *Chem. Phys. Lett.*, 62(2):275–278, 1979.

[3] A. André, D. DeMille, J. M. Doyle, M. D. Lukin, S. E. Maxwell, P. Rabl, R. J. Schoelkopf, and P. Zoller. A coherent all-electrical interface between polar molecules and mesoscopic superconducting resonators. *Nature Physics*, 2:636, 2006.

[4] George Arfken. *Mathematical Methods for Physicists*. Academic Press, Inc., 3 edition, 1985.

[5] Martin Asplund, Nicolas Grevesse, and A. Jacques Sauval. The solar chemical composition. In F. N. Bash and T. G. Barnes, editors, *Cosmic Abundances as Records of Stellar Evolution and Nucleosynthesis*, volume XXX, 2005. astro-ph/0410214.

[6] Joost M. Bakker, Michael Stoll, Dennis R. Weise, Oliver Vogelsang, Gerard Meijer, and Achim Peters. Magnetic trapping of buffer-gas-cooled chromium atoms and prospects for the extension to paramagnetic molecules. *J. Phys. B*, 39:S1111, 2006.

[7] N. Balakrishnan, G. C. Groenenboom, R. V. Krems, and A. Dalgarno. The He-CaH($^2\Sigma^+$) interaction. II. collisions at cold and ultracold temperatures. *J. Chem. Phys.*, 118(16):7386–7393, 2003.

[8] K. Balasubramanian. The low-lying states of the second-row transition metal hydrides (YH-CdH). *J. Chem. Phys.*, 93(11):8061–8072, 1990.

[9] K. Balasubramanian and Jungqing Li. Spectroscopic properties and potential energy curves of MoH and MoH^+. *J. Phys. Chem.*, 94:4415–4419, 1990.

[10] M. A. Baranov, M. S. Mar'enko, Val. S. Rychkov, and G. V. Shlyapnikov. Superfluid pairing in a polarized dipolar Fermi gas. *Phys. Rev. A*, 66:013606, 2002.

[11] W. L. Barclay, Jr., M. A. Anderson, and L. M. Ziurys. The millimeter-wave spectrum of CaH ($X^2\Sigma^+$). *Astrophys. J.*, 408:L65–L67, 1993.

[12] R. F. Barrow and E. W. Deutsch. Rotational analysis of the $A^3\Sigma^- - X^3\Sigma^-$ system of SeO. *Proc. Phys. Soc.*, 82(4):548–556, 1963.

[13] Edward M. Baum, Harold D. Knox, and Thomas R. Miller. Chart of the nuclides, 2002.

[14] C. A. Baumann, R. J. Van Zee, and W. Weltner, Jr. High-spin molecules: Electron spin resonance of manganese halides and sulfide at 4 K. *J. Phys. Chem.*, 86:5084–5093, 1982.

[15] L.-E. Berg and L. Klynning. Rotational analysis of the $a - x$ and $b - x$ band systems of CaH. *Physica Scripta*, 10:331–336, 1974.

[16] Hendrick L. Bethlem, Giel Berden, Floris M. H. Crompvoets, Rienk T. Jongma, André J. A. van Roij, and Gerard Meijer. Electrostatic trapping of ammonia molecules. *Nature*, 406:491–494, 2000.

[17] Hendrick L. Bethlem, Giel Berden, and Gerard Meijer. Decelerating neutral dipolar molecules. *Phys. Rev. Lett.*, 83(8):1558, 1999.

[18] Hendrick L. Bethlem and Gerard Meijer. Production and application of translationally cold molecules. *Int. Rev. Phys. Chem.*, 22(1):73, 2003.

[19] Hendrick L. Bethlem, M R Tarbutt, Jochen Küpper, David Carty, Kirstin Wohlfart, E A Hinds, and Gerard Meijer. Alternating gradient focusing and deceleration of polar molecules. *J. Phys. B*, 39:R263–R291, 2006.

[20] J. R. Bochinski, Eric R. Hudson, H. J. Lewandowski, Gerard Meijer, and Jun Ye. Phase space manipulation of cold free OH molecules. *Phys. Rev. Lett.*, 91(24):243001, 2003.

[21] M. Bogey, C. Demuynck, and J. L. Destomes. Millimeter wave spectrum of SO in highly excited vibrational states: vibrational and isotopic dependence of molecular constants. *Chem. Phys.*, 66:99–104, 1982.

[22] Alexander I. Boldyrev, Jack Simons, and Paul von R. Schleyer. *Ab initio* study of the electronic structures of lithium containing diatomic molecules and ions. *J. Chem. Phys.*, 99(11):8793–8804, 1993.

[23] V. E. Bondybey and E. V. Savchenko. Preface. *Low Temp. Phys.*, 26:629–631, 2000.

[24] S. Boris, A. Golutvin, L. Laptin, V. Lubimov, V. Nagovizin, V. Nozik, E. Novikov, V. Soloshenko, I. Tihomirov, E. Tretjakov, and M. Myasoedov. Neutrino mass from the beta spectrum in the decay of tritium. *Phys. Rev. Lett.*, 58(20):2019–2022, 1987.

[25] C. C. Bradley, C. A. Sackett, J. J. Tollett, and R. G. Hulet. Evidence of Bose-Einstein condensation in an atomic gas with attractive interactions. *Phys. Rev. Lett.*, 75(9):1687–1690, 1995.

[26] C. R. Brazier. First gas phase spectrum of the aluminum carbide molecule: The $B^4\Sigma^- - X^4\Sigma^-$ system. *J. Chem. Phys.*, 98(4):2790–2797, 1993.

[27] C. R. Brazier, R. S. Ram, and P. F. Bernath. Fourier transform spectroscopy of the $A^3\Pi - X^3\Sigma^-$ transition of NH. *J. Mol. Spectrosc.*, 120:381–402, 1986.

[28] H. Bredohl, I. Dubois, and P. Nzohabonayo. The emission spectrum of B_2. *J. Molec. Spec.*, 93:281–285, 1982.

[29] A. W. Brewer, P. A. Davis, and J. B. Kerr. Nitrogen hydride as a possible stratospheric constituent. *Nature*, 240:35–36, 1972.

[30] J. M. Brown and A. J. Merer. Lambda-type doubling parameters for molecules in Π electronic states of triplet and higher multiplicity. *J. Mol. Spectrosc.*, 74:488–494, 1979.

[31] John M. Brown and Alan Carrington. *Rotational Spectroscopy of Diatomic Molecules*. Cambridge University Press, 2003.

[32] A. B. Callear and P. M. Wood. Rates of energy transfer from $N_2 A^3\Sigma_u^+$ to various molecules. *Trans. Faraday Soc.*, 67:272–288, 1971.

[33] Wesley C. Campbell, Gerrit C. Groenenboom, Hsin-I Lu, Edem Tsikata, and John M. Doyle. Time-domain measurement of spontaneous vibrational decay of magnetically trapped NH. Accepted to Phys. Rev. Lett.

[34] Wesley C. Campbell, Edem Tsikata, Hsin-I Lu, Laurens D. van Buuren, and John M. Doyle. Magnetic trapping and zeeman relaxation of NH($X^3\Sigma^-$). *Phys. Rev. Lett.*, 98:213001, 2007.

[35] E. Cantarella, F. Culot, and J. Liévin. *Ab initio* calculation of vibrational dipole moment matrix elements. I. methods of calculation and diatomic test systems. *Physica Scripta*, 46:489–501, 1992.

[36] Jianying Cao, Walter J. Balfour, and Charles X. W. Qian. Deperturbation analysis of the [18.5]1-$X0^+$ system and the electronic structure of ReN: A laser induced and dispersed fluorescence study. *J. Phys. Chem. A*, 101:6741–6745, 1997.

[37] Marcos Casarrubios and Luis Seijo. The *ab initio* model potential method: Third series transition metal elements. *J. Chem. Phys.*, 110(2):784–796, 1999.

[38] C. Chackerian, Jr., G. Guelachvili, A. López-Piñeiro, and R. H. Tipping. Rovibrational intensities for the $\Delta v = 1$ bands of the $X^3\Sigma^-$ nh radical: Experiment and theory. *J. Chem. Phys.*, 90(2):641–649, 1989.

[39] Jinhai Chen, Joost M. Bakker, Achim Peters, Michael Stoll, Gerard Meijer, and Timothy C. Steimle. The Zeeman tuning of the $A^6\Sigma^+ - X^6\Sigma^+$ transition of chromium monohydride. *Phys. Chem. Chem. Phys.*, 9:949–957, 2007.

[40] A. C. Cheung, D. M. Rank, C. H. Townes, D. D. Thornton, and W. J. Welch. Detection of NH_3 molecules in the interstellar medium by their microwave emission. *Phys. Rev. Lett.*, 21(25):1701–1705, 1968.

[41] A. S-C. Cheung, R. C. Hansen, and A. J. Merer. Laser spectroscopy of VO: Analysis of the rotational and hyperfine structure of the $C^4\Sigma^- - X^4\Sigma^-(0,0)$ band. *J. Molec. Spec.*, 91:165–208, 1982.

[42] M. S. Chou, A. M. Dean, and D. Stern. Laser absorption measurements on OH, NH, and NH_2 in NH_3/O_2 flames: Determination of an oscillator strength for NH_2. *J. Chem. Phys.*, 76(11):5334–5340, 1982.

[43] E. A. Cornell and C. E. Weiman. Nobel lecture: Bose-Einstein condensation in a dilute gas, the first 70 years and some recent experiments. *Rev. Mod. Phys.*, 74(3):875–893, 2002.

[44] Eric A. Cornell, Chris Monroe, and Carl E. Wieman. Multiply loaded, ac magnetic trap for neutral atoms. *Phys. Rev. Lett.*, 67(18):2439–2442, 1991.

[45] H. Cybulski, R. V. Krems, H. R. Sadeghpour, A. Dalgarno, J. Kłos, G. C. Groenenboom, A. van der Avoird, D. Zgid, and G. Chałasiński. Interaction of NH($X^3\Sigma^-$) with He: Potential energy surface, bound states, and collisional relaxation. *J. Chem. Phys.*, 122:094307, 2005.

[46] Dingguo Dai and K. Balasubramanian. Spectroscopic properties and potential energy curves for 30 electronic states of ReH. *J. Molec. Spec.*, 158:455–467, 1993.

[47] G. Das, Arnold C. Wahl, and Walter J. Stevens. *Ab initio* study of the NH radical. *J. Chem. Phys.*, 61(1):433–434, 1974.

[48] B. Deh, C. Marzok, C. Zimmermann, and Ph. W. Courteille. Feshbach resonances in mixtures of ultracold ^{6}Li and ^{87}Rb gases. *Phys. Rev. A*, 77:010701(R), 2008.

[49] B. DeMarco and D. S. Jin. Onset of Fermi degeneracy in a trapped atomic gas. *Science*, 285:1703–1706, 1999.

[50] D. DeMille. Quantum computation with trapped polar molecules. *Phys. Rev. Lett.*, 88(6):067901, 2002.

[51] D. DeMille, S. Sainis, J. Sage, T. Bergeman, S. Kotochigova, and E. Tiesinga. Enhanced sensitivity to variation of m_e/m_p in molecular spectra. *Phys. Rev. Lett.*, 100:043202, 2008.

[52] Wolfgang Demtröder. *Laser Spectroscopy*. Springer, 3 edition, 2003.

[53] T. C. DeVore, R. J. Van Zee, and W. Weltner, Jr. High spin molecules: ESR of MnF and MnF_2 at 4 K. *J. Chem. Phys.*, 68(8):3522–3527, 1978.

[54] R. N. Dixon. The 0-0 and 1-0 bands of the $A(^3\Pi_i) - X(^3\Sigma^-)$ system of NH. *Can. J. Phys.*, 37:1171–1186, 1959.

[55] R. N. Dixon and H. M. Lamberton. The A, $^3\Pi$-X, $^3\Sigma^-$ band systems of AsH and AsD. *J. Molec. Spec.*, 25:12–33, 1968.

[56] James A. Dodd, Steven J. Lipson, Dorothy J. Flanagan, William A. M. Blumberg, James C. Person, and Byren David Green. $NH(X^3\Sigma^-, v = 1-3)$ formation and vibrational relaxation in electron-irradiated $Ar/N_2/H_2$ mixtures. *J. Chem. Phys.*, 94(6):4301–4310, 1991.

[57] L. Duband, L. Hui, and A. Lange. Space-borne ^{3}He refrigerator. *Cryogenics*, 30:263–270, 1990.

[58] D. Egorov, W. C. Campbell, B. Friedrich, S. E. Maxwell, E. Tsikata, L. D. van Buuren, and J. M. Doyle. Buffer-gas cooling of NH via the beam loaded buffer-gas method. *Eur. Phys. J. D*, 31:307, 2004.

[59] Dima Egorov, Jonathan D. Weinstein, David Patterson, Bretislav Friedrich, and John M. Doyle. Spectroscopy of laser-ablated buffer-gas-cooled PbO at 4 K and the prospects for measuring the electric dipole moment of the electron. *Phys. Rev. A*, 63:030501(R), 2001.

[60] Dimitri Michael Egorov. *Buffer-gas cooling of diatomic molecules*. PhD thesis, Harvard University, 2004.

[61] Michael S. Elioff, James J. Valentini, and David W. Chandler. Subkelvin cooling NO molecules via "billiard-like" collisions with argon. *Science*, 302:1940, 2003.

[62] O. Fackler, B. Jeziorski, W. Kołos, H. J. Monkhorst, and K. Szalewicz. Accurate theoretical β-decay energy spectrum of the tritium molecule and its neutrino mass dependence. *Phys. Rev. Lett.*, 55(13):1388–1391, 1985.

[63] Paul W. Fairchild, Gregory P. Smith, David R. Crosley, and Jay B. Jeffries. Lifetimes and transition probabilities for NH($A^3\Pi_i - X^3\Sigma^-$). *Chem. Phys. Lett.*, 107(2):181, 1984.

[64] W. T. M. L. Fernando, L. C. O'Brien, and P. F. Bernath. Fourier transform emission spectroscopy: The $B^4\Sigma^- - X^4\Sigma^-$ transition of BC. *J. Chem. Phys.*, 93(12):8482–8487, 1990.

[65] Bretislav Friedrich, Jonathan D. Weinstein, Robert deCarvalho, and John M. Doyle. Zeeman spectroscopy of CaH molecules in a magnetic trap. *J. Chem. Phys.*, 110(5):2376–2383, 1999.

[66] R Fulton, A I Bishop, M N Schneider, and P F Barker. Optical Stark deceleration of nitric oxide and benzene molecules using optical lattices. *J. Phys. B: At. Mol. Opt. Phys.*, 39:S1097, 2006.

[67] James F. Garvey and Aron Kuppermann. Observation and analysis of emission spectra of tungsten hydride. *J. Phys. Chem.*, 92:4583–4588, 1988.

[68] Iouli E. Gordon, Dominique R. T. Appadoo, Alireza Shayesteh, Kaley A. Walker, and Peter F. Bernath. Fourier transform infrared emission spectra of MnH and MnD. *J. Molec. Spec.*, 229:145–149, 2005.

[69] S. Goyal, D. L. Schutt, and G. Scoles. Vibrational spectroscopy of sulfur hexafluoride attached to helium clusters. *Phys. Rev. Lett.*, 69(6):933–936, 1992.

[70] Markus Greiner, Olaf Mandel, Tilman Esslinger, Theodor W. Hänsch, and Immanuel Bloch. Quantum phase transition from a superfluid to a Mott insulator in a gas of ultracold atoms. *Nature*, 415:39–44, 2002.

[71] N. Grevesse, M. Asplund, and A. J. Sauval. The solar chemical composition. *Space Sci. Rev.*, 2007. DOI 10.1007/s11214-007-9173-7.

[72] N. Grevesse, D. L. Lambert, A. J. Sauval, E. F. van Dishoeck, C. B. Farmer, and R. H. Norton. Identification of solar vibration-rotation lines of NH and the solar nitrogen abundance. *Astron. Astrophys.*, 232:225–230, 1990.

[73] Dennis S. Greywall. Specific heat of normal liquid ^{3}He. *Phys. Rev. B*, 27(5):2747–2766, 1983.

[74] Gerrit C. Groenenboom, Roman V. Krems, and Alexander Dalgarno. Zeeman transitions in cold OH$^2\Pi$-He collisions. Manuscript in preparation.

[75] Manish Gupta and Dudley Herschbach. Slowing and speeding molecular beams by means of a rapidly rotating source. *J. Phys. Chem. A*, 105:1626–1637, 2001.

[76] C. Haimberger, J. Kleinert, M. Bhattacharya, and N. P. Bigelow. Forma-

tion and detection of ultracold ground-state polar molecules. *Phys. Rev. A*, 70:021402(R), 2004.

[77] D. T. Halfen, A. J. Apponi, and L. M. Ziurys. Laboratory detection and pure rotational spectrum of the CaC radical ($X^3\Sigma^-$). *Astrophys. J.*, 577:L67–L70, 2002.

[78] John L. Hall, Long-Sheng Ma, Matthew Taubman, Bruce Tiemann, Feng-Lei Hong, Olivier Pfister, and Jun Ye. Stabilization and frequency measurement of the I_2-stabilized Nd:YAG laser. *IEEE Trans. Instrum. Meas.*, 48(2):583–586, 1999.

[79] J. G. E. Harris, R. A. Michniak, S. V. Nguyen, N. Brahms, W. Ketterle, and J. M. Doyle. Buffer gas cooling and trapping of atoms with small effective magnetic moments. *Europhys. Lett.*, 67(2):198–204, 2004.

[80] J. G. E. Harris, R. A. Michniak, S. V. Nguyen, W. C. Campbell, D. Egorov, S. E. Maxwell, L. D. van Buuren, and J. M. Doyle. Deep superconducting magnetic traps for neutral atoms and molecules. *Rev. Sci. Inst.*, 75(1):17, 2004.

[81] J. B. Hasted. *Physics of Atomic Collisions*, chapter 1.6. American Elsevier Publishing Company, Inc., 2 edition, 1972.

[82] Lene Vestergaard Hau, S. E. Harris, Zachary Dutton, and Cyrus H. Behroozi. Light speed reduction to 17 meters per second in an ultracold atomic gas. *Nature*, 397:594–598, 1999.

[83] H. G. Hedderich and P. F. Bernath. Infrared emission spectroscopy of bismuch monohydride and bismuth monodeuteride. *J. Molec. Spec.*, 158:170–176, 1993.

[84] Christoph Heinemann, Wolfram Koch, Gottlieb-Georg Lindner, Dirk Reinen, and Per-Olof Widmark. Ground- and excited-state properties of neutral and anionic selenium dimers and trimers. *Phys. Rev. A*, 54(3):1979–1993, 1996.

[85] Gerhard Herzberg. *Molecular Spectra and Molecular Structure*, volume I. Krieger Publishing Company, Malabar, Florida, 2nd edition, 1989.

[86] Harald F. Hess, Greg P. Kochanski, John M. Doyle, Naoto Masuhara, Daniel Kleppner, and Thomas J. Greytak. Magnetic trapping of spin-polarized atomic hydrogen. *Phys. Rev. Lett.*, 59(6):672–675, 1987.

[87] Hinne Hettema and David R. Yarkony. On the radiative lifetime of the $(a^4\Sigma^-, v, N, F_i)$ levels of the CH radical: An *ab initio* treatment. *J. Chem. Phys.*, 100(12):8991–8998, 1994.

[88] Steven Hoekstra, Joop J. Gilijamse, Boris Sartakov, Nicholas Vanhaecke, Ludwig Scharfenberg, Sebastiaan Y. T. van de Meerakker, and Gerard Meijer. Optical pumping of trapped neutral molecules by blackbody radiation. *Phys. Rev. Lett.*, 98:133001, 2007.

[89] Steven Hoekstra, Markus Metsälä, Peter C. Zieger, Ludwig Scharfenberg, Joop J. Gilijamse, Gerard Meijer, and Sebastiaan Y. T. van de Meerakker. Electrostatic trapping of metastable NH molecules. *Phys. Rev. A*, 76:063408, 2007.

[90] A. Hofzumahaus and F. Stuhl. Electronic quenching, rotational relaxation, and radiative lifetime of NH($^3\Pi, v' = 0, N'$). *J. Chem. Phys.*, 82(7):3152–3159, 1985.

[91] E. Holzschuh, M. Fritschi, and W. Kundig. Measurement of the electron neutrino mass from tritium β-decay. *Phys. Lett. B*, 287:381–388, 1992.

[92] Jon T. Hougen. The calculation of rotational energy levels and rotational line intensities in diatomic molecules. Technical report, National Bureau of Standards Monograph 115.

[93] Y. H. Huang and G. B. Chen. A practical vapor pressure equation for helium-3 from 0.01 k to the critical point. *Cryogenics*, 46(12):833–839, 2006.

[94] K. P. Huber and G. Herzberg, editors. *NIST Chemistry WebBook, NIST Standard Reference Database*, chapter Constants of Diatomic Molecules. Number 69. National Institute of Standards and Technology, Gaithersburg MD, 20899 (http://webbook.nist.gov), 2005.

[95] Eric R. Hudson, H. J. Lewandowski, Brian C. Sawyer, and Jun Ye. Cold molecule spectroscopy for constraining the evolution of the fine structure constant. *Phys. Rev. Lett.*, 96:143004, 2006.

[96] J. J. Hudson, B. E. Sauer, M. R. Tarbutt, and E. A. Hinds. Measurement of the electron electric dipole moment using YbF molecules. *Phys. Rev. Lett.*, 89(2):023003, 2002.

[97] L. R. Hunter. Tests of time-reversal invariance in atoms, molecules, and the neutron. *Science*, 252:73–79, 1991.

[98] Kei ichi Namiki and Shuji Saito. Microwave spectrum of the NiO radical in the $X^3\Sigma^-$ state. *Chem. Phys. Lett.*, 252:343–347, 1996.

[99] Kei ichi Namiki and Shuji Saito. Microwave spectrum of the MnO radical in the $X^6\Sigma^+$ state. *J. Chem. Phys.*, 107(21):8848–8853, 1997.

[100] S. Inouye, J. Goldwin, M. L. Olsen, C. Tinknor, J. L. Bohn, and D. S. Jin. Observation of heteronuclear feshbach resonances in a mixture of Bosons and Fermions. *Phys. Rev. Lett.*, 93(18):183201, 2004.

[101] John David Jackson. *Classical Electrodynamics*. Wiley, 3 edition, 1999.

[102] J. W. C. Johns and D. W. Lepard. Calculation of rotation-electronic energies and relative transition intensities in diatomic molecules. *J. Molec. Spec.*, 55:374–406, 1975.

[103] Paul S. Julienne. $^3\Sigma_u^- - ^3\Sigma_u^+$ coupling in the O_2 $B^3\Sigma_u^-$ predissociation. *J. Molec. Spec.*, 63:60–79, 1976.

[104] Leonid A. Kaledin, Metthew G. Erickson, and Michael C. Heaven. Laser spectroscopy of GdO: Ligand field assignments of $4f^7(^8S)6p \leftarrow 4f^7(^8S)6s$ transitions. *J. Molec. Spec.*, 165:323–333, 1994.

[105] Hideto Kanamori, Chikashi Yamada, James E. Butler, Kentarou Kawaguchi, and Eizi Hirota. Infrared diode laser spectroscopy of the PCl radical. *J. Chem. Phys.*, 83(10):4945–4948, 1985.

[106] Mark A. Kasevich, Erling Riis, Steven Chu, and Ralph G. DeVoe. rf spectroscopy in an atomic fountain. *Phys. Rev. Lett.*, 63(6):612–615, 1989.

[107] Kaoru Katoh, Toshiaki Okabayashi, Mitsutoshi Tanimoto, Yoshiro Sumiyoshi, and Yasuki Endo. Electronic properties of CrF and CrCl in the $X^6\Sigma^+$ state: Observation of the halogen hyperfine structure by Fourier transform microwave spectroscopy. *J. Chem. Phys.*, 120(17):7927–7931, 2004.

[108] H. Kawakami et al. New upper bound on the electron anti-neutrino mass. *Phys. Lett. B*, 256(1):105–111, 1991.

[109] Andrew J. Kerman, Jeremy M. Sage, Sunil Sainis, Thomas Bergeman, and David DeMille. Production of ultracold, polar RbCs* molecules via photoassociation. *Phys. Rev. Lett.*, 92(3):033004, 2004.

[110] Eugene C. Kerr. Orthobaric densities of He^3 1.3°K to 3.2°K. *Phys. Rev.*, 96(3):551–554, 1954.

[111] Wolfgang Ketterle. Nobel lecture: When atoms behave as waves: Bose-Einstein condensation and the atom laser. *Rev. Mod. Phys.*, 74(4):1131–1151, 2002.

[112] Jinha Kim. *Buffer-Gas Loading and Magnetic Trapping of Atomic Europium*. PhD thesis, Harvard University, 1997.

[113] G. B. Kistiakowsky and William P. Slichter. A high intensity source for the molecular beam. part II. experimental. *Rev. Sci. Inst.*, 22(5):333–337, 1951.

[114] Martin Kleinschmidt, Timo Fleig, and Christel M. Marian. Kramers-type splitting in the $X^2\Pi$ and $a^4\Sigma^-$ states of CH and CD calculated in a Hund's case (a) basis. *J. Molec. Spec.*, 211:179–188, 2002.

[115] Bengt Kleman and Ulla Uhler. A $^6\Sigma - ^6\Sigma$ transition in CrH. *Can. J. Phys.*, 37:537–549, 1959.

[116] William Klemperer. Interstellar chemistry. *Proc. Natl. Acad. Sci. USA*, 103(33):12232–12234, 2006.

[117] T. Kraemer, M. Mark, P. Waldburger, J. G. Danzl, C. Chin, B. Engeser, A. D. Lange, K. Pilch, A. Jaakkola, H.-C. Nägerl, and R. Grimm. Evidence for Efimov quantum states in an ultracold gas of caesium atoms. *Nature*, 440:315, 2006.

[118] S. D. Kraft, P. Staanum, J. Lange, L. Vogel, R. Wester, and M. Weidemüller. Formation of ultracold LiCs molecules. *J. Phys. B*, 39:S993–S1000, 2006.

[119] Ch. Kraus et al. Final results from phase II of the Mainz neutrino mass search in tritium β decay. *Eur. Phys. J. C*, 40:447–468, 2005.

[120] R. V. Krems and A. Dalgarno. Quantum-mechanical theory of atom-molecule and molecular collisions in a magnetic field: spin depolarization. *J. Chem. Phys.*, 120(5):2296–2307, 2004.

[121] R. V. Krems, H. R. Sadeghpour, A. Dalgarno, D. Zgid, J. Kłos, and G. Chałasiński. Low-temperature collisions of NH($X^3\Sigma^-$) molecules with He atoms in a magnetic field: An *ab initio* study. *Phys. Rev. A*, 68:051401(R), 2003.

[122] Paul H. Krupenie. The spectrum of molecular oxygen. *J. Phys. Chem. Ref. Data*, 1(2):423–534, 1972.

[123] J. M. Lafferty. *Foundations of Vacuum Science and Technology*. Wiley-Interscience, 1998.

[124] D. L. Lambert and R. Beer. Vibration-rotation bands of NH in the spectrum of alpha orions. *Astrophys. J.*, 177:514–545, 1972.

[125] David L. Lambert. *Private communication*, Aug. 2007.

[126] David L. Lambert, Jeffery A. Brown, Kenneth H. Hinkle, and Hollis R. Johnson. Carbon, nitrogen, and oxygen abundances in betelgeuse. *Astrophys. J.*, 284:223–237, 1984.

[127] David L. Lambert, Bengt Gustafsson, Kjell Eriksson, and Kenneth H. Hinkle. The chemical composition of carbon stars. I. carbon, nitrogen, and oxygen in 30 cool carbon stars in the galactic disk. *Astrophys. J. Suppl.*, 62:373–425, 1986.

[128] Stephen R. Langhoff, Charles W. Bauschlicher, Jr., and Alistair P. Rendell. The spectroscopy of MnH. *J. Molec. Spec.*, 138:108–122, 1989.

[129] O. Launila, B. Simard, and A. M. James. Spectroscopy of MnF: Rotational analysis of the $A^7\Pi \leftarrow X^7\Sigma^+$ (0,0) and (1,0) bands in the near-ultraviolet region. *J. Molec. Spec.*, 159:161–174, 1993.

[130] Helene Lefebvre-Brion and Robert W. Field. *The Spectra and Dynamics of Diatomic Molecules*. Elsevier Academic Press, 2004.

[131] Thierry Leininger and Gwang-Hi Jeung. *Ab initio* calculation of rovibronic transition spectra of CaH. *J. Chem. Phys.*, 103(10):3942–3949, 1995.

[132] J. M. Lents. An evaluation of molecular constants and transition probabilities for the NH free radical. *J. Quant. Spectrosc. Radit. Transfer*, 13:297–310, 1973.

[133] Philip A. Lessard. Cryogenic adsorption of noncondensibles in the high-vacuum regime. *J. Vac. Sci. Technol. A*, 7(3):2373–2376, 1989.

[134] M. M. Litvak and E. N. Rodriguez Kuiper. Cometary NH: Ultraviolet and submilimeter emission. *Astrophys. J.*, 253:622–633, 1982.

[135] Alf Lofthus and Paul H. Krupenie. The spectrum of molecular nitrogen. *J. Phys. Chem. Ref. Data*, 6(1):113–307, 1977.

[136] Zhongxin Ma and K. Balasubramanian. Electronic states of WH. *Chem. Phys. Lett.*, 181(5):467–473, 1991.

[137] M. W. Mancini, G. D. Telles, A. R. L. Caires, V. S. Bagnato, and L. G. Marcassa. Observation of ultracold ground-state heteronuclear molecules. *Phys. Rev. Lett.*, 92(13):133203, 2004.

[138] Aristides Mavridis and James F. Harrison. Electronic structure of the carbyne C-Li and the carbene Li_2C. *J. Am. Chem. Soc.*, 104:3827–3833, 1982.

[139] J. K. Messer and Frank C. De Lucia. Measurement of pressure-broadening parameters for the CO-He system at 4 K. *Phys. Rev. Lett.*, 53(27):2555–2558, 1984.

[140] Harold J. Metcalf and Peter van der Straten. *Laser Cooling and Trapping*. Springer, 1999.

[141] A. Micheli, G. K. Brennen, and P. Zoller. A toolbox for lattice-spin models with polar molecules. *Nature Physics*, 2:341–347, 2006.

[142] Thomas Nelis, John M. Brown, and Kenneth M. Evenson. The spectroscopic observation of the CH radical in its $a^4\Sigma^-$ state. *J. Chem. Phys.*, 88(3):2087–2088, 1988.

[143] P. A. G. O'Hare, Alicia Batana, and Arnold C. Wahl. Arsenic monofluoride (AsF, $^3\Sigma$): Dissociation enthalpy, ionization potential, electron affinity, dipole moment, spectroscopic constants, and idel gas thermodynamic functions from a Hartree-Fock molecular orbital investigation. *J. Chem. Phys.*, 59(12):6495–6501, 1973.

[144] C. Ospelkaus, S. Ospelkaus, L. Humbert, P. Ernst, K. Sengstock, and K. Bongs. Ultracold heteronuclear molecules in a 3D optical lattice. *Phys. Rev. Lett.*, 97:120402, 2006.

[145] C. J. Pethick and H. Smith. *Bose-Einstein Condensation in Dilute Gases*. Cambridge, 2002.

[146] Herbert M. Pickett and Timothy L. Boyd. The millimeter wavelength spectrum of diatomic sulfur. *J. Molec. Spec.*, 75:53–57, 1979.

[147] Frank Pobell. *Matter and Methods at Low Temperatures*. Springer, 2 edition, 1996.

[148] To reproduce the term values in Table I of [153] we had to assume this sign

convention in Table II: $B_e = Y_{0,1}$, $\alpha_e = -Y_{1,1}$, $\gamma_e = Y_{2,1}$, $\delta_e = -Y3,1$, and $\epsilon_e = -Y_{4,1}$.

[149] A. A. Radzig and B. M. Smirnov, editors. *Reference Data on Atoms, Molecules, and Ions*. Springer-Verlag, 1980.

[150] R. S. Ram and P. F. Bernath. High-resolution Fourier-transform emission spectroscopy of the $A^4\Pi - X^4\Sigma^-$ system of WN. *J. Opt. Soc. Am. B: Opt. Phys.*, 11(1):225–230, 1994.

[151] R. S. Ram and P. F. Bernath. Fourier transform inrfared emission spectroscopy of ND and PH. *J. Molec. Spec.*, 176:329–336, 1996.

[152] R. S. Ram, P. F. Bernath, W. J. Balfour, J. Cao, C. X. W. Qian, and S. J. Rixon. Laser and Fourier transform spectroscopy of the [23.8]1-$X0^+$ system of ReN. *J. Molec. Spec.*, 168:350–362, 1994.

[153] R. S. Ram, P. F. Bernath, and K. H. Hinkle. Infrared emission spectroscopy of NH: Comparison of a cryogenic schelle spectrograph with a Fourier transform spectrometer. *J. Chem. Phys.*, 110(12):5557–5563, 1999.

[154] Ram S. Ram, Jacky Liévin, Gang Li, Tsuyoshi Hirao, and Peter F. Bernath. The $X^3\Sigma^-$ ground state of WO. *Chem. Phys. Lett.*, 343:437–445, 2001.

[155] R. Ravelo and M. Baskes. Equilibrium and thermodynamic properties of grey, white, and liquid tin. *Phys. Rev. Lett.*, 79(13):2482–2485, 1997.

[156] R. R. Reddy, A. S. R. Reddy, and T. V. R. Rao. Dissociation energies of SO^+, SF and PBr. *J. Quant. Spectrosc. Radiat. Transfer*, 35(3):167–170, 1986.

[157] Alessandra Ricca and Charles W. Bauschlicher, Jr. The low-lying electronic states of LiC. *Chem. Phys. Lett.*, 244:32–38, 1995.

[158] Thomas R. Roberts and Stephen G. Sydoriak. Thermodynamic properties of liquid helium three. I. the specific heat and entropy. *Phys. Rev.*, 98(6):1672–1678, 1955.

[159] Thomas R. Roberts and Stephen G. Sydoriak. Thermomolecular pressure ratios of He^3 and He^4. *Phys. Rev.*, 102(2):304–308, 1956.

[160] R. G. H. Robertson, T. J. Bowles, G. J. Stephenson, Jr., D. L. Wark, J. F. Wilkerson, and D. A. Knapp. Limit on $\bar{\nu}_e$ mass from observation of the β decay of molecular tritium. *Phys. Rev. Lett.*, 67(8):957–960, 1991.

[161] M. D. Di Rosa. Laser-cooling molecules. *Eur. Phys. J. D*, 31:395–402, 2004.

[162] P. Rosmus and H. J. Werner. Einstein transition-probability coefficients in the electronic ground states of the diatomic hydrides. *J. Molec. Struct.*, 60:405–408, 1980.

[163] A. Roth. *Vacuum Technology*. North-Holland, 3 edition, 1990.

[164] F. Roux, F. Michaud, and J. Verges. High-resolution Fourier spectrometry of the $^{14}N_2$ infrared emission spectrum: Extensive analysis of the $B^3\Pi_g - A^3\Sigma_u^+$ system. *J. Molec. Spec.*, 97:253–265, 1983.

[165] Jan R. Rubbmark, Michael M. Kash, Michael G. Littman, and Daniel Kleppner. Dynamical effects at avoided level crossings: A study of the Landau-Zener effect using Rydberg atoms. *Phys. Rev. A*, 23(6):3107–3117, 1981.

[166] Jeremy M. Sage, Sunil Sainis, Thomas Bergeman, and David DeMille. Optical production of ultracold polar molecules. *Phys. Rev. Lett.*, 94:203001, 2005.

[167] Toru Sakamaki, Toshiaki Okabayashi, and Mitsutoshi Tanimoto. Microwave spectroscopy of the NBr radical in the $X^3\Sigma^-$ state. *J. Chem. Phys.*, 109(17):7169–7175, 1998.

[168] Toru Sakamaki, Toshiaki Okabayashi, and Mitsutoshi Tanimoto. Microwave spectrum of the NI radical in the $X^3\Sigma^-$ ground state. *J. Chem. Phys.*, 111(14):6345–6349, 1999.

[169] L. Santos, G. V. Shlyapnikov, P. Zoller, and M. Lewenstein. Bose-Einstein condensation in trapped dipolar gases. *Phys. Rev. Lett.*, 85(9):1791–1794, 2000.

[170] E. A. Scarl and F. W. Dalby. High field stark effects in CH and NH. *Can. J. Phys.*, 52:1429–1437, 1974.

[171] D. W. Sedgley, A. G. Tobin, T. H. Batzer, and W. R. Call. Characterization of charcoals for helium cryopumping in fusion devices. *Journal of Vacuum Science and Technology A*, 5(4):2572, 1987.

[172] P. M. Sheridan, M. A. Brewster, and L. M. Ziurys. Rotational rest frequencies for CrO ($X^5\Pi_r$) and CrN ($X^4\Sigma^-$). *Astrophys. J.*, 576:1108–1114, 2002.

[173] P. M. Sheridan, J. Xin, L. M. Ziurys, Sara A. Beaton, Stephen M. Kermonde, and John M. Brown. The pure rotational spectrum of NaC in its $X^4\Sigma^-$ state: Observation and interpretation. *J. Chem. Phys.*, 116(13):5544–5550, 2002.

[174] P. M. Sheridan and L. M. Ziurys. Molecules in high spin states II: the pure rotational spectrum of MnF ($X^7\Sigma^+$). *Chem. Phys. Lett.*, 380:632–646, 2003.

[175] Saeyoung Shin, Dale J. Brugh, and Michael D. Morse. Radiative lifetime of the $v = 0, 1$ levels of the $A^6\Sigma^+$ state of CrH. *Astrophys. J.*, 619(1):407–411, 2005.

[176] D. M. Silveira, O. Pereira, M. Veloso, and Claudio L. Cesar. Low energy (anti)atoms for precision tests of basic physics. *Brazilian Journal of Physics*, 31(2):203–210, June 2001.

[177] Verne V. Smith and David L. Lambert. The chemical composition of red giants. II. helium burning and the s-process in the MS and S stars. *Astrophys. J.*, 311:843–863, 1986.

[178] C. A. Stan, M. W. Zwierlein, C. H. Schunck, S. M. F. Raupach, and W. Ketterle. Observation of Feshbach resonances between two different atomic species. *Phys. Rev. Lett.*, 93(14):143001, 2004.

[179] Wolfgang Stoeffl and Daniel J. Decman. Anomalous structure in the beta decay of gaseous molecular tritium. *Phys. Rev. Lett.*, 75(18):3237–3240, 1995.

[180] S. N. Suchard, editor. *Spectroscopic Data*, volume 1. IFI/Plenum Data Company, 1975.

[181] G. W. Swift. Thermoacoustic engines. *J. Acoust. Soc. Am.*, 84(4):1145–1180, 1988.

[182] N. S-K. Sze and A. S-C. Cheung. Laser induced fluorescence spectrum of the $A^4\Pi - X^4\Sigma^-(0, 0)$ band of MoN. *J. Molec. Spec.*, 173:194–204, 1995.

[183] T. Takekoshi and R. J. Knize. CO_2 laser trap for cesium atoms. *Opt. Lett.*, 21(1):77–79, 1996.

[184] T. Takekoshi, B. M. Patterson, and R. J. Knize. Observation of optically trapped cold cesium molecules. *Phys. Rev. Lett.*, 81(23):5105–5108, 1998.

[185] J. M. Thompson, M. A. Brewster, and L. M. Ziurys. Molecules in high spin states: The millimeter and submillimeter spectrum of the MnS radical ($X^6\Sigma^+$). *J. Chem. Phys.*, 116:10212, 2002.

[186] W. Ubachs, J. J. ter Meulen, and A. Dymanus. High-resolution laser spectroscopy on the $A^3\Pi \leftarrow X^3\Sigma^-$ transition of NH. *Can. J. Phys.*, 62:1374, 1984.

[187] Rolf-Dieter Urban, Kay Essig, and Harold Jones. The molecular parameters of the antimony monodeuteride radical from diode laser spectroscopy. *J. Chem. Phys.*, 99(3):1591–1596, 1993.

[188] Sebastiaan Y. T. van de Meerakker, Irena Labazan, Steven Hoekstra, Jochen Küpper, and Gerard Meijer. Production and deceleration of a pulsed beam of metastable NH ($a^1\delta$) radicals. *J. Phys. B: At. Mol. Opt. Phys.*, 39:S1077, 2006.

[189] Sebastiaan Y. T. van de Meerakker, Paul H. M. Smeets, Nicolas Vanhaecke, Rienk T. Jongma, and Gerard Meijer. Deceleration and electrostatic trapping of OH radicals. *Phys. Rev. Lett.*, 94:023004, 2005.

[190] Sebastiaan Y. T. van de Meerakker, Nicolas Vanhaecke, Mark P. J. van der Loo, Gerrit C. Groenenboom, and Gerard Meijer. Direct measurement of the radia-

tive lifetime of vibrationally excited OH radicals. *Phys. Rev. Lett.*, 95:013003, 2005.

[191] Jacqueline van Veldhoven, Hendrick L. Bethlem, and Gerard Meijer. ac electric trap for ground-state molecules. *Phys. Rev. Lett.*, 94:083001, 2005.

[192] Thad G. Walker and William Happer. Spin-exchange optical pumping of noble-gas nuclei. *Rev. Mod. Phys.*, 69(2):629–641, 1997.

[193] D. Wang et al. The photoassociative spectroscopy, photoassociative molecule formation, and trapping of ultracold $^{39}K^{85}Rb$. *Euro. Phys. J. D.*, 31:165–177, 2004.

[194] F. D. Wayne and H. E. Radford. The laser magnetic resonance spectra of imine (NH) and its isotopes. *Molecular Physics*, 32(5):1407–1422, 1976.

[195] Ch. Weinheimer et al. Improved limit on the electron-antineutrino rest mass from tritium β-decay. *Phys. Lett. B*, 300:210–216, 1993.

[196] Jonathan D. Weinstein, Robert deCarvalho, Karine Amar, Andrea Boca, Brian C. Odom, Bretislav Friedrich, and John M. Doyle. Spectroscopy of buffer-gas cooled vanadium monoxide in a magnetic trapping field. *J. Chem. Phys.*, 109(7):2656, 1998.

[197] Jonathan D. Weinstein, Robert deCarvalho, Thierry Guillet, Bretislav Friedrich, and John M. Doyle. Magnetic trapping of calcium monohydride molecules at milikelvin temperatures. *Nature*, 395:148, 1998.

[198] Jonathan David Weinstein. *Magnetic Trapping of Atomic Chromium and Molecular Calcium Monohydride*. PhD thesis, Harvard University, 2001.

[199] Daniel R. Willey, Richard L. Crownover, D. N. Bittner, and Frank C. De Lucia. Very low temperature spectroscopy: The pressure broadening coefficients of CO-He between 4.3 and 1.7 K. *J. Chem. Phys.*, 89(4):1923–1928, 1988.

[200] Stefan Willitsch, Martin T. Bell, Alexander D. Gingell, Simon R. Procter, and Timothy P. Softley. Cold reactive collisions between laser-cooled ions and velocity-selected neutral molecules. *Phys. Rev. Lett.*, 100:043203, 2008.

[201] J. Xin and L. M. Ziurys. Gas phase spectroscopy of alkali carbides: The pure rotational spectrum of KC ($X^4\Sigma^-$). *J. Chem. Phys.*, 110(10):4797–4802, 1999.

[202] J. Xin and L. M. Ziurys. Structural studies of alkali methylidyne radicals: High resolution spectroscopy of NaCH and KCH ($\tilde{X}^3\Sigma^-$). *J. Chem. Phys.*, 110(7):3360–3367, 1999.

[203] Chikashi Yamada, Man Chai Chang, and Eizi Hirota. Infrared diode laser spectroscopy of the PF radical. *J. CHem. Phys.*, 86(7):3804–3806, 1987.

[204] Chikashi Yamada, Yasuki Endo, and Eizi Hirota. The microwave spectrum of the $N^{35}Cl$ radical in the $X^3\Sigma^-$ state. *J. Chem. Phys.*, 79(9):4159–4166, 1983.

[205] W.-M. Yao et al. Review of particle physics. *J. Phys. G*, 33:1+, 2006.

[206] David R. Yarkony. On the electronic structure of the NH radical. The fine structure splitting of the $X^3\Sigma^-$ state and the spin-forbidden $(b^1\Sigma^+, a^1\Delta) \rightarrow$

$X^3\Sigma^-$, and the spin-allowed $A^3\Pi \rightarrow X^3\Sigma^-$ and $c^1\Pi \rightarrow (b^1\Sigma^+, a^1\Delta)$, radiative transitions. *J. Chem. Phys.*, 91(8):4745–4757, 1989.

[207] R. N. Zare, A. L. Schmeltekopf, W. J. Harrop, and D. L. Albritton. A direct approach for the reduction of diatomic spectra to molecular constants for the construction of RKR potentials. *J. Mol. Spectrosc.*, 46:37–66, 1973.

[208] Richard N. Zare. *Angular Momentum*. John Wiley and Sons, 1988.

[209] T. Zelevinsky, S. Kotochigova, and Jun Ye. Precision test of mass-ratio variations with lattice-confined ultracold molecules. *Phys. Rev. Lett.*, 100:043201, 2008.

[210] J. J. Zirbel, K.-K. Ni, S. Ospelkaus, J. P. D'Incao, C. E. Weiman, J. Ye, and D. S. Jin. Collisional stability of Fermionic Feshbach molecules. arXiv:0710.2479v1.

Appendix A

Zeeman Effect in NH

The Zeeman effect on the $X^3\Sigma^-$ and $A^3\Pi$ states of the NH radical is calculated for fields up to a few Tesla, yielding lineshifts for the A $\leftrightarrow$ X electronic transition. The calculation takes into account the lowest few rotational states of each manifold and shows deviations from linearity at higher values of the magnetic field due to mixing of these states.

A.1 Zero-field Hamiltonian

The field-free Hamiltonian of the molecule is introduced in the Hund's case (a) basis for the ground vibrational level of the $^3\Sigma^-$ and $^3\Pi$ electronic states of NH.

A.1.1 Basis Set

The $^3\Sigma$ state of NH is best described by Hund's case (b) and $^3\Pi$ state of NH is intermediate between Hund's case (a) and (b). Since it is common and convenient to

perform calculations in the case (a) basis we will follow that convention here (though for low rotational quantum numbers we fully expect the $^3\Pi$ state to approach Hund's case (b)). The case (a) basis consists of vectors $|\Lambda, S, \Sigma; \Omega, J, M\rangle$ where $\Omega = \Lambda + \Sigma$. Each of the three multiplet states of the triplet will be doubly degenerate (unless we take into account the effects of Lambda-type doubling of the $^3\Pi$ state) leaving six distinct states for each J,M pair. We will label these states in the case (a) basis as follows.

$$
\begin{aligned}
|^3\Sigma_{+1}, J, M\rangle &\equiv |0, 1, 1; 1, J, M\rangle \\
|^3\Sigma_{0}, J, M\rangle &\equiv |0, 1, 0; 0, J, M\rangle \\
|^3\Sigma_{-1}, J, M\rangle &\equiv |0, 1, -1; -1, J, M\rangle \\
|^3\Pi_{+0}, J, M\rangle &\equiv |1, 1, -1; 0, J, M\rangle \\
|^3\Pi_{-0}, J, M\rangle &\equiv |-1, 1, 1; 0, J, M\rangle \\
|^3\Pi_{+1}, J, M\rangle &\equiv |1, 1, 0; 1, J, M\rangle \\
|^3\Pi_{-1}, J, M\rangle &\equiv |-1, 1, 0; -1, J, M\rangle \\
|^3\Pi_{+2}, J, M\rangle &\equiv |1, 1, 1; 2, J, M\rangle \\
|^3\Pi_{-2}, J, M\rangle &\equiv |-1, 1, -1; -2, J, M\rangle.
\end{aligned}
$$

The states given above are simple to express in the case (a) basis but are not all parity eigenstates. We can construct linear combinations of the states above and label them by their e/f symmetry to form the following parity eigenstates:

$$
|^3\Sigma_1^e, J, M\rangle \equiv \frac{1}{\sqrt{2}}\left(|^3\Sigma_{+1}, J, M\rangle + |^3\Sigma_{-1}, J, M\rangle\right)
$$

$$
\begin{aligned}
|^3\Sigma_1^f, J, M\rangle &\equiv \frac{1}{\sqrt{2}}\left(|^3\Sigma_{+1}, J, M\rangle - |^3\Sigma_{-1}, J, M\rangle\right) \\
|^3\Sigma_0^e, J, M\rangle &\equiv |^3\Sigma_0, J, M\rangle \\
|^3\Pi_0^e, J, M\rangle &\equiv \frac{1}{\sqrt{2}}\left(|^3\Pi_{+0}, J, M\rangle + |^3\Pi_{-0}, J, M\rangle\right) \\
|^3\Pi_0^f, J, M\rangle &\equiv \frac{1}{\sqrt{2}}\left(|^3\Pi_{+0}, J, M\rangle - |^3\Pi_{-0}, J, M\rangle\right) \\
|^3\Pi_1^e, J, M\rangle &\equiv \frac{1}{\sqrt{2}}\left(|^3\Pi_{+1}, J, M\rangle + |^3\Pi_{-1}, J, M\rangle\right) \\
|^3\Pi_1^f, J, M\rangle &\equiv \frac{1}{\sqrt{2}}\left(|^3\Pi_{+1}, J, M\rangle - |^3\Pi_{-1}, J, M\rangle\right) \\
|^3\Pi_2^e, J, M\rangle &\equiv \frac{1}{\sqrt{2}}\left(|^3\Pi_{+2}, J, M\rangle + |^3\Pi_{-2}, J, M\rangle\right) \\
|^3\Pi_2^f, J, M\rangle &\equiv \frac{1}{\sqrt{2}}\left(|^3\Pi_{+2}, J, M\rangle - |^3\Pi_{-2}, J, M\rangle\right)
\end{aligned} \tag{A.1}
$$

which will have parities $(-1)^J$ and $-(-1)^J$ for e and f symmetries, respectively [30]. A diagram of the $A^3\Pi \leftrightarrow X^3\Sigma^-$ transition is shown in Figure 3.1.1.

A.1.2 Nonrotating Hamiltonian

For a nonrotating molecule there will be contributions from the bare electronic configuration and the spin-orbit coupling in the $^3\Pi$ states, which is characterized by the spin-orbit coupling constant A. There will only be diagonal matrix elements given by

$$\langle^3\Sigma|H_o|^3\Sigma\rangle \equiv 0 \tag{A.2}$$

$$\langle^3\Pi|H_o|^3\Pi\rangle = \text{const} + \langle^3\Pi|A\mathbf{L}\cdot\mathbf{S}|^3\Pi\rangle = \text{const} + A\Lambda\Sigma \tag{A.3}$$

where the constant can in general contain information about the electronic and vibrational degrees of freedom. From this it is evident that the $^3\Pi$ triplet splitting will

(at least in the rotational ground state) be set by the spin-orbit constant.

A.1.3 Rotational Hamiltonian

The rotational angular momentum vector in a diatomic molecule is necessarily oriented perpendicular to the internuclear axis (referred to here at the z-axis, which is not to be confused with the Z-axis of the magnetic field in the laboratory frame) and will be equal to $\mathbf{J} - \mathbf{L} - \mathbf{S}$. Since it only has x and y components, we can write

$$H_{\rm rot} = B\mathbf{R}^2 = B\left[(J_x - L_x - S_x)^2 + (J_y - L_y - S_y)^2\right] \tag{A.4}$$

where B is the rotational constant. This can be rewritten[92] as

$$\begin{aligned} H_{\rm rot} &= B\Big[J^2 - J_z^2 + L^2 - L_z^2 + S^2 - S_z^2 + \\ &\quad L_+S_- + L_-S_+ - J_+L_- - J_-L_+ - J_+S_- - J_-S_+] \end{aligned} \tag{A.5}$$

where $\mathcal{O}_\pm = \mathcal{O}_x \pm i\mathcal{O}_y$ for the operators J,L, and S. The top line of Equation (A.5) has the diagonal elements and the bottom line connects states of various Ω, Σ, and Λ. Of these diagonal components, all can be evaluated trivially except for $\langle\Lambda|L^2 - L_z^2|\Lambda\rangle$ since L is not a good quantum number, but this matrix element is a constant [92] and can be set equal to 0. Thus, we have

$$\langle S,\Sigma;\Omega,J|H_{\rm rot}|S,\Sigma;\Omega,J\rangle = B\left[J(J+1) - \Omega^2 + S(S+1) - \Sigma^2\right]. \tag{A.6}$$

To evaluate the off-diagonal terms, it is helpful to recall the following:

$$\langle S,\Sigma\pm1|S_\pm|S,\Sigma\rangle = \sqrt{(S\mp\Sigma)(S\pm\Sigma+1)}$$

$$\begin{aligned} \langle L, \Lambda \pm 1 | L_{\pm} | L, \Lambda \rangle &= \sqrt{(L \mp \Lambda)(L \pm \Lambda + 1)} \\ \langle J, \Omega \pm 1 | J_{\mp} | J, \Omega \rangle &= \sqrt{(J \mp \Omega)(J \pm \Omega + 1)}. \end{aligned} \tag{A.7}$$

Note that $J_{\pm}$ raises (lowers) where $S_{\pm}$ and $L_{\pm}$ lower (raise).

In evaluating the off-diagonal elements of $H_{\rm rot}$ it is evident that $L_{\pm}$ can only connect states of $\Delta\Lambda = \pm 1$, whereas if we limit ourselves to the $^3\Pi$, or, separately, the $^3\Sigma$ state of NH we have only $\Delta\Lambda = \pm 2,0$. These operators can in general introduce coupling to Σ, Π, and Δ states with similar energies and good wavefunction overlap, but this interaction will be disregarded for this calculation. This leaves us with

$$\begin{aligned} \langle S, \Sigma \pm 1; \Omega \pm 1, J | H_{\rm rot} | S, \Sigma; \Omega, J \rangle &= -B \langle S, \Sigma \pm 1; \Omega \pm 1, J | J_+ S_- + J_- S_+ | S, \Sigma; \Omega, J \rangle \\ &= -B \sqrt{(S \mp \Sigma)(S \pm \Sigma + 1)(J \mp \Omega)(J \pm \Omega + 1)} \end{aligned} \tag{A.8}$$

The off-diagonal terms only couple states with the same total angular momentum J, but we don't necessarily have the maximum number of states for every J since each substate in the triplet will have a different minimum J. For instance, for $J = 0$ the $^3\Pi_0$ states are the only available from the $^3\Pi$ excited level, whereas we have all six states for $J = 2$: $^3\Pi_0(R = 2)$, $^3\Pi_1(R = 1)$, and $^3\Pi_2(R = 0)$. To include all six of the lowest states in the $^3\Pi$ manifold in our calculation we will need to include 12 states of various rotational and electron orbital angular momentum, and each of these will have a number of different projections of their total angular momentum on the magnetic field direction (Zeeman sublevels).

A.1.4 Spin-Rotation Hamiltonian

Despite the fact that the spin-rotation constant in NH is more than an order of magnitude smaller than the spin-spin constant (which dominates the rotational dependence of the multiplet splitting) we will treat it here for completeness. The spin-rotation Hamiltonian is given by

$$\begin{aligned} H_{\text{S-Rot}} &= \gamma \mathbf{R} \cdot \mathbf{S} \\ &= \gamma \left[(J_x - L_x - S_x)\hat{x} + (J_y - L_y - S_y)\hat{y} \right] \cdot \mathbf{S} \\ &= \gamma \left[S_z^2 - S^2 - \frac{1}{2} L_+ S_- - \frac{1}{2} L_- S_+ + \frac{1}{2} J_+ S_- + \frac{1}{2} J_- S_+ \right] \\ &= \gamma \left[S_z^2 - S^2 + \frac{1}{2} J_+ S_- + \frac{1}{2} J_- S_+ \right]. \end{aligned} \tag{A.9}$$

In moving from the second to the third lines in Equation (A.9) we have again neglected any coupling to nearby Σ, Π, or Δ states.

The spin-rotation Hamiltonian has diagonal[1] and off-diagonal terms, and the diagonal components can be evaluated directly as

$$\langle S, \Sigma | H_{\text{S-Rot}} | S, \Sigma \rangle = \gamma \left(\Sigma^2 - S(S+1) \right) \tag{A.11}$$

while the off-diagonal components yield the same form as Equation (A.8) with the substitution $-B \rightarrow \gamma/2$.

[1] As noted by Zare *et al.* [207], the from of what is called the spin-rotation Hamiltonian is not standardized in the molecular spectroscopy community. The from given above ($H_{\text{S-Rot}} = \gamma \mathbf{R} \cdot \mathbf{S}$) will here be referred to as the *phenomenological* spin-rotation interaction and the other common form ($\tilde{H}_{\text{S-Rot}} = \gamma \mathbf{N} \cdot \mathbf{S}$) will be designated the *inclusive* spin-rotation interaction. The results for the inclusive spin-rotation interaction are identical for the off-diagonal elements, but the diagonal elements of the inclusive spin-rotation Hamiltonian will be given by

$$\langle S, \Sigma | \tilde{H}_{\text{S-Rot}} | S, \Sigma \rangle = \gamma \left(\Sigma\Omega - S(S+1) \right). \tag{A.10}$$

A.1.5 Spin-Spin Hamiltonian

The true spin-spin interaction will couple to rotation and is discussed in Appendix C. I will use the first-order interaction as given by [130] (p.196)

$$H_{\mathrm{SS}} = \frac{2}{3}\lambda(3S_z^2 - S^2) \tag{A.12}$$

where λ is the spin-spin constant. There will only be diagonal contributions from this term of the from

$$\langle S, \Sigma | H_{\mathrm{SS}} | S, \Sigma \rangle = \frac{2}{3}\lambda \left(3\Sigma^2 - S\left(S+1\right)\right). \tag{A.13}$$

A.2 Zeeman Hamiltonian

We will approach the problem of accounting for the magnetic field interaction in the same way as the zero-field Hamiltonian by finding its matrix elements and applying numerical diagonalization to find the corresponding energy eigenvalues for each magnetic field magnitude. This analysis essentially follows from [65] and [92] but has been extended to $^3\Sigma$ and $^3\Pi$ molecules.

A.2.1 H_{Z} *via* the Direction Cosine Matrix

The Zeeman Hamiltonian is given by $H_{\mathrm{Z}} = -\mu_Z \mathcal{H}$ where $\mathcal{H}$ is the magnetic field and

$$\mu_Z = \frac{1}{2}\left(\mathbf{\Phi}_Z^+ \mu_- + \mathbf{\Phi}_Z^- \mu_+\right) + \mathbf{\Phi}_Z^z \mu_z \tag{A.14}$$

where $\mathbf{\Phi}$ is the direction cosine matrix [92] and $\mu_a = -\left(g_L L_a + g_S S_a\right)\mu_{\mathrm{B}}$ with μ_{B} the Bohr magneton. Capital letters denote axes in the lab frame (with $\mathcal{H}$ pointing in the Z-direction) and lowercase letters denote the molecule-fixed axes.

Using the definitions of raising and lowering operators introduced for Equation (A.5) we can rewrite this as

$$H_{\mathrm{Z}} = \mathcal{H}\mu_{\mathrm{B}}\left[\frac{1}{2}g_L\left(\mathbf{\Phi}_Z^+ L_- + \mathbf{\Phi}_Z^- L_+\right) + \frac{1}{2}g_S\left(\mathbf{\Phi}_Z^+ S_- + \mathbf{\Phi}_Z^- S_+\right) + \mathbf{\Phi}_Z^z\left(g_L L_z + g_S S_z\right)\right]. \tag{A.15}$$

If we can again disregard the effect of other $\Delta\Lambda = \pm 1$ states we can eliminate all terms with $L_\pm$ to leave us with

$$H_{\mathrm{Z}} = \mathcal{H}\mu_{\mathrm{B}}\left[\frac{1}{2}g_S\left(\mathbf{\Phi}_Z^+ S_- + \mathbf{\Phi}_Z^- S_+\right) + \mathbf{\Phi}_Z^z\left(g_L L_z + g_S S_z\right)\right]. \tag{A.16}$$

A.2.2 Explicit Matrix Elements of H_{Z}

To evaluate the matrix elements of these expressions, Hougen points out the separability of the operator pairs:

> The elements of the 3×3 direction cosine matrix [$\mathbf{\Phi}$] do not involve the electronic or vibrational variables of a diatomic molecule; they involve only the rotational angles ... Consequently, matrix elements of elements of the direction cosine matrix are diagonal in the nonrotating-molecule quantum numbers L, Λ, S, Σ.

and provides a table of the matrix elements of the direction cosine matrix[92].

We can now write down an expression for the matrix elements of the Zeeman Hamiltonian:

$$\begin{aligned}
&\langle \Lambda', S', \Sigma'; \Omega', J', M' | H_{\mathrm{Z}} | \Lambda, S, \Sigma; \Omega, J, M\rangle = \\
&\quad \frac{1}{2}\mathcal{H} g_S \mu_{\mathrm{B}} \langle \Lambda', S', \Sigma' | S_- | \Lambda, S, \Sigma\rangle \langle \Omega', J', M' | \mathbf{\Phi}_Z^+ | \Omega, J, M\rangle && \text{(A.17)}\\
&\quad + \frac{1}{2}\mathcal{H} g_S \mu_{\mathrm{B}} \langle \Lambda', S', \Sigma' | S_+ | \Lambda, S, \Sigma\rangle \langle \Omega', J', M' | \mathbf{\Phi}_Z^- | \Omega, J, M\rangle && \text{(A.18)}\\
&\quad + \mathcal{H}\mu_{\mathrm{B}} \langle \Lambda', S', \Sigma' | g_L L_z + g_S S_z | \Lambda, S, \Sigma\rangle \langle \Omega', J', M' | \mathbf{\Phi}_Z^z | \Omega, J, M\rangle. && \text{(A.19)}
\end{aligned}$$

Bare Basis Matrix Elements

For the purposes of our calculation, line (A.17) will apply when $\Sigma' = \Sigma - 1$ and $\Omega' = \Omega - 1$, line (A.18) when $\Sigma' = \Sigma + 1$ and $\Omega' = \Omega + 1$, and line (A.19) when $\Sigma' = \Sigma$ and $\Omega' = \Omega$. The direction cosine matrix elements are only nonzero for $\Delta J = 0, \pm 1$, so for each of the three cases above there will be three possible ΔJ values. The explicit forms will be given here.

$$\langle \Sigma - 1, \Omega - 1, J + 1, M | H_{\mathrm{Z}} | \Sigma, \Omega, J, M \rangle = \tag{A.20}$$
$$\frac{1}{2}\mathcal{H} g_S \mu_{\mathrm{B}} \frac{\sqrt{(S+\Sigma)(S-\Sigma+1)(J-\Omega+1)(J-\Omega+2)(J+M+1)(J-M+1)}}{(J+1)\sqrt{(2J+1)(2J+3)}}$$

$$\langle \Sigma - 1, \Omega - 1, J, M | H_{\mathrm{Z}} | \Sigma, \Omega, J, M \rangle = \tag{A.21}$$
$$\frac{1}{2}\mathcal{H} g_S \mu_{\mathrm{B}} \frac{M\sqrt{(S+\Sigma)(S-\Sigma+1)(J+\Omega)(J-\Omega+1)}}{J(J+1)}$$

$$\langle \Sigma - 1, \Omega - 1, J - 1, M | H_{\mathrm{Z}} | \Sigma, \Omega, J, M \rangle = \tag{A.22}$$
$$-\frac{1}{2}\mathcal{H} g_S \mu_{\mathrm{B}} \frac{\sqrt{(S+\Sigma)(S-\Sigma+1)(J+\Omega)(J+\Omega-1)(J+M)(J-M)}}{J\sqrt{(2J+1)(2J-1)}}$$

$$\langle \Sigma, \Omega, J + 1, M | H_{\mathrm{Z}} | \Sigma, \Omega, J, M \rangle = \tag{A.23}$$
$$\mathcal{H}\mu_{\mathrm{B}} (g_L \Lambda + g_S \Sigma) \frac{\sqrt{(J+\Omega+1)(J-\Omega+1)(J+M+1)(J-M+1)}}{(J+1)\sqrt{(2J+1)(2J+3)}}$$

$$\langle \Sigma, \Omega, J, M | H_{\mathrm{Z}} | \Sigma, \Omega, J, M \rangle = \tag{A.24}$$
$$\mathcal{H}\mu_{\mathrm{B}} (g_L \Lambda + g_S \Sigma) \frac{\Omega M}{J(J+1)}$$

$$\langle \Sigma, \Omega, J-1, M|H_{\mathrm{Z}}|\Sigma, \Omega, J, M\rangle = \mathcal{H}\mu_{\mathrm{B}}\left(g_L\Lambda + g_S\Sigma\right)\frac{\sqrt{\left(J+\Omega\right)\left(J-\Omega\right)\left(J+M\right)\left(J-M\right)}}{J\sqrt{\left(2J+1\right)\left(2J-1\right)}} \tag{A.25}$$

$$\langle \Sigma+1, \Omega+1, J+1, M|H_{\mathrm{Z}}|\Sigma, \Omega, J, M\rangle = -\frac{1}{2}\mathcal{H}g_S\mu_{\mathrm{B}}\frac{\sqrt{\left(S-\Sigma\right)\left(S+\Sigma+1\right)\left(J+\Omega+1\right)\left(J+\Omega+2\right)\left(J+M+1\right)\left(J-M+1\right)}}{\left(J+1\right)\sqrt{\left(2J+1\right)\left(2J+3\right)}} \tag{A.26}$$

$$\langle \Sigma+1, \Omega+1, J, M|H_{\mathrm{Z}}|\Sigma, \Omega, J, M\rangle = \frac{1}{2}\mathcal{H}g_S\mu_{\mathrm{B}}\frac{M\sqrt{\left(S-\Sigma\right)\left(S+\Sigma+1\right)\left(J-\Omega\right)\left(J+\Omega+1\right)}}{J\left(J+1\right)} \tag{A.27}$$

$$\langle \Sigma+1, \Omega+1, J-1, M|H_{\mathrm{Z}}|\Sigma, \Omega, J, M\rangle = \frac{1}{2}\mathcal{H}g_S\mu_{\mathrm{B}}\frac{\sqrt{\left(S-\Sigma\right)\left(S+\Sigma+1\right)\left(J-\Omega\right)\left(J-\Omega-1\right)\left(J+M\right)\left(J-M\right)}}{J\sqrt{\left(2J+1\right)\left(2J-1\right)}} \tag{A.28}$$

Diagonal Components of $H_{\mathbf{Z}}$

All of the diagonal components of the Zeeman Hamiltonian will be of the form found in Equation (A.24) and can be found explicitly below in our basis:

$$\langle {}^3\Sigma_1^{e/f}, J|H_{\mathrm{Z}}|{}^3\Sigma_1^{e/f}, J\rangle = \frac{g_S}{J\left(J+1\right)}\mathcal{H}\mu_{\mathrm{B}}M \tag{A.29}$$

$$\langle {}^3\Sigma_0^{e}, J|H_{\mathrm{Z}}|{}^3\Sigma_0^{e}, J\rangle = 0 \tag{A.30}$$

$$\langle {}^3\Pi_0^{e/f}, J|H_{\mathrm{Z}}|{}^3\Pi_0^{e/f}, J\rangle = 0 \tag{A.31}$$

$$\langle {}^3\Pi_1^{e/f}, J|H_{\mathrm{Z}}|{}^3\Pi_1^{e/f}, J\rangle = \frac{g_L}{J\left(J+1\right)}\mathcal{H}\mu_{\mathrm{B}}M \tag{A.32}$$

$$\langle {}^3\Pi_2^{e/f}, J|H_{\mathrm{Z}}|{}^3\Pi_2^{e/f}, J\rangle = \frac{2\left(g_L+g_S\right)}{J\left(J+1\right)}\mathcal{H}\mu_{\mathrm{B}}M. \tag{A.33}$$

It is worth noting that Equations (A.29,A.32,A.33) cannot diverge at $J = 0$ since only $|^3\Sigma_0^e, J\rangle$ and $|^3\Pi_0^{e/f}, J\rangle$ exist when $J = 0$ and while it appears Equation (A.24) diverges for $J = 0$ we see that Equations (A.31,A.30) are zero independent of J for these parity eigenstates.

Off-diagonal Components of $H_{\mathbf{Z}}$

The off-diagonal components of the Zeeman Hamiltonian will be nonzero only for states of opposite parity and $\Delta\Sigma = \Delta\Omega = 0, \pm 1$. The e/f symmetry notation can be used to find whether two states have the same parity by recalling that e/f symmetry is total parity without the contribution from the rotational part of the wavefunction, which will alternate positive and negative parity as R is increased. For example, two e states in the same rotational level will have the same parity, as will an e and an f state whose rotational quantum numbers differ by an odd integer.

Aside from these two considerations, the matrix elements of the Zeeman Hamiltonian are diagonal in M, the projection of the total angular momentum on the Z-axis. If we leave the expressions for these elements in terms of M we have seventeen nonzero cases:

$$\langle {}^3\Sigma_1^f, J+1|H_{\mathrm{Z}}|{}^3\Sigma_0^e, J\rangle = -g_S\mathcal{H}\mu_{\mathrm{B}}\frac{\sqrt{(J+1)(J+2)(J+M+1)(J-M+1)}}{(J+1)\sqrt{(2J+1)(2J+3)}} \tag{A.34}$$

$$\langle {}^3\Sigma_1^e, J|H_{\mathrm{Z}}|{}^3\Sigma_0^e, J\rangle = g_S\mathcal{H}\mu_{\mathrm{B}}\frac{M}{\sqrt{J(J+1)}} \tag{A.35}$$

$$\langle {}^3\Sigma_1^f, J-1|H_{\rm Z}|{}^3\Sigma_0^e, J\rangle = g_S\mathcal{H}\mu_{\rm B}\frac{\sqrt{J\,(J-1)\,(J+M)\,(J-M)}}{J\sqrt{(2J+1)\,(2J-1)}} \tag{A.36}$$

$$\langle {}^3\Sigma_1^{e/f}, J+1|H_{\rm Z}|{}^3\Sigma_1^{f/e}, J\rangle = g_S\mathcal{H}\mu_{\rm B}\frac{\sqrt{J\,(J+2)\,(J+M+1)\,(J-M+1)}}{(J+1)\sqrt{(2J+1)\,(2J+3)}} \tag{A.37}$$

$$\langle {}^3\Sigma_1^{e/f}, J-1|H_{\rm Z}|{}^3\Sigma_1^{f/e}, J\rangle = g_S\mathcal{H}\mu_{\rm B}\frac{\sqrt{(J+1)\,(J-1)\,(J+M)\,(J-M)}}{J\sqrt{(2J+1)\,(2J-1)}} \tag{A.38}$$

$$\langle {}^3\Pi_0^{e/f}, J-1|H_{\rm Z}|{}^3\Pi_0^{f/e}, J\rangle = (g_L-g_S)\,\mathcal{H}\mu_{\rm B}\frac{\sqrt{(J+M)\,(J-M)}}{\sqrt{(2J+1)\,(2J-1)}} \tag{A.39}$$

$$\langle {}^3\Pi_0^{e/f}, J+1|H_{\rm Z}|{}^3\Pi_0^{f/e}, J\rangle = (g_L-g_S)\,\mathcal{H}\mu_{\rm B}\frac{\sqrt{(J+M+1)\,(J-M+1)}}{\sqrt{(2J+1)\,(2J+3)}} \tag{A.40}$$

$$\langle {}^3\Pi_1^{e/f}, J-1|H_{\rm Z}|{}^3\Pi_1^{f/e}, J\rangle = g_L\mathcal{H}\mu_{\rm B}\frac{\sqrt{(J+1)\,(J-1)\,(J+M)\,(J-M)}}{J\sqrt{(2J+1)\,(2J-1)}} \tag{A.41}$$

$$\langle {}^3\Pi_1^{e/f}, J+1|H_{\rm Z}|{}^3\Pi_1^{f/e}, J\rangle = g_L\mathcal{H}\mu_{\rm B}\frac{\sqrt{J\,(J+2)\,(J+M+1)\,(J-M+1)}}{(J+1)\sqrt{(2J+1)\,(2J+3)}} \tag{A.42}$$

$$\langle {}^3\Pi_2^{e/f}, J-1|H_{\rm Z}|{}^3\Pi_2^{f/e}, J\rangle = (g_L+g_S)\,\mathcal{H}\mu_{\rm B}\frac{\sqrt{(J+2)\,(J-2)\,(J+M)\,(J-M)}}{J\sqrt{(2J+1)\,(2J-1)}} \tag{A.43}$$

$$\langle {}^3\Pi_2^{e/f}, J+1|H_{\rm Z}|{}^3\Pi_2^{f/e}, J\rangle = (g_L+g_S)\,\mathcal{H}\mu_{\rm B}\frac{\sqrt{(J+3)\,(J-1)\,(J+M+1)\,(J-M+1)}}{(J+1)\sqrt{(2J+1)\,(2J+3)}} \tag{A.44}$$

$$\langle {}^3\Pi_1^{e/f}, J+1|H_{\rm Z}|{}^3\Pi_0^{f/e}, J\rangle = -\frac{g_S}{\sqrt{2}}\mathcal{H}\mu_{\rm B}\frac{\sqrt{(J+1)\,(J+2)\,(J+M+1)\,(J-M+1)}}{(J+1)\sqrt{(2J+1)\,(2J+3)}} \tag{A.45}$$

Table A.1: Spectroscopic constants used in this calculation in cm^{-1}.

Constant	$X^3\Sigma^-$	$A^3\Pi_i$
B_0	16.3433	16.3215
A_0	-	-34.6198
λ_0	0.9199	-0.1997
γ_0	-0.0549	0.0298

$$\langle {}^3\Pi_1^{e/f}, J|H_Z|{}^3\Pi_0^{e/f}, J\rangle = \frac{g_S}{\sqrt{2}}\mathcal{H}\mu_B\frac{M}{\sqrt{J\,(J+1)}} \quad (A.46)$$

$$\langle {}^3\Pi_1^{e/f}, J-1|H_Z|{}^3\Pi_0^{f/e}, J\rangle = \frac{g_S}{\sqrt{2}}\mathcal{H}\mu_B\frac{\sqrt{J\,(J-1)\,(J+M)\,(J-M)}}{J\sqrt{(2J+1)\,(2J-1)}} \quad (A.47)$$

$$\langle {}^3\Pi_2^{e/f}, J+1|H_Z|{}^3\Pi_1^{f/e}, J\rangle = -\frac{g_S}{\sqrt{2}}\mathcal{H}\mu_B\frac{\sqrt{(J+2)\,(J+3)\,(J+M+1)\,(J-M+1)}}{(J+1)\sqrt{(2J+1)\,(2J+3)}} \quad (A.48)$$

$$\langle {}^3\Pi_2^{e/f}, J|H_Z|{}^3\Pi_1^{e/f}, J\rangle = \frac{g_S}{\sqrt{2}}\mathcal{H}\mu_B\frac{M\sqrt{(J-1)\,(J+2)}}{J\,(J+1)} \quad (A.49)$$

$$\langle {}^3\Pi_2^{e/f}, J-1|H_Z|{}^3\Pi_1^{f/e}, J\rangle = \frac{g_S}{\sqrt{2}}\mathcal{H}\mu_B\frac{\sqrt{(J-1)\,(J-2)\,(J+M)\,(J-M)}}{J\sqrt{(2J+1)\,(2J-1)}} \quad (A.50)$$

A.3 Results

The total Hamiltonian developed in Sections A.1 and A.2 was diagonalized numerically to yield the Zeeman energies of the $X^3\Sigma^-$ and $A^3\Pi_i$ states of NH as a function of applied magnetic field. The spectroscopic constants used in this calculation[153, 27] can be found in Table A.1.

Figures A.1, A.2, and A.3 show the Zeeman shifts calculated by numerical diagonalization of the Hamiltonian. The rotational ground level ($N'' = 0$) of the $X^3\Sigma^-$

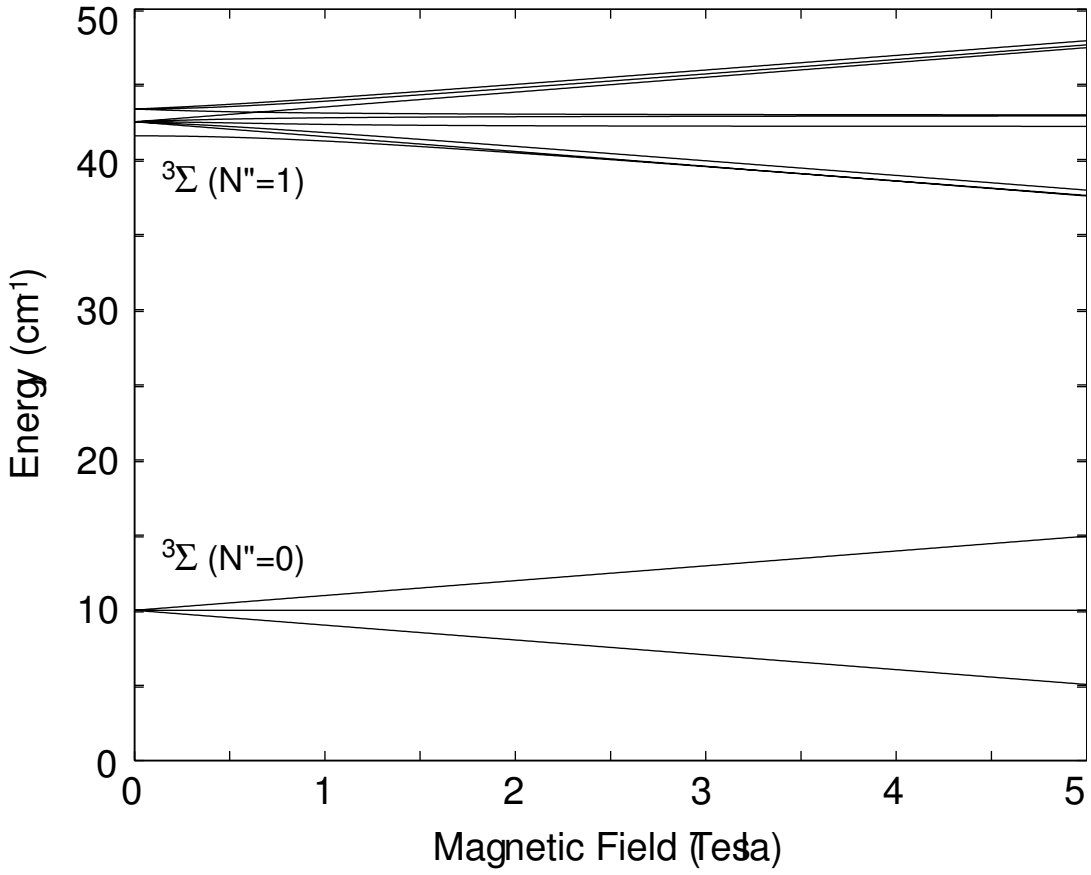

Figure A.1: Zeeman shift of the two lowest rotational levels of the $X^3\Sigma^-$ state of NH.

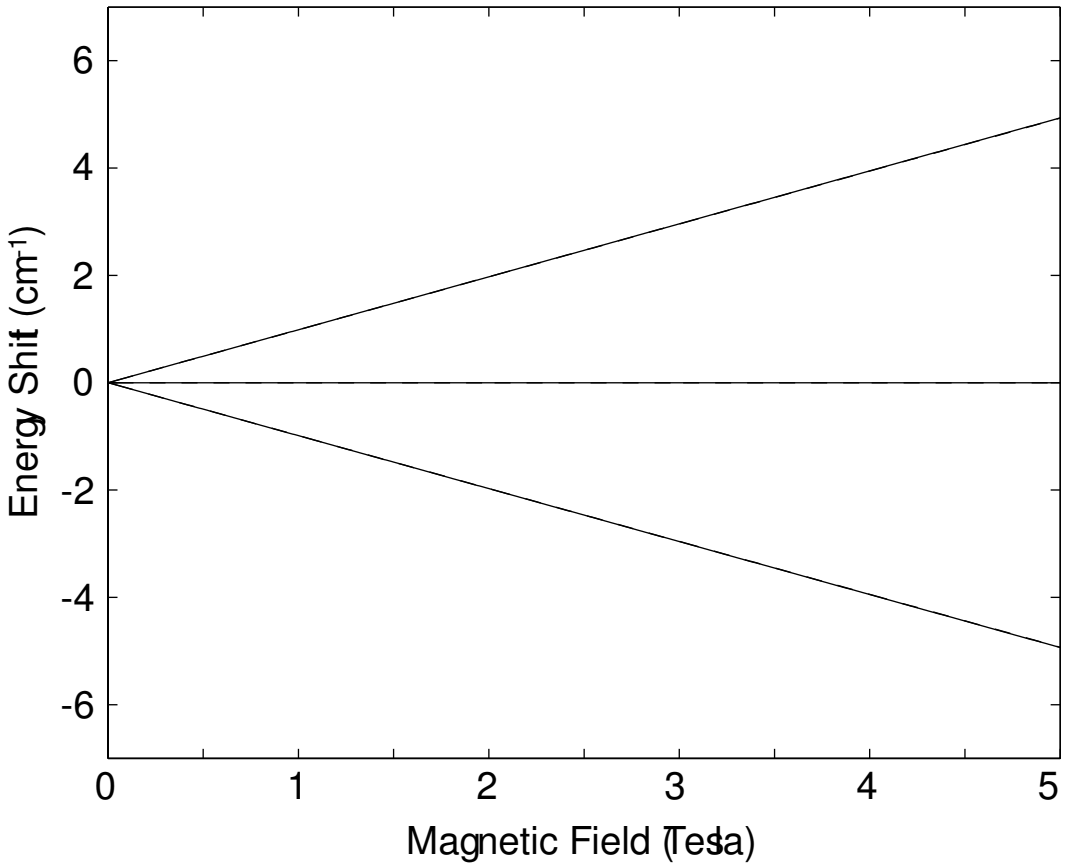

Figure A.2: Zeeman shift of the $X^3\Sigma^-$ rotational ground state of NH. Solid curves are the results of this calculation, dashed curves are from Equation (3.1) and represent $\mu_{\rm eff} = 2\mu_{\rm B}$.

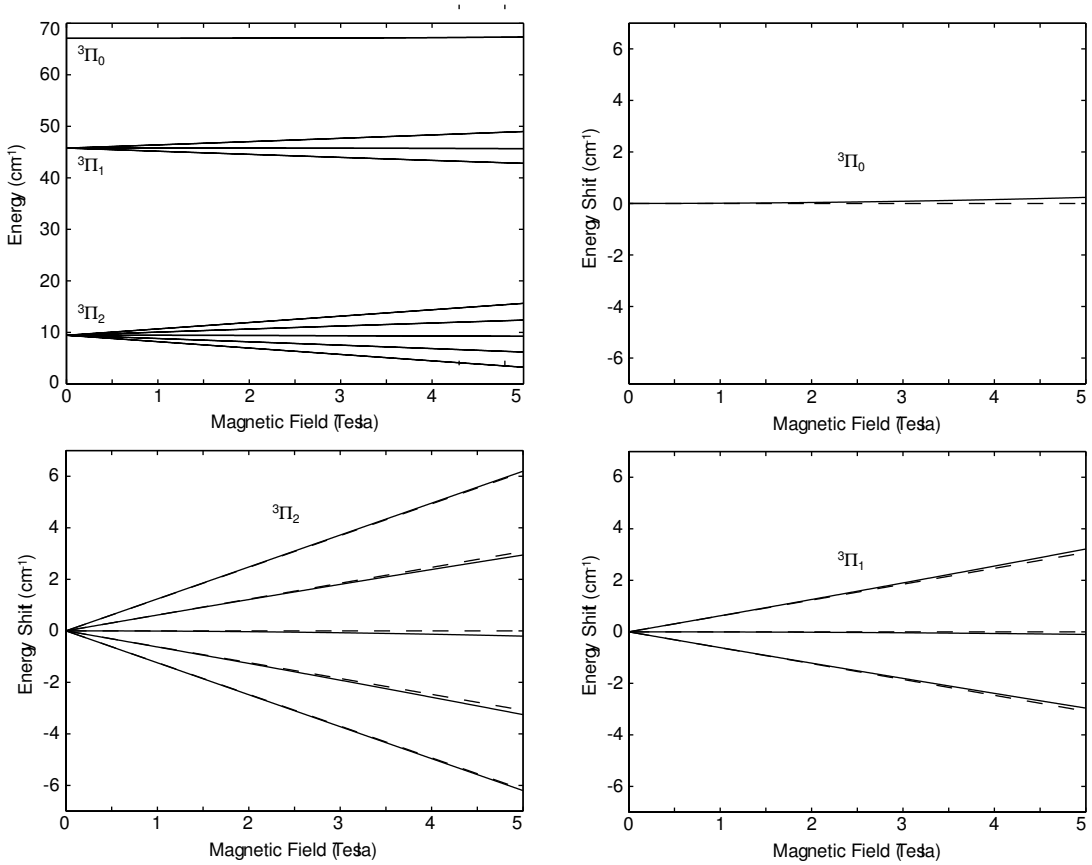

Figure A.3: Zeeman shift of the A$^3\Pi$ rotational ground state of NH. Solid curves are the results of this calculation, dashed curves are from Equation (3.1) and represent $\mu_{\rm eff} = \frac{5}{2}, \frac{5}{4}$, and 0 $\times \mu_{\rm B}$ for the $^3\Pi_2$,$^3\Pi_1$, and $^3\Pi_0$ states respectively.

state agrees almost exactly with Equation (3.1) and remains linear to fields of a few Tesla. The Zeeman Hamiltonian can mix some of the $N'' = 1$ rotationally excited state with the ground state, but the rotational constant (Table A.1) is significantly larger than the energy shift due to the magnetic field (Figure A.2) for NH in this regime and the mixing is therefore minimal.

The rotational ground states of the $A^3\Pi$ manifold show deviations from linearity at high field due to mixing of states with $\Delta N = 0$ and $\Delta\Omega = \pm 1$ as well as $\Delta N = \pm 1$ and $\Delta\Omega = 0$. The former are dominant for the $^3\Pi_2$ ground rotational level while the latter are also significant for $^3\Pi_0$.

Appendix B

Hyperfine Effect in NH

Below 2K the Doppler broadening in NH becomes comparable to the splitting of states due to interactions between the nuclear structure and the electronic and rotational states of the molecule. This *hyperfine splitting* of the levels becomes important at low temperatures for accurate modeling of the spectrum. The matrix elements are derived using spherical tensor methods and the results are in agreement with published data to within 10%.

B.1 Nuclear Hyperfine Hamiltonian

The hyperfine Hamiltonian can be written as the sum of four terms:

$$H_{\rm hf} = H_{\rm dip} + H_{\rm fc} + H_{\rm IL} + H_{\rm Q}. \tag{B.1}$$

The first two terms are the nuclear dipole-electron dipole and Fermi contact interactions. These terms arise from the interaction of electron spin magnetic dipoles with

nuclear spin magnetic dipoles. The third term represents the interaction between a magnetic field caused by nonzero electron orbital angular momentum and nuclear magnetic dipole moments. The last term arises when a nucleus has a nonzero electric quadrupole moment that interacts with the electric field gradient caused by the other charges in the molecule.

B.1.1 Dipole-Dipole

Jackson [101] gives the classical Hamiltonian of the nuclear dipole-electron dipole interaction as

$$H_{\text{clas}} = \frac{\mu_o}{4\pi}\left[\frac{\boldsymbol{\mu}_e \cdot \boldsymbol{\mu}_N}{r^3} - \frac{3(\boldsymbol{\mu}_e \cdot \mathbf{r})(\boldsymbol{\mu}_N \cdot \mathbf{r})}{r^5} - \frac{8\pi}{3}\boldsymbol{\mu}_e \cdot \boldsymbol{\mu}_N \delta(\mathbf{r})\right] \tag{B.2}$$

where $\boldsymbol{\mu}_e$ and $\boldsymbol{\mu}_N$ are the electron spin and nuclear spin magnetic dipole moments, respectively. The first two terms will be called the dipole-dipole hyperfine interaction and will be recast into quantum operator form in H_{dip}. If we use the convention that the electron g-factor is positive, we can write the spin and nuclear magnetic moments in terms of quantum mechanical operators as

$$\boldsymbol{\mu}_e = -\mathrm{g}_e \mu_{\mathrm{B}} \mathbf{S} \tag{B.3}$$

$$\boldsymbol{\mu}_{Nk} = \mathrm{g}_N \mu_{\mathrm{N}} \mathbf{I}_k \tag{B.4}$$

where $\mathbf{S}$ is the total spin operator for the molecule, $\mathbf{I}_k$ is the total nuclear spin operator for nucleus k and $\mu_{\mathrm{B}} \equiv \hbar e/2m_e$ is the Bohr magneton. We can now write the quantum mechanical form of the dipole-dipole hyperfine Hamiltonian as

$$H_{\text{dip}} = -\mathrm{g}_e \mu_{\text{B}} \mathrm{g}_N \mu_{\text{N}} \frac{\mu_o}{4\pi} \sum_k \left[\frac{\mathbf{I}_k \cdot \mathbf{S}}{r_k^3} - \frac{3(\mathbf{I}_k \cdot \mathbf{r}_k)(\mathbf{S} \cdot \mathbf{r}_k)}{r_k^5} \right] \tag{B.5}$$

where r_k is the distance between the electron and nucleus k.

The process of evaluating matrix elements in the system of coupled angular momenta that is the molecule can often be made simpler by expressing operators in terms of irreducible spherical tensor operators. Zare [208] as well as Brown and Carrington [31] provide excellent introductions to spherical tensor operators and give explicit formulas for their use with the Wigner Eckart theorem. Brown and Carrington show that Equation (B.5) can be written in terms of irreducible spherical tenor operators as

$$H_{\text{dip}} = -\sqrt{10} \mathrm{g}_e \mu_{\text{B}} \mathrm{g}_N \mu_{\text{N}} \frac{\mu_o}{4\pi} \sum_k \mathsf{T}^1(\mathbf{I}_k) \cdot \mathsf{T}^1(\mathbf{S}, \mathbf{C}_k^2). \tag{B.6}$$

If we express Equation (B.6) in terms of Cartesian tensor components it can be shown that it is entirely equivalent to Equation (B.5). Furthermore, Brown and Carrington provide a third equivalent form for the dipole-dipole hyperfine Hamiltonian:

$$H_{\text{dip}} = \sqrt{6} \mathrm{g}_e \mu_{\text{B}} \mathrm{g}_N \mu_{\text{N}} \frac{\mu_o}{4\pi} \sum_k \mathsf{T}^2(\mathbf{C}_k) \cdot \mathsf{T}^2(\mathbf{I}_k, \mathbf{S}) \tag{B.7}$$

where we are using the shorthand that

$$\mathsf{T}_q^2(\mathbf{C}_k) \equiv \sqrt{\frac{4\pi}{5}} \mathrm{Y}_{2,q}(\theta, \phi) \frac{1}{r_k^3}. \tag{B.8}$$

This is essentially the same form used for the electron spin-spin interaction in Appendix C.

B.1.2 Fermi Contact

The third term in Equation (B.2) is called the Fermi contact term and only contributes when there is finite overlap of the electron wavefunction with the nucleus, *i.e.* when there is any s-character to the electronic orbital. Using the same procedure as in the previous section, we can rewrite this in terms of quantum operators as

$$H_{\mathrm{fc}} = \mathrm{g}_e \mu_{\mathrm{B}} \mathrm{g}_N \mu_{\mathrm{N}} \frac{2\mu_o}{3} \sum_k \mathbf{I}_k \cdot \mathbf{S}\, \delta(\mathbf{r}_k). \tag{B.9}$$

In terms of spherical tensors,

$$H_{\mathrm{fc}} = \mathrm{g}_e \mu_{\mathrm{B}} \mathrm{g}_N \mu_{\mathrm{N}} \frac{2\mu_o}{3} \sum_k \mathsf{T}^1(\mathbf{I}_k) \cdot \mathsf{T}^1(\mathbf{S})\, \delta(\mathbf{r}_k). \tag{B.10}$$

B.1.3 Orbital Hyperfine Interaction

If the molecule has nonzero electron orbital angular momentum there will be an interaction between the magnetic field created by the electron's motion at the nucleus and the nuclear spin. The magnetic field produced at the center of a circular loop of current I of radius r is given by

$$B = \frac{\mu_o I}{2r}. \tag{B.11}$$

In a molecule, this current can be modeled as an electron orbiting the nucleus with orbital angular momentum L. The frequency of this orbit will be given by

$$f = \frac{L}{2\pi m_e r^2} \tag{B.12}$$

so that the current ef can be inserted into Equation B.11 to give the classical magnetic field in terms of the orbital angular momentum of the electron:

$$\boldsymbol{B} = 2\frac{\mu_o}{4\pi}\frac{e}{2m_e}\frac{\boldsymbol{L}}{r^3}. \tag{B.13}$$

The energy of a nuclear magnetic dipole in this field will be

$$W = \boldsymbol{\mu}_N \cdot \boldsymbol{B} \tag{B.14}$$

so that when we combine this with Equation B.4 and convert classical quantities into quantum operators we get

$$H_{\mathrm{IL}} = 2\mu_{\mathrm{B}} g_N \mu_{\mathrm{N}} \frac{\mu_o}{4\pi} \sum_k \frac{\mathsf{T}^1(\mathbf{I}_k) \cdot \mathsf{T}^1(\mathbf{L})}{r_k^3}. \tag{B.15}$$

B.1.4 Electric Quadrupole

The classical electric potential of a charge density $\rho(\mathbf{r})$ is given by

$$V(\mathbf{r}) = \frac{1}{4\pi\epsilon_o}\int \frac{\rho(\mathbf{r}')}{|\mathbf{r}-\mathbf{r}'|}\mathrm{d}^3r'. \tag{B.16}$$

Jackson [101] gives the energy of a configuration of charges in a potential as

$$W = \frac{1}{2}\int \rho(\mathbf{r})V(\mathbf{r})\mathrm{d}^3r. \tag{B.17}$$

The energy required to put a nuclear charge density $\rho_p(\mathbf{r}_p)$ in an electrostatic potential created by an electron density $\rho_e(\mathbf{r}_e)$ is therefore given by

$$W = \frac{1}{4\pi\epsilon_o}\int \rho_p(\mathbf{r}_p)\int \frac{\rho_e(\mathbf{r}_e)}{|\mathbf{r}_p-\mathbf{r}_e|}\mathrm{d}^3r_e\mathrm{d}^3r_p. \tag{B.18}$$

Following Zare, [208] we can expand this in terms of modified spherical harmonics by identifying

$$\frac{1}{|\mathbf{r}_p - \mathbf{r}_e|} = \sum_l \frac{r_p^l}{r_e^{l+1}} \mathbf{C}^l(\theta_e, \phi_e) \cdot \mathbf{C}^l(\theta_p, \phi_p). \tag{B.19}$$

We now have

$$W = \frac{1}{4\pi\epsilon_o} \sum_l \int \rho_p(\mathbf{r}_p) \mathbf{C}^l(\theta_p, \phi_p) r_p^l \cdot \int \frac{\rho_e(\mathbf{r}_e) \mathbf{C}^l(\theta_e, \phi_e)}{r_e^{l+1}} \mathrm{d}^3 r_e \mathrm{d}^3 r_p. \tag{B.20}$$

Equation (B.20) is a multipole expansion of the interaction energy between charge distributions in the molecule. We are here interested in the $l = 2$ component, which represents a nuclear electric quadrupole moment interacting with the electric field gradient at the nucleus. To cast this in quantum mechanical form we will replace the integrals over continuous charge distributions with sums over individual electron and proton position operators and take only the $l = 2$ component:

$$H = -\frac{e^2}{4\pi\epsilon_o} \sum_{e,p} \mathbf{C}^2(\theta_p, \phi_p) r_p^2 \cdot \frac{\mathbf{C}^2(\theta_e, \phi_e)}{r_e^3}. \tag{B.21}$$

If we make the following definitions

$$\mathsf{T}^2(\nabla \mathbf{E}) \equiv -\frac{e}{4\pi\epsilon_o} \sum_e \frac{\mathbf{C}^2(\theta_e, \phi_e)}{r_e^3}. \tag{B.22}$$

$$\mathsf{T}^2(\mathbf{Q}) \equiv \sum_p \mathbf{C}^2(\theta_p, \phi_p) r_p^2 \tag{B.23}$$

we can write the electric quadrupole hyperfine Hamiltonian as

$$H_{\mathrm{Q}} = -e\, \mathsf{T}^2(\nabla \mathbf{E}) \cdot \mathsf{T}^2(\mathbf{Q}). \tag{B.24}$$

This is sometimes rewritten in terms of nuclear spin operators as

$$H_{\mathrm{Q}} = eq_o Q \frac{\sqrt{6}}{4I(2I-1)} \mathsf{T}^2_{q=0}(\mathbf{I}, \mathbf{I}) \tag{B.25}$$

Table B.1: Momenta used in the hyperfine calculation

Operator	Meaning
$\mathbf{S}$	Total electronic spin ($S = 1$ in NH)
$\mathbf{R}$	Rotational angular momentum
$\mathbf{\Lambda}$	Electron orbital angular momentum along internuclear axis
$\mathbf{N}$	Rotation plus orbital projection ($\mathbf{N} = \mathbf{R} + \mathbf{\Lambda}$)
$\mathbf{J}$	Total angular momentum exclusive of nuclear spin ($\mathbf{J} = \mathbf{N} + \mathbf{S}$)
$\mathbf{I}_{\mathrm{N}}$	Nuclear spin of nitrogen nucleus (for ^{14}N, $I_{\mathrm{N}} = 1$)
$\mathbf{I}_{\mathrm{H}}$	Nuclear spin of hydrogen nucleus (for ^{1}H, $I_{\mathrm{H}} = 1/2$)
$\mathbf{T}$	Total nuclear spin ($\mathbf{T} = \mathbf{I}_{\mathrm{N}} + \mathbf{I}_{\mathrm{H}}$)
$\mathbf{F}$	Total angular momentum of the molecule ($\mathbf{F} = \mathbf{J} + \mathbf{T}$)

where q_o is the negative of the expectation value of the electric field gradient and q denotes the molecule-fixed reference frame (p will be used for lab-fixed components).

We can now write the complete Hamiltonian in terms of irreducible spherical tensor operators:

$$\begin{aligned} H_{\mathrm{hf}} &= -\sqrt{10}\mathrm{g}_e\mu_{\mathrm{B}}\mathrm{g}_N\mu_{\mathrm{N}}\frac{\mu_o}{4\pi}\sum_k \mathsf{T}^1(\mathbf{I}_k)\cdot\mathsf{T}^1(\mathbf{S},\mathbf{C}^2_k) \\ &+ \mathrm{g}_e\mu_{\mathrm{B}}\mathrm{g}_N\mu_{\mathrm{N}}\frac{2\mu_o}{3}\sum_k \mathsf{T}^1(\mathbf{I}_k)\cdot\mathsf{T}^1(\mathbf{S})\,\delta(\mathbf{r}_k) \\ &+ 2\mu_{\mathrm{B}}\mathrm{g}_N\mu_{\mathrm{N}}\frac{\mu_o}{4\pi}\sum_k \frac{\mathsf{T}^1(\mathbf{I}_k)\cdot\mathsf{T}^1(\mathbf{L})}{r_k^3} \\ &- e\sum_k \mathsf{T}^2(\nabla\mathbf{E})\cdot\mathsf{T}^2(\mathbf{Q}_k). \end{aligned} \tag{B.26}$$

B.1.5 Coupling Scheme

There are many ways to couple the various angular momenta in molecules. Table B.1 lists the momenta used in this calculation.

Some authors prefer to couple the nuclear spins sequentially to J since there is

often one nucleus whose coupling to the molecule dominates the hyperfine shifts, but we have chosen here to separate the nuclear spins from J at the same time. Results of calculations using these two methods will be identical and this is only a matter calculational and intuitive convenience.

To determine which states exist for a particular set of quantum numbers we can add up the momenta sequentially. For instance, we will here be working with the dominant isotopomer ^{14}N^{1}H, which can have two different values of total nuclear spin, $T = \frac{1}{2}, \frac{3}{2}$. That means that for a given value of J, there will be one state each[1] of $F = J \pm \frac{3}{2}$ and two states each of $F = J \pm \frac{1}{2}$ corresponding to different values of T. Furthermore, the hyperfine interaction will mix the states with the same F but different T, so T will not be a good quantum number. We will need to include the matrix elements that are off-diagonal in T and diagonalize the Hamiltonian to get accurate values for the hyperfine splittings.

B.2 Nuclear Hyperfine Matrix Elements

To evaluate the matrix elements of $H_{\rm hf}$ we can use the Wigner Eckart theorem as stated by Zare [208]. In order to evaluate matrix elements of lab-fixed and molecule-fixed operators it will be helpful to restate the relationship between them explicitly. For an irreducible spherical tensor operator $\mathsf{T}^k_p(\mathbf{O})$, the lab-fixed p component can be written in terms of molecule-fixed q components as

$$\mathsf{T}^k_p(\mathbf{O}) = \sum_q \mathcal{D}^k_{pq}(\omega)^* \mathsf{T}^k_q(\mathbf{O}) \tag{B.27}$$

[1] except for $J = 1$, which will not have $F = J - 3/2$

where $\mathcal{D}^k(\omega)$ is the Wigner rotation matrix through Euler angles $\omega \equiv (\phi, \theta, \chi)$. Likewise, to express molecule-fixed (q) components in terms of lab-fixed (p) components we can write

$$\mathsf{T}^k_q(\mathbf{O}) = \sum_p \mathcal{D}^k_{pq}(\omega)\mathsf{T}^k_p(\mathbf{O}). \tag{B.28}$$

The integration over all angles ω takes a particularly simple form since the symmetric top wavefunctions of the molecule can be written in terms of the Wigner rotation matrix as

$$|N, \Lambda, M_N\rangle = \sqrt{\frac{(2N+1)}{8\pi^2}}\mathcal{D}^N_{M_N,\Lambda}(\omega)^*. \tag{B.29}$$

The reduced matrix elements will be given by

$$\langle N, \Lambda \| \mathcal{D}^k_{.q}(\omega)^* \| N', \Lambda' \rangle = (-1)^{N-\Lambda} \begin{pmatrix} N & k & N' \\ -\Lambda & q & \Lambda' \end{pmatrix} \sqrt{(2N+1)(2N'+1)} \tag{B.30}$$

where the term in parenthesis is a Wigner-3j symbol. An excellent introduction to Wigner 3-,6-, and 9-j symbols has been provided by Zare. [208]

B.2.1 $H_{\mathbf{dip}}$ Matrix Elements

The dipole-dipole interaction (the first line of Equation (B.26)) will have matrix elements that are proportional to

$$\langle T, F, M_F | \mathsf{T}^1(\mathbf{I}) \cdot \mathsf{T}^1(\mathbf{S}, \mathbf{C}^2) | T', F, M_F \rangle \tag{B.31}$$

Since $\mathsf{T}^1(\mathbf{I})$ operates on the nuclear spin part of the Hamiltonian and $\mathsf{T}^1(\mathbf{S})$ and $\mathsf{T}^2(\mathbf{C})$ operate on the spin and rotational parts respectively, we can use the Wigner

Eckart theorem to separate F into J and T to get

$$\begin{aligned}\langle T, F, M_F|\mathsf{T}^1(\mathbf{I})\cdot\mathsf{T}^1(\mathbf{S},\mathbf{C}^2)|T', F, M_F\rangle &= (-1)^{T+J+F}\left\{\begin{array}{ccc} T & J & F \\ J & T' & 1\end{array}\right\} \\ &\times\langle T\|\mathsf{T}^1(\mathbf{I})\|T'\rangle\langle J\|\mathsf{T}^1(\mathbf{S},\mathbf{C}^2)\|J\rangle\end{aligned} \tag{B.32}$$

To evaluate the nuclear spin reduced matrix elements we need to decouple T into $I_{\rm N}$ and $I_{\rm H}$:

$$\sum_k\langle T\|\mathsf{T}^1(\mathbf{I}_k)\|T'\rangle = \langle T\|\mathsf{T}^1(\mathbf{I}_{\rm N})\|T'\rangle + \langle T\|\mathsf{T}^1(\mathbf{I}_{\rm H})\|T'\rangle$$

$$= (-1)^{I_{\rm N}+I_{\rm H}+T'+1}\sqrt{(2T'+1)(2T+1)}\left\{\begin{array}{ccc} I_{\rm N} & T & I_{\rm H} \\ T' & I_{\rm N} & 1\end{array}\right\}\langle I_{\rm N}\|\mathsf{T}^1(\mathbf{I}_{\rm N})\|I_{\rm N}\rangle \tag{B.33}$$

$$+(-1)^{I_{\rm N}+I_{\rm H}+T+1}\sqrt{(2T'+1)(2T+1)}\left\{\begin{array}{ccc} I_{\rm H} & T & I_{\rm N} \\ T' & I_{\rm H} & 1\end{array}\right\}\langle I_{\rm H}\|\mathsf{T}^1(\mathbf{I}_{\rm H})\|I_{\rm H}\rangle \tag{B.34}$$

where we can identify the reduced matrix elements

$$\langle I_k\|\mathsf{T}^1(\mathbf{I}_k)\|I_k\rangle = \sqrt{(2I_k+1)I_k(I_k+1)}. \tag{B.35}$$

Note that for $T \neq T'$, lines (B.33) and (B.34) can have opposite signs.

Since $\mathbf{S}$ acts only on the spin part of the wavefunction and $\mathbf{C}_k^2$ does not, we can split up the second reduced matrix element in Equation (B.32) by separating J into S and N:

$$\langle J\|\mathsf{T}^1(\mathbf{S},\mathbf{C}_k^2)\|J\rangle = \sqrt{3}\,(2J+1)\left\{\begin{array}{ccc} S & N & J \\ 1 & 2 & 1 \\ S & N & J\end{array}\right\}\langle S\|\mathsf{T}^1(\mathbf{S})\|S\rangle\langle N,\Lambda\|\mathsf{T}^2(\mathbf{C}_k)\|N,\Lambda\rangle. \tag{B.36}$$

The first reduced matrix element can be evaluated in the same form as Equation (B.35). To evaluate the second reduced matrix element it will be helpful to look at the form of the hyperfine constant that we will be taking from literature for our calculation. The dipole-dipole hyperfine coupling constant we will use for our calculation is defined by Wayne and Radford [194] as

$$t_k \equiv \mathrm{g}_e \mu_\mathrm{B} \mathrm{g}_N \mu_\mathrm{N} \frac{\mu_o}{4\pi} \sum_i \left\langle \frac{(3\cos^2(\theta_{ik}) - 1)}{2r_{ik}^3} \right\rangle \tag{B.37}$$

where the sum of i runs over all unpaired electrons and θ_{ik} is the angle between the internuclear axis and the ith unpaired electron. This quantity is clearly defined in the molecule-fixed axis system, so it will be helpful for us to write our reduced matrix element in terms of q:

$$\langle N, \Lambda \| \mathsf{T}^2(\mathbf{C}_k) \| N, \Lambda \rangle = \langle N, \Lambda \| \sum_q \mathcal{D}^2_{.q}(\omega)^* \mathsf{T}^2_q(\mathbf{C}_k) \| N, \Lambda \rangle \tag{B.38}$$

where the . in the subscript of the Wigner rotation matrix reminds us that this quantity has already had its lab-frame (p) orientation dependence separated out via the Wigner Eckart theorem. If we insert the projection operator to separate the two terms we get

$$\sum_{N'', \Lambda''} \langle N, \Lambda \| \sum_q \mathcal{D}^2_{.q}(\omega)^* \| N'', \Lambda'' \rangle \langle N'', \Lambda'' \| \mathsf{T}^2_q(\mathbf{C}_k) \| N, \Lambda \rangle. \tag{B.39}$$

The diagonal $q = 0$ component of the second reduced matrix element is

$$\langle N, \Lambda \| \mathsf{T}^2_{q=0}(\mathbf{C}_k) \| N, \Lambda \rangle = \left\langle \frac{(3\cos^2(\theta_k) - 1)}{2r_k^3} \right\rangle, \tag{B.40}$$

so we will set $q = 0$ and $N'' = N$,$\Lambda'' = \Lambda$ to write our answer in terms of the constant t_k. In general there are other correction terms corresponding to $q = \pm 1, \pm 2$, etc. but

we will neglect these in our calculation since they connect Λ-doublet states, which do not occur in the ground state of NH. Now we can evaluate

$$\langle N,\Lambda\|\sum_q \mathcal{D}^2_{.q=0}(\omega)^*\|N,\Lambda\rangle = (-1)^{N-\Lambda}(2N+1)\begin{pmatrix} N & 2 & N \\ -\Lambda & 0 & \Lambda \end{pmatrix} \tag{B.41}$$

to give us

$$\langle N,\Lambda\|\mathsf{T}^2(\mathbf{C}_k)\|N,\Lambda\rangle = (-1)^{N-\Lambda}(2N+1)\begin{pmatrix} N & 2 & N \\ -\Lambda & 0 & \Lambda \end{pmatrix}\left\langle \frac{(3\cos^2(\theta_k)-1)}{2r_k^3}\right\rangle. \tag{B.42}$$

Combining the various parts of this calculation results in an expression for the matrix elements of the dipole-dipole hyperfine Hamiltonian:

$$\begin{aligned}
&\langle T,F,M_F|H_{\rm dip}|T',F,M_F\rangle = \\
&\quad -\sqrt{30}(-1)^{T+J+N+F-\Lambda+1}(2J+1)(2N+1)\sqrt{(2T'+1)(2T+1)}\sqrt{(2S+1)S(S+1)} \\
&\quad \times\begin{Bmatrix} T & J & F \\ J & T' & 1 \end{Bmatrix}\begin{pmatrix} N & 2 & N \\ -\Lambda & 0 & \Lambda \end{pmatrix}\begin{Bmatrix} S & N & J \\ 1 & 2 & 1 \\ S & N & J \end{Bmatrix} \\
&\quad \times\Bigg[t_{\rm N}(-1)^{I_{\rm N}+I_{\rm H}+T'}\sqrt{(2I_{\rm N}+1)I_{\rm N}(I_{\rm N}+1)}\begin{Bmatrix} I_{\rm N} & T & I_{\rm H} \\ T' & I_{\rm N} & 1 \end{Bmatrix} \\
&\qquad + t_{\rm H}(-1)^{I_{\rm N}+I_{\rm H}+T}\sqrt{(2I_{\rm H}+1)I_{\rm H}(I_{\rm H}+1)}\begin{Bmatrix} I_{\rm H} & T & I_{\rm N} \\ T' & I_{\rm H} & 1 \end{Bmatrix}\Bigg].
\end{aligned}$$

B.2.2 $H_{\mathbf{fc}}$ Matrix Elements

The Fermi contact hyperfine coupling constant given by Wayne and Radford[194] is defined by

$$b_{Fk} \equiv \sum_i \mathrm{g}_e \mu_\mathrm{B} \mathrm{g}_N \mu_\mathrm{N} \frac{\mu_o}{3} \psi_i^2(r_k = 0) \tag{B.43}$$

where the sum on i again extends over all unpaired electrons. This term will clearly arise directly from the spatial part of the integration over the $\delta(\mathbf{r})$ in the Fermi contact Hamiltonian, so we can focus our attention on the scalar product

$$\langle T, F, M_F | \mathsf{T}^1(\mathbf{I}) \cdot \mathsf{T}^1(\mathbf{S}) | T', F, M_F \rangle. \tag{B.44}$$

We can first split F into J and T using the Wigner Eckart theorem:

$$\begin{aligned} \sum_k \langle T, F, M_F | \mathsf{T}^1(\mathbf{I}_k) \cdot \mathsf{T}^1(\mathbf{S}) | T', F, M_F \rangle &= (-1)^{T+J+F} \left\{ \begin{array}{ccc} T & J & F \\ J & T' & 1 \end{array} \right\} \\ &\quad \times \sum_k \langle T \| \mathsf{T}^1(\mathbf{I}_k) \| T' \rangle \langle J \| \mathsf{T}^1(\mathbf{S}) \| J \rangle \end{aligned} \tag{B.45}$$

The nuclear spin term has been evaluated in the previous section, so the only new term here is $\langle J \| \mathsf{T}^1(\mathbf{S}) \| J \rangle$, which can be evaluated by decoupling J into S and N:

$$\begin{aligned} \langle J \| \mathsf{T}^1(\mathbf{S}) \| J \rangle &= (-1)^{N+S+J+1} (2J+1) \left\{ \begin{array}{ccc} S & J & N \\ J & S & 1 \end{array} \right\} \langle S \| \mathsf{T}^1(\mathbf{S}) \| S \rangle \\ &= (-1)^{N+S+J+1} (2J+1) \left\{ \begin{array}{ccc} S & J & N \\ J & S & 1 \end{array} \right\} \sqrt{(2S+1)S(S+1)} \end{aligned} \tag{B.46}$$

Putting this calculation together with Equation (B.43) yields the matrix elements of the Fermi contact interaction:

$$\langle T, F, M_F | H_{\mathrm{fc}} | T', F, M_F \rangle =$$

$$(-1)^{2J+T+F+N+S}(2J+1)\sqrt{(2S+1)S(S+1)}\sqrt{(2T'+1)(2T+1)}$$
$$\times\left\{\begin{array}{ccc} T & J & F \\ J & T' & 1 \end{array}\right\}\left\{\begin{array}{ccc} S & J & N \\ J & S & 1 \end{array}\right\}$$
$$\times\left[b_{F\mathrm{N}}(-1)^{I_\mathrm{N}+I_\mathrm{H}+T'}\sqrt{(2I_\mathrm{N}+1)I_\mathrm{N}(I_\mathrm{N}+1)}\left\{\begin{array}{ccc} I_\mathrm{N} & T & I_\mathrm{H} \\ T' & I_\mathrm{N} & 1 \end{array}\right\}\right.$$
$$\left.+\,b_{F\mathrm{H}}(-1)^{I_\mathrm{N}+I_\mathrm{H}+T}\sqrt{(2I_\mathrm{H}+1)I_\mathrm{H}(I_\mathrm{H}+1)}\left\{\begin{array}{ccc} I_\mathrm{H} & T & I_\mathrm{N} \\ T' & I_\mathrm{H} & 1 \end{array}\right\}\right].$$

B.2.3 H_{IL} Matrix Elements

While H_{IL} will vanish to first order for the ground state of NH, the $A^3\Pi$ excited state has nonzero electron orbital angular momentum which will cause hyperfine shifts of the transition frequencies. The orbital hyperfine coupling constant for nucleus k is defined by Ubachs *et al.*[186] as

$$a_k \equiv \mathrm{g}_e\mu_\mathrm{B}\mathrm{g}_N\mu_\mathrm{N}\left\langle\frac{1}{r_k^3}\right\rangle_\pi \tag{B.47}$$

where the spatial average is to be taken over the π orbital only. This indicates that the mixing of states of different Λ that the $\mathsf{T}^1(\mathbf{L})$ operator will introduce is to be neglected for this first-order effect. We can begin evaluation of the matrix elements by first decoupling F into T and J:

$$\begin{aligned}\sum_k\langle T,F,M_F|\frac{1}{r_k^3}\mathsf{T}^1(\mathbf{I}_k)\cdot\mathsf{T}^1(\mathbf{L})|T',F,M_F\rangle &= (-1)^{T+J+F}\left\{\begin{array}{ccc} T & J & F \\ J & T' & 1 \end{array}\right\}\\ &\times\langle J\|\mathsf{T}^1(\mathbf{L})\|J\rangle\sum_k\langle T\|\frac{1}{r_k^3}\mathsf{T}^1(\mathbf{I}_k)\|T'\rangle\end{aligned} \tag{B.48}$$

The first reduced matrix element contains an operator that does not depend on the spin part of the wavefunction, so we can separate J into N and S:

$$\langle J\|\mathsf{T}^1(\mathbf{L})\|J\rangle = (-1)^{N+S+J+1}(2J+1)\left\{\begin{array}{ccc} N & J & S \\ J & N & 1 \end{array}\right\}\langle N\|\mathsf{T}^1(\mathbf{L})\|N\rangle \tag{B.49}$$

The basis functions $|N,\Lambda\rangle$ have one well-defined projection of $\mathbf{L}$ in the molecule-fixed reference frame, so we will express this matrix element in terms of molecule-fixed operator components:

$$\langle N\|\mathsf{T}^1(\mathbf{L})\|N\rangle = \sum_q \langle N\|\mathcal{D}^1_{.q}(\omega)^*\mathsf{T}^1_q(\mathbf{L})\|N\rangle. \tag{B.50}$$

These terms can be separated by inserting the projection operator just like Equation B.39. Here we note that since we have decided to consider only the terms that are diagonal in Λ we will ignore all but the $q=0$ component to give us

$$\begin{aligned}\langle N\|\mathsf{T}^1(\mathbf{L})\|N\rangle &= \langle N\|\mathcal{D}^1_{.0}(\omega)^*\|N\rangle\langle N\|\mathsf{T}^1_0(\mathbf{L})\|N\rangle \\ &= (-1)^{N-\Lambda}\left(\begin{array}{ccc} N & 1 & N \\ -\Lambda & 0 & \Lambda \end{array}\right)(2N+1)\Lambda. \end{aligned}\tag{B.51}$$

The last term in Equation B.48 has already been addressed in the calculation for $H_{\rm dip}$ and can be combined with the lines above to give us the matrix elements of the orbital hyperfine Hamiltonian:

$$\langle T,F,M_F|H_{\rm IL}|T',F,M_F\rangle =$$
$$(-1)^{T+2J+2N+F+S-\Lambda}(2J+1)(2N+1)\Lambda\sqrt{(2T'+1)(2T+1)}$$

$$\times \left\{ \begin{array}{ccc} T & J & F \\ J & T' & 1 \end{array} \right\} \left\{ \begin{array}{ccc} N & J & S \\ J & N & 1 \end{array} \right\} \left(\begin{array}{ccc} N & 1 & N \\ -\Lambda & 0 & \Lambda \end{array} \right)$$

$$\times \left[a_{\rm N}(-1)^{I_{\rm N}+I_{\rm H}+T'} \sqrt{(2I_{\rm N}+1)I_{\rm N}(I_{\rm N}+1)} \left\{ \begin{array}{ccc} I_{\rm N} & T & I_{\rm H} \\ T' & I_{\rm N} & 1 \end{array} \right\} \right.$$

$$\left. + a_{\rm H}(-1)^{I_{\rm N}+I_{\rm H}+T} \sqrt{(2I_{\rm H}+1)I_{\rm H}(I_{\rm H}+1)} \left\{ \begin{array}{ccc} I_{\rm H} & T & I_{\rm N} \\ T' & I_{\rm H} & 1 \end{array} \right\} \right].$$

B.2.4 $H_{\rm Q}$ Matrix Elements

The electric quadrupole coupling constant is a product of the electric field gradient at the nucleus and the quadrupole moment of that nucleus, often written as eq_oQ. Their definitions are given mathematically as

$$eQ_k \equiv e\langle I_k, M_{I_k} = I_k | 2 \sum_{p'} C^2_{p=0}(\theta_{kp'}, \phi_{kp'}) r^2_{kp'} | I_k, M_{I_k} = I_k \rangle \tag{B.52}$$

$$= 2 \left(\begin{array}{ccc} I & 2 & I \\ -I & 0 & I \end{array} \right) \langle I_k \| \mathsf{T}^2(\mathbf{Q}_k) \| I_k \rangle \tag{B.53}$$

and

$$q_o \equiv 2 \left\langle \sum_i \frac{e}{4\pi\epsilon_o r_i^3} C^2_{q=0}(\theta_i, \phi_i) \right\rangle \tag{B.54}$$

where the sums over p' and i extend over all the protons and electrons, respectively. Note that the quadrupole moment is defined in the (p) lab-fixed reference frame and the electric field gradient is defined in the (q) molecule-fixed frame. To evaluate the matrix elements of $H_{\rm Q}$ we will need to examine terms of the form

$$\langle T, F, M_F | \mathsf{T}^2(\nabla \mathbf{E}) \cdot \mathsf{T}^2(\mathbf{Q}) | T', F, M_F \rangle. \tag{B.55}$$

Since $\mathsf{T}^2(\nabla\mathbf{E})$ involves electron operators and $\mathsf{T}^2(\mathbf{Q})$ only references nucleon operators we can decouple F as before:

$$\begin{aligned}\langle T, F, M_F|\mathsf{T}^2(\nabla\mathbf{E})\cdot\mathsf{T}^2(\mathbf{Q})|T', F, M_F\rangle &= (-1)^{T+J+F}\left\{\begin{array}{ccc} T & J & F \\ J & T' & 2 \end{array}\right\} \\ &\times\langle J\|\mathsf{T}^2(\nabla\mathbf{E})\|J\rangle\langle T\|\mathsf{T}^2(\mathbf{Q})\|T'\rangle \end{aligned} \quad \text{(B.56)}$$

and since $\mathsf{T}^2(\nabla\mathbf{E})$ is also independent of the spin, we have

$$\langle J\|\mathsf{T}^2(\nabla\mathbf{E})\|J\rangle = (-1)^{N+S+J}(2J+1)\left\{\begin{array}{ccc} S & J & N \\ J & S & 2 \end{array}\right\}\langle N\|\mathsf{T}^2(\nabla\mathbf{E})\|N\rangle. \quad \text{(B.57)}$$

For the dominant isotopomer $^{14}\mathrm{N}^1\mathrm{H}$ the nitrogen nucleus is the only one with a nonzero quadrupole moment, so we have

$$\langle T\|\mathsf{T}^2(\mathbf{Q})\|T'\rangle = (-1)^{I_\mathrm{N}+I_\mathrm{H}+T'}\sqrt{(2T'+1)(2T+1)}\left\{\begin{array}{ccc} I_\mathrm{N} & T & I_\mathrm{H} \\ T' & I_\mathrm{N} & 2 \end{array}\right\}\langle I_\mathrm{N}\|\mathsf{T}^2(\mathbf{Q})\|I_\mathrm{N}\rangle. \quad \text{(B.58)}$$

Combining this with Equation (B.53) gives us

$$\begin{aligned}\langle T\|\mathsf{T}^2(\mathbf{Q})\|T'\rangle &= \frac{eQ}{2}(-1)^{I_\mathrm{N}+I_\mathrm{H}+T'}\sqrt{(2T'+1)(2T+1)} \\ &\times\left\{\begin{array}{ccc} I_\mathrm{N} & T & I_\mathrm{H} \\ T' & I_\mathrm{N} & 2 \end{array}\right\}\left(\begin{array}{ccc} I_\mathrm{N} & 2 & I_\mathrm{N} \\ -I_\mathrm{N} & 0 & I_\mathrm{N} \end{array}\right)^{-1}. \end{aligned} \quad \text{(B.59)}$$

If we examine Equation (B.22) we find that Equation (B.54) can be rewritten in terms of the molecule-fixed ($q = 0$) component of the electric field gradient tensor:

$$q_o = -2\left\langle\mathsf{T}^2_{q=0}(\nabla\mathbf{E})\right\rangle. \quad \text{(B.60)}$$

In order to express our reduced matrix element in this form we must therefore transform into the molecule-fixed frame:

$$\begin{aligned}\langle N\|\mathsf{T}^2(\nabla\mathbf{E})\|N\rangle &= \langle N\|\sum_q \mathcal{D}^2_{\cdot q}(\omega)^*\mathsf{T}^2_q(\nabla\mathbf{E})\|N\rangle \\ &= \langle N\|\sum_q \mathcal{D}^2_{\cdot q}(\omega)^*\|N\rangle\left\langle\mathsf{T}^2_q(\nabla\mathbf{E})\right\rangle. \end{aligned} \tag{B.61}$$

We are interested in the $q=0$ component of this expression, so we are left with

$$\begin{aligned}\langle N\|\mathsf{T}^2(\nabla\mathbf{E})\|N\rangle &= \langle N\|\mathcal{D}^2_{\cdot 0}(\omega)^*\|N\rangle\left\langle\mathsf{T}^2_{q=0}(\nabla\mathbf{E})\right\rangle \\ &= -\frac{q_o}{2}(-1)^{N-\Lambda}(2N+1)\begin{pmatrix} N & 2 & N \\ -\Lambda & 0 & \Lambda\end{pmatrix} \end{aligned} \tag{B.62}$$

and can write down the expression for the quadrupole hyperfine matrix elements:

$$\begin{aligned}&\langle T,F,M_F|H_{\mathrm{Q}}|T',F,M_F\rangle = \\ &\quad -\frac{eq_oQ}{4}(-1)^{2J+2N+T+T'+F+S+I_{\mathrm{N}}+I_{\mathrm{H}}-\Lambda}(2J+1)(2N+1)\sqrt{(2T'+1)(2T+1)} \\ &\quad \times\begin{Bmatrix} T & J & F \\ J & T' & 2\end{Bmatrix}\begin{Bmatrix} S & J & N \\ J & S & 2\end{Bmatrix}\begin{Bmatrix} I_{\mathrm{N}} & T & I_{\mathrm{H}} \\ T' & I_{\mathrm{N}} & 2\end{Bmatrix} \\ &\quad \times\begin{pmatrix} N & 2 & N \\ -\Lambda & 0 & \Lambda\end{pmatrix}\begin{pmatrix} I_{\mathrm{N}} & 2 & I_{\mathrm{N}} \\ -I_{\mathrm{N}} & 0 & I_{\mathrm{N}}\end{pmatrix}^{-1}. \end{aligned} \tag{B.63}$$

B.3 Relevant Hyperfine States and Shifts

The absolute rovibrational and electronic ground state of NH is $X^3\Sigma^-(J''=1,N''=0)$. Our detection happens on the $A\leftarrow X$ transition to $A^3\Pi_2(J'=2,N'=1)$. Literature values for the hyperfine coupling constants can be found in Table B.2.

Table B.2: Hyperfine coupling coefficients for NH (in MHz)

Term	$X^3\Sigma^-$	$A^3\Pi$
$b_{F\mathrm{H}}$	-70.6†	301.0
t_{H}	29.6†	30.2
a_{H}		74.1
$b_{F\mathrm{N}}$	20.0†	158.7
t_{N}	-22.8†	5.1
a_{N}		89.6
eqQ_{N}	-5.0	7.1

All values from [186] except those marked with †, which are from [194].

B.3.1 $X^3\Sigma^-(J''=1, N''=0)$

For this rotational ground state the only nonzero part of the hyperfine interaction will be the Fermi-contact term, which will produce energy shifts as well as mix states with the same F but different T. The five basis states for this calculation will be $|F=5/2, T=3/2\rangle$, $|3/2, 3/2\rangle$, $|3/2, 1/2\rangle$, $|1/2, 3/2\rangle$, and $|1/2, 1/2\rangle$. The block-diagonal form of H_{hf} can be factored into two 2×2 blocks and diagonalized separately. We will adopt the notation of Ubachs *et al.* when referring to the resultant states after diagonalization and write $F_{1,2}$ where 1 refers to the state with higher energy for a given F. The eigenvalues of H_{hf} are as follows:

$$
\begin{aligned}
E(5/2) &= -b_{F\mathrm{N}} - \tfrac{1}{2}b_{F\mathrm{H}} && = \text{-13.6 MHz}\\
E(3/2_1) &= -\tfrac{1}{4}b_{F\mathrm{H}} + \tfrac{1}{2}\sqrt{\tfrac{9}{4}b_{F\mathrm{H}}^2 - 4b_{F\mathrm{H}}b_{F\mathrm{N}} + 4b_{F\mathrm{N}}^2} && = 81.0 \text{ MHz}\\
E(3/2_2) &= -\tfrac{1}{4}b_{F\mathrm{H}} - \tfrac{1}{2}\sqrt{\tfrac{9}{4}b_{F\mathrm{H}}^2 - 4b_{F\mathrm{H}}b_{F\mathrm{N}} + 4b_{F\mathrm{N}}^2} && = \text{-47.9 MHz}\\
E(1/2_1) &= -\tfrac{1}{4}b_{F\mathrm{H}} - \tfrac{3}{2}b_{F\mathrm{N}} + \tfrac{1}{2}\sqrt{\tfrac{9}{4}b_{F\mathrm{H}}^2 - 4b_{F\mathrm{H}}b_{F\mathrm{N}} + b_{F\mathrm{N}}^2} && = 41.0 \text{ MHz}\\
E(1/2_2) &= -\tfrac{1}{4}b_{F\mathrm{H}} - \tfrac{3}{2}b_{F\mathrm{N}} - \tfrac{1}{2}\sqrt{\tfrac{9}{4}b_{F\mathrm{H}}^2 - 4b_{F\mathrm{H}}b_{F\mathrm{N}} + b_{F\mathrm{N}}^2} && = \text{-66.6 MHz}
\end{aligned}
$$

The splittings between these levels agree with the values measured by Wayne and Radford[194] to better than 2 MHz. The resultant states for the $F = 3/2$ and $F = 1/2$ blocks are given (in terms of the $|F, T\rangle$ basis) by

$$\begin{aligned} |3/2_1\rangle &\approx 0.75\,|3/2, 1/2\rangle + 0.67\,|3/2, 3/2\rangle \\ |3/2_2\rangle &\approx 0.67\,|3/2, 1/2\rangle - 0.75\,|3/2, 3/2\rangle \\ |1/2_1\rangle &\approx 0.41\,|1/2, 1/2\rangle + 0.91\,|1/2, 3/2\rangle \\ |1/2_2\rangle &\approx 0.91\,|1/2, 1/2\rangle - 0.41\,|1/2, 3/2\rangle\,. \end{aligned} \tag{B.64}$$

We can see that T is not a good quantum number for either $F = 3/2$ or $1/2$, though it is better for the $F = 1/2$ states.

B.3.2 $A^3\Pi_2(J' = 2, N' = 1)$

The matrix elements of the hyperfine Hamiltonian for the excited state have contributions from all four terms of Equation B.1. The electronic configuration for this state is $(1s\sigma)^2(2s\sigma)^2 2p\sigma(2p\pi)^3$, so there are two unpaired electrons, one σ and one π. The Fermi contact interaction from the unpaired σ electron dominates the hyperfine structure since σ electrons have finite overlap with the nuclei. The unpaired π electron contributes to the orbital hyperfine splitting, but its effect is on the order of 20% of the overall splitting. The numerical results for the energies and states (using the same $F_{1,2}$ notation) are given by

$$E(7/2) = 376 \text{ MHz}$$

$$\begin{aligned} E(5/2_1) &= 121 \text{ MHz} \\ E(5/2_2) &= \text{-}104 \text{ MHz} \\ E(3/2_1) &= \text{-}101 \text{ MHz} \\ E(3/2_2) &= \text{-}394 \text{ MHz} \\ E(1/2) &= \text{-}565 \text{ MHz} \end{aligned} \tag{B.65}$$

$$\begin{aligned} |5/2_1\rangle &\approx 0.90\,|5/2,1/2\rangle - 0.43\,|5/2,3/2\rangle \\ |5/2_2\rangle &\approx 0.43\,|5/2,1/2\rangle + 0.90\,|5/2,3/2\rangle \\ |3/2_1\rangle &\approx 0.97\,|3/2,1/2\rangle - 0.24\,|3/2,3/2\rangle \\ |3/2_2\rangle &\approx 0.24\,|3/2,1/2\rangle + 0.97\,|3/2,3/2\rangle\,. \end{aligned} \tag{B.66}$$

From this we see that the $|3/2\rangle$ states are nearly pure and so T is approximately a good quantum number for these states. The $|5/2\rangle$ states are slightly more mixed, but T may still be good for many calculational purposes.

B.3.3 Line Strengths

We can represent the interaction of the light field with the molecule by writing the energy of an electric dipole in an electric field:

$$W = -\boldsymbol{E} \cdot \boldsymbol{d} \tag{B.67}$$

where d is the electric dipole operator:

$$\boldsymbol{d} \equiv \sum_i e_i \mathbf{r}_i. \tag{B.68}$$

The direction of $\boldsymbol{E}$ can be chosen by the experimentalist, so for convenience we will suppose that we have linearly polarized light with $\boldsymbol{E} = E_o \boldsymbol{Z}$. We can rewrite the Hamiltonian in terms of quantum mechanical spherical tensor operators:

$$H_{\text{light}} = -E_o \mathsf{T}^1_{p=0}(\mathbf{d}) \tag{B.69}$$

The strength of a particular transition will clearly then be proportional to the square of the appropriate matrix element of $\mathsf{T}^1_{p=0}(\mathbf{d})$. We can begin evaluating these elements by applying the Wigner Eckart theorem:

$$\langle JFM_F T| \, \mathsf{T}^1_0(\mathbf{d}) \, |J'F'M'_F T'\rangle = (-1)^{F-M_F} \begin{pmatrix} F & 1 & F' \\ -M'_F & 0 & M_F \end{pmatrix} \langle JFT\| \, \mathsf{T}^1_0(\mathbf{d}) \, \|J'F'T'\rangle \, . \tag{B.70}$$

The 3-j symbol contains an effective $\delta_{M_F M'_F}$, so we can set $M'_F = M_F$. The electric dipole moment operator (Equation B.68) does not depend on nuclear or spin structure, so we can decompose F into J and T by writing

$$\begin{aligned} &\langle JFM_F T| \, \mathsf{T}^1_0(\mathbf{d}) \, |J'F'M_F T'\rangle = \\ &\quad (-1)^{2F-M_F+T+J'+1} \sqrt{(2F'+1)(2F+1)} \begin{pmatrix} F & 1 & F' \\ -M_F & 0 & M_F \end{pmatrix} \\ &\quad \times \begin{Bmatrix} J & F & T \\ F' & J' & 1 \end{Bmatrix} \delta_{TT'} \langle J\| \, \mathsf{T}^1_0(\mathbf{d}) \, \|J'\rangle \, . \end{aligned} \tag{B.71}$$

One can further expand the reduced matrix element to remove the spin part of the wavefunction, etc., but we already have what we need since our interest is in comparing the strengths of various hyperfine lines within a single level of a single branch (that is, J and J' will be fixed). The intensities will be given by:

$$A(JFM_F T, J'F'M'_F T') \propto$$
$$\delta_{M_F M'_F}\delta_{TT'}(2F'+1)(2F+1)\begin{pmatrix} F & 1 & F' \\ -M_F & 0 & M_F \end{pmatrix}^2 \begin{Bmatrix} J & F & T \\ F' & J' & 1 \end{Bmatrix}^2 \quad \text{(B.72)}$$

In zero field, we must sum over all magnetic sublevels of the ground and excited state if we want the total intensity of each hyperfine line. The summation can be simplified by using the orthogonality relation of 3-j symbols:

$$\sum_{M_F M_{F'}} \delta_{M_F M'_F}\begin{pmatrix} F & 1 & F' \\ -M_F & 0 & M_F \end{pmatrix}^2 = \frac{1}{3} \quad \text{(B.73)}$$

and this constant can be dropped from the proportionality to give us

$$A(JFT, J'F'T') \propto \delta_{TT'}(2F'+1)(2F+1)\begin{Bmatrix} J & F & T \\ F' & J' & 1 \end{Bmatrix}^2 . \quad \text{(B.74)}$$

While Equation B.74 is easy to use in the case of pure states, T is no longer a good quantum number for the mixed hyperfine states of NH even in zero field. To obtain line strengths we must keep track of the phases of the contributions to the dipole operator before squaring. If we can denote the ground state by $|\psi_{\mathrm{g}}\rangle = a\,|\eta_g, T_1\rangle + b\,|\eta_g, T_2\rangle$ and the excited state by $|\psi_{\mathrm{e}}\rangle = c\,|\eta_e, T_1\rangle + d\,|\eta_e, T_2\rangle$ where η stands for all

other quantum numbers, we can write

$$\langle\psi_g|\,\mathsf{T}^1_0(\mathbf{d})\,|\psi_e\rangle =$$
$$(-1)^{2F+J'+1}\sqrt{(2F'+1)(2F+1)}\,\langle\eta_g, J\|\,\mathsf{T}^1_0(\mathbf{d})\,\|\eta_e, J'\rangle\,(-1)^{M_F}\begin{pmatrix} F & 1 & F' \\ -M_F & 0 & M_F \end{pmatrix}$$
$$\times\left[a^*c\,(-1)^{T_1}\begin{Bmatrix} J & F & T_1 \\ F' & J' & 1 \end{Bmatrix} + b^*d\,(-1)^{T_2}\begin{Bmatrix} J & F & T_2 \\ F' & J' & 1 \end{Bmatrix}\right] \tag{B.75}$$

Our molecules are in a statistical (incoherent) superposition of magnetic sublevels, so to get the total line strength we must take the square of the magnitude and then sum over all M_F. This gives us one term that resembles the left side of Equation B.73 with an extra factor of $(-1)^{2M_F}$ in the summation. Since M_F is always either integral or half-integral (half-integral in our case) this factor can be ignored since the overall sign doesn't affect the identity. Furthermore, we can see that the cross terms will have opposite sign from the terms with $T_g = T_e$, so we will choose to make the cross term coefficient negative[2] and write

$$\begin{aligned} A(\psi_g,\psi_e) \;\propto\; & (2F'+1)(2F+1)\left[|a|^2\,|c|^2\begin{Bmatrix} J & F & T_1 \\ F' & J' & 1 \end{Bmatrix}^2\right. \\ & -\;(a^*bcd^* + ab^*c^*d)\begin{Bmatrix} J & F & T_1 \\ F' & J' & 1 \end{Bmatrix}\begin{Bmatrix} J & F & T_2 \\ F' & J' & 1 \end{Bmatrix} \\ & +\;\left.|b|^2\,|d|^2\begin{Bmatrix} J & F & T_2 \\ F' & J' & 1 \end{Bmatrix}^2\right] \end{aligned} \tag{B.76}$$

[2]The sign of a 3-j symbol is determined by $(-1)^s$ where s is the sum of the top row. Since we know that T_1 and T_2 must differ by an integer the overall sign of the cross terms will be positive and it is the signs of a, b, c and d that determine whether the interference is constructive or destructive.

This form for the transition strengths, along with the calculated state superpositions (Eq. B.64 and B.66) were used with literature line positions to generate the spectrum in Fig. 3.7.

Appendix C

Derivation of the Tensorial Spin-Spin Hamiltonian

The energy of two magnetic dipoles $\boldsymbol{\mu}_i$ separated by a vactor $\mathbf{r}$ can be written as

$$W = \frac{\mu_o}{4\pi}\left[\frac{\boldsymbol{\mu}_1 \cdot \boldsymbol{\mu}_2}{r^3} - \frac{3(\boldsymbol{\mu}_2 \cdot \mathbf{r})(\boldsymbol{\mu}_2 \cdot \mathbf{r})}{r^5}\right] \tag{C.1}$$

where μ_o is the permeability of free space. This can be made into a quantum mechanical Hamiltonian operator by casting it in terms of electron spin operators $\boldsymbol{\mu} = -\mathrm{g}_e\mu_\mathrm{B}\mathbf{S}$ to give

$$H_{SS} = \frac{\mu_o \mathrm{g}_e^2 \mu_\mathrm{B}^2}{4\pi r^3}\left[\mathbf{S}_1 \cdot \mathbf{S}_2 - 3(\mathbf{S}_1 \cdot \hat{\mathbf{n}})(\mathbf{S}_2 \cdot \hat{\mathbf{n}})\right] \tag{C.2}$$

where $\hat{\mathbf{n}} \equiv \mathbf{r}/r$. We can write the spin operators in terms of Cartesian coordinates and $\hat{\mathbf{n}}$ in terms of spherical angles θ and ϕ to write the term in brackets as

$$
\begin{aligned}
H_{SS} \;\propto\; & S_{1x}S_{2x} + S_{1y}S_{2y} + S_{1z}S_{2z} && \text{(C.3)}\\
& -3\left[S_{1z}\cos\theta + \sin\theta(S_{1y}\sin\phi + S_{1x}\cos\phi)\right] && \text{(C.4)}\\
& \times\left[S_{2z}\cos\theta + \sin\theta(S_{2y}\sin\phi + S_{2x}\cos\phi)\right]. && \text{(C.5)}
\end{aligned}
$$

Now the Cartesian spin operators can be written in terms of raising and lowering operators $2S_x = S_+ + S_-$ and $2iS_y = S_+ - S_-$ to give us

$$
\begin{aligned}
H_{SS} \;\propto\; & \left[-\frac{1}{4}S_{1+}S_{2-} + S_{1z}S_{2z} - \frac{1}{4}S_{1-}S_{2+}\right]\left(1 - 3\cos^2\theta\right) && \text{(C.6)}\\
& + \frac{3}{2}\left[S_{1-}S_{2z} + S_{1z}S_{2-}\right]\left(\sin\theta\cos\theta e^{i\phi}\right) && \text{(C.7)}\\
& + \frac{3}{2}\left[S_{1z}S_{2+} + S_{1+}S_{2z}\right]\left(\sin\theta\cos\theta e^{-i\phi}\right) && \text{(C.8)}\\
& + \frac{3}{4}\left[S_{1+}S_{2+}\right]\left(\sin^2\theta e^{-2i\phi}\right) && \text{(C.9)}\\
& + \frac{3}{4}\left[S_{1-}S_{2-}\right]\left(\sin^2\theta e^{2i\phi}\right). && \text{(C.10)}
\end{aligned}
$$

The terms in parentheses are proportional to second-order spherical harmonics:

$$
\begin{aligned}
\mathrm{Y}_{2,+2} &= \sqrt{\frac{15}{32\pi}}\sin^2\theta e^{2i\phi} && \text{(C.11)}\\
\mathrm{Y}_{2,+1} &= -\sqrt{\frac{15}{8\pi}}\cos\theta\sin\theta e^{i\phi} && \text{(C.12)}\\
\mathrm{Y}_{2,0} &= \sqrt{\frac{5}{16\pi}}\left(3\cos^2\theta - 1\right) && \text{(C.13)}\\
\mathrm{Y}_{2,-1} &= \sqrt{\frac{15}{8\pi}}\cos\theta\sin\theta e^{-i\phi} && \text{(C.14)}\\
\mathrm{Y}_{2,-2} &= \sqrt{\frac{15}{32\pi}}\sin^2\theta e^{-2i\phi} && \text{(C.15)}
\end{aligned}
$$

and the terms in square brackets are proportional to second-order spherical tensor product components:

$$\mathsf{T}^{(2)}_{+2}\left[\mathbf{S}_1,\mathbf{S}_2\right] = \frac{1}{2}S_{1+}S_{2+} \tag{C.16}$$

$$\mathsf{T}^{(2)}_{+1}\left[\mathbf{S}_1,\mathbf{S}_2\right] = -\frac{1}{2}\left(S_{1+}S_{2z}+S_{1z}S_{2+}\right) \tag{C.17}$$

$$\mathsf{T}^{(2)}_{0}\left[\mathbf{S}_1,\mathbf{S}_2\right] = \frac{2}{\sqrt{6}}\left(-\frac{1}{4}S_{1+}S_{2-}+S_{1z}S_{2z}-\frac{1}{4}S_{1-}S_{2+}\right) \tag{C.18}$$

$$\mathsf{T}^{(2)}_{-1}\left[\mathbf{S}_1,\mathbf{S}_2\right] = \frac{1}{2}\left(S_{1-}S_{2z}+S_{1z}S_{2-}\right) \tag{C.19}$$

$$\mathsf{T}^{(2)}_{-2}\left[\mathbf{S}_1,\mathbf{S}_2\right] = \frac{1}{2}S_{1-}S_{2-}. \tag{C.20}$$

We now have

$$H_{SS} \propto -3\sqrt{\frac{8\pi}{15}}\mathrm{Y}_{2,+2}\mathsf{T}^{(2)}_{-2}\left[\mathbf{S}_1,\mathbf{S}_2\right] \tag{C.21}$$

$$+\ 3\sqrt{\frac{8\pi}{15}}\mathrm{Y}_{2,+1}\mathsf{T}^{(2)}_{-1}\left[\mathbf{S}_1,\mathbf{S}_2\right] \tag{C.22}$$

$$-\ 3\sqrt{\frac{8\pi}{15}}\mathrm{Y}_{2,0}\mathsf{T}^{(2)}_{0}\left[\mathbf{S}_1,\mathbf{S}_2\right] \tag{C.23}$$

$$+\ 3\sqrt{\frac{8\pi}{15}}\mathrm{Y}_{2,-1}\mathsf{T}^{(2)}_{+1}\left[\mathbf{S}_1,\mathbf{S}_2\right] \tag{C.24}$$

$$-\ 3\sqrt{\frac{8\pi}{15}}\mathrm{Y}_{2,-2}\mathsf{T}^{(2)}_{+2}\left[\mathbf{S}_1,\mathbf{S}_2\right] \tag{C.25}$$

$$\tag{C.26}$$

which can be written compactly as

$$H_{SS} = -\frac{3\mu_o \mathrm{g}_e^2\mu_\mathrm{B}^2}{4\pi}\left\langle\frac{1}{r^3}\right\rangle\sqrt{\frac{8\pi}{15}}\sum_q(-1)^q\mathrm{Y}_{2,-q}\mathsf{T}^{(2)}_{q}\left[\mathbf{S}_1,\mathbf{S}_2\right]. \tag{C.27}$$